TOWARDS INSECT CYBORGS: INTERFACING MICROTECHNOLOGIES WITH METAMORPHIC DEVELOPMENT

by Alper Yusuf Bozkurt

TOWARDS INSECT CYBORGS: INTERFACING MICROTECHNOLOGIES WITH METAMORPHIC DEVELOPMENT

A Dissertation

Presented to the Faculty of the Graduate School

of Cornell University

In Partial Fulfillment of the Requirements for the Degree of

Doctor of Philosophy

by

Alper Yusuf Bozkurt

August 2010

TOWARDS INSECT CYBORGS: INTERFACING MICROTECHNOLOGIES WITH METAMORPHIC DEVELOPMENT

Alper Yusuf Bozkurt, Ph. D.

Cornell University 2010

Controlled by neurons, muscles are actuated to do mechanical work by converting chemical energy into mechanical power. Throughout history, humans have benefited from the muscle power of larger animals for farming, transportation and industry, the backbones of civilization. Although insects possess much higher muscle force to body mass compared to most large domesticated mammals, their direct locomotive uses have not been exploited reliably and reproducibly because of various challenges. This dissertation introduces the concept of Insect Machine Interfaces (IMI), a combination of microtechnology and neuroengineering, to control insect locomotion in a "biobotic" manner through the neuromuscular system.

Early Metamorphosis Insertion Technology (EMIT) is a novel neurotechnological pathway for integrating microelectronic sensing and actuation platforms on insects during metamorphosis. Metamorphic development not only provides an elegant and effective method of mechanically affixing artificial systems in or on an insect, but also enables a reliable bioelectrical interface without any observable short term adverse effect on insect flight behavior.

As an application of biobotic control of insect locomotion, the first results towards flight navigation in moths were established in this research. We were able to demonstrate on-demand wing actuation and flight direction control using microprobes inserted through the EMIT procedure, with the goal of insect navigation and domestication. Using this procedure, we were able to alter and control the flight of tobacco hawkmoth *Manduca sexta* by actuating its flight muscles on tethered setups. Successful locomotion control for both land and air was also demonstrated for the first

time with remotely transmitted radio signals through electrodes inserted in the antennal lobe and neck muscles of the insect following an EMIT procedure. Initiation and cessation of flight and walk, as well as yaw actuation were obtained on freely flying and walking lift assisted moths through joystick manipulation on a conventional model airplane remote controller. The concept of lift assisted flight allows for transporting tens of grams while potentially increasing the flight duration of the insect biobots, enabling a vast number of engineering applications in which such biobots can be deployed ranging from ecological monitoring to search-and-rescue missions during natural disasters..

BIOGRAPHICAL SKETCH

Alper Bozkurt received a B.Sc. degree in electrical and electronics engineering in 2001 from Bogazici University in Istanbul, Turkey where he performed research on EEG source localization. This was followed by a M.Sc. degree in biomedical engineering in 2004 at Drexel University in Philadelphia, Pennsylvania, where he developed functional near infrared spectroscopy systems for brain-machine interfaces to augment cognition and for clinical monitoring of the newborn brain in neonatal intensive care units. He continued his doctoral studies at Cornell University, School of Electrical and Computer Engineering, where he developed microsystems for neural engineering applications and received his Ph.D. degree in 2010. Alper is a recipient of the Calhoun Fellowship from Drexel University and Donald Kerr Award at Cornell University.

To
my parents Fatma and Selim Bozkurt,
my grandmother Sevim Ayturan,
and
my wife Tuba

ACKNOWLEDGMENTS

One truth that I have learned after four degrees, at three universities, in three different disciplines is that not one thing could have ever happened without the support and encouragement of so many people, starting with family, extending to friends and to those in the research world whose contributions to scientific advancement are revealed in books, theses, journal papers and conference abstracts.

First, I would like to thank my advisor, Amit Lal, to whom I owe so much. Amit, only with your innovative ideas and endless moral support was I able to maneuver around difficult problems throughout our scientific explorations for this dissertation. You have been my friend, my mentor, my confidant and my colleague. Not only have you taught me the dynamics of the MEMS field, but you have also taught me how to come up with groundbreaking ideas to do front-end research. With your trust in me, I was nourished as an independent researcher, and that encouraged me to take an academic path. Whatever is waiting for me in my scholarly future, I will be prepared because of you.

I would also like to thank the rest of my thesis committee for their support. Sunil Bhave, Harold Craighead and Robert F. Gilmour, Jr. provided me with invaluable advice and comments on both my research and future research career plans. Robert, I will never forget your efficiency as we worked on our publications together and Sunil for your extraordinary support as a mentor, colleague and friend as I applied for faculty positions.

I have been very lucky throughout most of graduate school in that I have been able to concentrate mostly on my research and have direct access to generous research funding. A large part of this funding is due to the gracious support of DARPA under the Hybrid-Insect Micro-electro-mechanical Systems (Hi-MEMS) program. I would also like to take this opportunity to thank everyone in Boyce Thompson Institute (BTI)

for supporting my research by always supplying the best insect specimens over the last four years.

I have also been fortunate to have a wonderful group of friends at Cornell that includes my lab mates in SonicMEMS Lab, users and staff of CNF and NBTC, and many other ECE students and faculty, too numerous to mention one by one. You were the people with whom I had immediate access to discuss my research or simply to goof off. I have learned so much from all of you through your constructive criticism and collaboration. Especially to the people of the SonicMEMS Lab, your friendship made everyday working hours fun. This, I believe, is the key behind all successful research groups, “having spirit.”

I would also like to express my thanks to the Turkish community of Ithaca and all other friends, again too many to name, who made Ithaca a second home for us. Special thanks go to Jill Marie for being a true and patient friend on editing this work with me.

None of this would have been possible without the support and encouragement of my parents, Selim baba and Fatma anne even for the most crazy decisions I ever made. You let me be myself, and you put numerous opportunities in front of me as I was growing up. You will make wonderful grandparents for Asude Leyla who also deserves acknowledgement for being Daddy's well-behaved girl while finishing up my studies at Cornell. Leyla, your entrance into Mommy’s and my life was the most wonderful thing in the world.

My deepest gratitude is reserved for my eternal happiness, my encourager, my companion: my precious wife Tuba. You are always there for me, especially when I need help and moral support to get past all the self-doubt that inevitably crops up in the course of a PhD. You are the first person I turn to in good times and in bad. You

have given me the courage to make the next transition in my life, and you always stand behind me through thick and thin. Thank you, my only bitisim.

And the One, the Force behind everything and the Owner of my heart, You know how thankful I am more than I…

TABLE OF CONTENTS

LIST OF FIGURES

LIST OF TABLES

CHAPTER 1
INTRODUCTION

1.1 Technology Development for Domestication of Insects

As early as 15,000 BCE, humankind has partnered with several animal species through domestication [Mor 06], where different animal populations were brought under control for a wide range of reasons, primarily as beasts of burden. Through animal domestication technologies using man-made devices such as horseshoes, whips, eye covers and genetic selection, equids, bovids and proboscideans could then be used for pack animals because of their large muscle volume and low resistance to domestication. Successful domestication is believed to be the basis for civilized societies, for domesticated animals allowed a stable agricultural society in which water could be pumped and the earth could be dug, thus supplanting the hunter-gatherer lifestyle [Dia 97].

Out of the many millions of animal species that could have been domesticated, only a few have been successfully used for their muscle power [Dia 02]. Interestingly, insects possess much higher muscle-force to body-mass compared to that of most large domesticated mammals. The insects' larger muscle cross-sectional area with respect to muscle volume allows them to carry payloads equivalent or greater than their body weight, whereas the larger domesticated species can carry loads that are, at most, half of their body weight [Vog 01]. On the other hand, it is relatively difficult to control insect behavior by training the insects as lack of learning related components in their behavioral complexity and underlying neural substrates. In particular, insects lack the necessary experience-dependent memory storage installed [Men 07]. Therefore, the insect population has been domesticated only for producing valuable commodities and food such as silk and honey, in which domestication involves

understanding the social or physiological behavior of the population as a whole, rather than training individuals. As a result, their direct locomotive uses have not been exploited reliably and reproducibly.

Furthermore, navigating large animals has been facilitated historically by man-made devices such as horseshoes, reins and blinders. Until recently, navigation technology needed for smaller animals did not exist. Hence there is a lack of pathways to utilize insects for their load carrying capacities. Historically, insect-scale transportable payloads have also been hard to manufacture. Nevertheless, with continued miniaturization of information sensing, computing, processing and communication technologies, it now seems likely that insects can be navigated and be useful as mobile information gatherers. In this sense, modern microelectronics and micro and nano electromechanical systems can provide the building blocks of insect domestication technology. This technology also allows for payloads with minuscule weights containing a dense amount of information storage and processing capacity and functional ability. However, using insects as "beasts of burden" has still not been an easy task, for mounting a payload to an insect is a challenging operation due to the insect's size and surface morphology making the load attachment difficult. Moreover, navigating the insect to carry the payload from one specific point to another is even more challenging [Gub 45].

1.2 Insect Machine Interfaces (IMI)

Developments in micromachining technology have shifted the notion of implantable neuromotor prosthetics from science fiction to reality [Leb 06]. Tiny silicon and polymer based neural electrodes have improved target localization by high density probing, enabling complex brain machine interfaces (BMIs). The highly miniaturized CMOS electronics on these micromachined probes have made possible a

number of complicated neurophysiological studies by coupling the state of art signal processing technologies to initiate and record advanced brain function [Naj 97, Wis 05]. This technology provides techniques and tools that allow us to understand and generate robust electronically controlled muscle movement. Restoring impaired motor function has been possible in vertebrates like rabbits, cats, monkeys, and will eventually be useful for humans, by controlling their motor function using either external operator commands or the output of the subject's own brain [Sco 06, Konig 02]. Remarkably, these systems are already at the size scale (~5 mm^3) to fit on an insect to build insect-machine-interfaces (IMI).

For a reliable IMI, hybrid bio-electronic structures with insects need to be formed through which CMOS devices and MEMS structures are coupled with the insect's natural sensors and actuators. Such interfaces may provide access for neural engineers to the neuromuscular system of the insect to study and thus control its sensory and behavioral physiology. These studies can eventually lead to solving many engineering challenges by understanding and manipulating the communication, and automatic navigation control systems of insects. One such cybernetic challenge is to control insect locomotion for carrying electronic payloads, as stated earlier.

To achieve this, electrical excitation of neuromuscular systems can be used to guide insects to perform particular tasks using either routine-operant conditioning or classical conditioning techniques. Through implanted payloads and electrodes, individual insects can be exposed to remotely generated exterioceptive inputs so that behavioral responses can be produced. Furthermore, proprioceptive inputs can also be applied directly to the central or peripheral nervous system through artificial processors that are inserted in the tissue to generate motor output. These concepts have the potential to control insect's behavior and benefit from their muscle power in a

"biobotic" manner by using artificial electronic systems in order to tap into the nervous and neuromuscular system of the insect [Woo 00].

1.3 An Application: Insect Based Micro-Air-Vehicles

When centimeter scale Micro-Air-Vehicles (MAVs) or tiny fliers are considered, the power source required to fly them has limited their mission time and autonomy within the constraints of generating lift, powering flight control sensors and actuators, and avoiding collisions [Woo 00]. The design and manufacturing of small-scale moving parts and control algorithms to provide lift and sustainable flight control with collision avoidance ability are also prohibitively challenging for realizing reliable flight.

For many decades, insect flight has fascinated robotic engineers who have confronted challenges in realizing human-made centimeter-scale flying machines. Researchers have greatly benefited from the study of these naturally occurring fliers by designing individual biomimetic structures as MAV parts [Tau 00]. Several technical approaches have been explored in order to combine these man-made propulsion and power components as a complete insect-mimetic small scale autonomous flying machine [Ell 99]. However, it has not been possible to reach the long mission duration and aerodynamic performance and maneuverability of insects because the artificial flight actuators are not sufficiently efficient, and the power and energy density of power sources are inadequate for insect-like flight [Ell 99, Wo 00].

The motivation behind this research has been the alternative idea of directly taming and domesticating insect locomotion in a "biobotic" manner to build hybrid bio-electro-mechanical MAVs by electrically controlling the insect's neuromuscular system through IMI [Tau 00]. Insects are self-powered. They operate with highly efficient flight muscle actuators and carry on-board flight control sensors as well as

collision avoidance systems to perform exquisite acrobatics. Therefore, the specific methodology developed in this study has broad implications not only for studying the insect-machine-interface, but also for the future use of navigated insects as hybrid MAVs. An application of such a hybrid platform is to convert insects into mobile environmental sensing systems. When instrumented with equipment to gather information for environmental sensing, such working animals can potentially assist humans to monitor the ecosystems that we share with them.

1.4 Outline of the Dissertation

A summary of the subsequent chapters is presented below as an outline of the presented work: Chapter 2 presents a novel surgical procedure, Early Metamorphosis Insertion Technology (EMIT), in which artificial implants are inserted in insects in the early stages of metamorphosis. Here, the implants are integrated within the structure and function of the insect body as a result of metamorphic development. The inserted microprobes emerge with the insect where the development of tissue around the electronics during pupal development allows mechanically stable and electrically reliable structures to couple to the insect. Remarkably, the insects do not react adversely or otherwise to the inserted electronics in the pupal stage, as is true when the electrodes are inserted in the adult stages. Details of the metamorphosis formed bioelectric interface are also discussed. The electrical and mechanical characteristics of this novel bio-electronic interface are reported, which we believe would be adopted by many investigators exploring biological behavior in insects with negligible or minimal traumatic effects compared to those encountered when the probes are inserted in the adult stages.

In Chapter 3, the anatomical, physiological and behavioral basics of the biological flight control system on insects are presented with a particular focus on

order Lepidoptera since the *Manduca sexta* was selected as the model insect. The key parts on the insect's anatomy that can be actuated to direct the locomotion of the insect are highlighted.

The development of the implantable electronic backpack, presented in Chapter 4, is the key step to overcome the technological bottleneck towards the concept of insect cyborgs. The mechanical flexibility of the inserted electrodes is shown as an important variable for reliability of the bio-electrical interface, and design rules on the flexibility of the inserted microsystem are presented. Novel methodologies to obtain low-cost electrodes are discussed. Also presented is an investigation of tissue-microprobe biological and electrical compatibility.

Chapter 5 reports various efforts towards the direct control of insect flight by manipulating various parts of the locomotory physiology via microprobes and electronics introduced through the Early Metamorphosis Insertion Technology (EMIT). Moreover, the control of flight and gait were demonstrated for the first time with a radio controlled, lift-assisted, electrode-instrumented *Manduca sexta* by altering the direction of turn through applied neuromuscular pulses. Electrical pulsing of the targeted locations created flight and gait initiation, cessation and yaw maneuver on the insects whose locomotion was supported by the lifting force of helium balloons.

CHAPTER 2
DEVELOPMENT OF SURGICAL TECHNIQUES

2.1 Surgical Challenges with Adult Insects

Previous researchers have attempted to attach electronic systems to insects for telemetric recording applications to understand how neural systems function during natural flight [Tau 00, Sho 04]. All of these attempts to attach or implant artificial systems in insects have posed many challenges involving the potential to disturb the natural flight of the insect. Superficially attached or surgically inserted artificial platforms on the adult insect are not reliable, for the inserted devices at this stage can shift, create mass imbalance, and damage tissue, especially when the inserted electronic probes and systems are rigid. Superficially attached or surgically inserted interface payloads also have the potential to be rejected both physiologically and behaviorally because they are perceived as foreign objects by the insect. Payloads can also move because of body induced inertial and stress forces, potentially causing tissue damage and experimental variability. Moreover, the surgery required to precisely place electronics onto or into adult tissue accurately is challenging because the insect tissue and organ feature dimensions are comparable to the electronic neural or muscular probe dimensions. The exoskeleton is covered with the readily shed-able scales and piles that interfere with the surgical innervations. The hard outer cuticle is often difficult to penetrate without significant collateral tissue and probe damage. All these factors can make a surgical or superficial implantation operation of artificial structures to the insect a challenging and delicate task. Therefore, it is a challenge to implant electronic systems readily and reliably to modulate the insect's flight without disturbing the insect's own efficient flight mechanism.

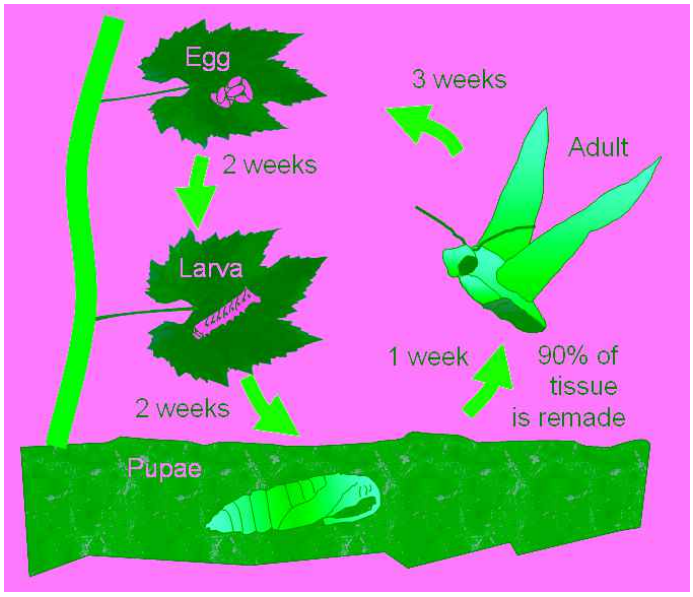

Figure 1: Life Cycle of Manduca sexta

2.2 Metamorphosis Based Surgery

In order to solve the issues involved in externally attaching control and recording electronics to the insects, a novel implant insertion pathway based on metamorphic development will be described in this section. During metamorphic growth, holometabolic insects are transformed from the larval (or nymph) stage into an adult insect after passing through a pupal stage (Figure 1). In each of these steps, the insects undergo an extensive programmed degeneration and remodeling to be transformed from a slow crawling caterpillar to an adult with many complex behavioral capabilities [Duc 00, Lev 95]. It has been shown that insects can survive extreme parabiotic surgeries performed during the pupal stage, where surgery related wounds are rapidly repaired through histogenesis [Wil 48, Wil 61]. In light of this fact, a surgical procedure has been developed in which an electronic payload is inserted in the insect in the early stages of metamorphosis (Figure 2). As the developing tissue forms around it, the payload adoption by the body not only ensures a secure attachment to the insect, but it also enables a highly predictable electronic

interface to the insect's sensorial, neural or muscular systems; this procedure is known as "Early Metamorphosis Insertion Technology" (EMIT). Structures inserted in the pupae in the early stages of metamorphosis emerge as a part of the insect's body; thus, by taking advantage of the rebuilding of the entire tissue system, insect cyborgs with a reliable biointerface are created. This hybrid structure enables a platform in which CMOS and MEMS can be used as sensors and actuators not only for insect flight control, but also for biological and environmental sensing. Using these techniques, it may be possible to control an insect's flight actuators by the various excitable points on the insect's neurophysiological system described in Chapter 3.

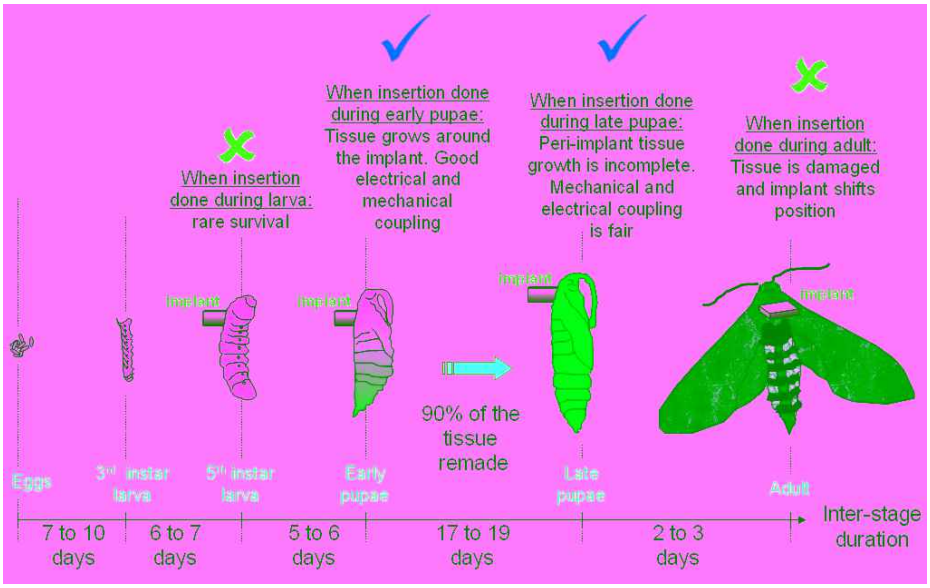

Figure 2: The life-span of Manduca sexta during metamorphic development and the results of insertions done at various stages of metamorphosis

2.3 *Manduca sexta* as a Model Insect

EMIT can be applied to any insect/animal that undergoes metamorphic development (moths, butterflies, beetles, etc.) to create insect cyborgs with different locomotion capabilities. In this thesis, the *Manduca sexta* (tobacco hawkmoth) was

selected as the model insect. The *Manduca sexta* has a variety of traits that make such a wide range of applications for the inserted devices possible.

Manduca sexta belongs to the family group of Sphingidae under the order Lepidoptera. Easy to rear and maintain under laboratory conditions, *Manduca sexta* is known as the "lab rat" of insect physiology, where, both its neurophysiology and flight behavior dynamics have been well studied. When *Manduca sexta* goes through its complete metamorphosis, an extensive programmed degeneration and remodeling transforms it from a terrestrial pupae to an aerial adult (Figure 1). As will be described later, this metamorphic transformation is a required part of the EMIT procedure.

The short duration of the pupal stage is a critical concern in obtaining a rapid experimental outcome. *Manduca sexta* has a relatively short pupal stage of three weeks. Therefore, a relatively shorter wait-time is required to obtain the emerged adults for further experimentation, compared to other insects undergoing complete metamorphosis. *Manduca sexta* has an adult lifetime of 2–3 weeks. With approximately 10cm of wing span, *Manduca sexta* can carry up to 1.5 grams of payload and fly miles without stopping. The relatively large size of the insect is also advantageous for easier target localization during the surgical insertion process. All these properties make *Manduca sexta* an ideal candidate for becoming an insect cyborg with implanted electronic payloads both to manipulate flight and to gather, store and transmit environmental information. Therefore, all the methodologies in this thesis will be described in considering the anatomical, physiological and behavioral properties of the *Manduca sexta.*

2.3.1 Metamorphosis of Cuticle and Flight Muscles in *Manduca sexta*

During metamorphic growth, the larval body goes through the intermediate stages of pupal development in which two layers of cuticle are formed. The epidermal

cells secrete the first set of cuticle (outer exocuticle) during molting, followed by the secretion of two more adjacent inner layers of cuticles: the endocuticle in the middle and in the innermost epicuticle. Later, the epicuticle is separated from the exocuticle by digestion of the endocuticle. The hardened epicuticle forms the exoskeleton and wings of the adult insect while the exocuticle goes through a complete transformation to form a hard shell around the pupa. Some of these exocuticle features are linear depressions that serve as mechanical stress points, where the exocuticle fractures during eclosion (emergence from the pupa). These features are known as the ecdysial lines in which the exocuticle is much thinner. These lines are mechanically programmed to split during eclosion, and can be visually easily differentiated from an external view. After fracture, the exocuticle is shed by means of peristaltic and partial rotary movements of the abdomen. An eclosion is triggered by the release of an eclosion hormone when the end cuticle is sufficiently digested [Klo 02].

The development of the cuticle is a key process of metamorphic growth in the EMIT design procedure. Although both cuticle layers are penetrated during the insertion process, the micro-implants are anchored to the body for mechanical stability at the epicuticle. This layer cannot be observed externally until the emergence of the adult insect from the pupa as it sheds its exocuticle. However, body parts such as wings, antenna and regions of the thorax (pro-, meso-, and metathorax) can be differentiated visually by means of the conformational overlays and intersegmental folds of the exocuticle during pupal development. Therefore, the first step of EMIT involves mapping the target location visually through observation of the structural conformations that form the exocuticle surface topology. For example, the surface features on the mesothoracic exocuticle provide target localization for insertions in the pupal flight muscles. Although the size of the insect larva changes dramatically before molting, the pupal stage growth is negligible because of scleratization of the inner and

outer cuticle. Therefore, any shifting of the targeted location in the body secondary to metamorphic growth is not a concern.

In lepidopteran metamorphosis, neuromuscular development occurs inside the thoracic body as the cuticle develops on the outside. The entire musculature system of the larva is degenerated and formed de novo in order to support newly emerging adult behaviors. Larval neurons required for adult behavior are retained and respecified throughout the metamorphosis process through the formation of new dendritic morphologies, whereas those lacking such adult functions are removed by programmed cell death [Lev 95]. During this intermediate stage between larva and adult, the aerodynamic body shape and appropriate sensory equipment are also formed to support adult aerial behaviors.

The metamorphosis of *Manduca sexta*'s motor neuro-muscular system for flight starts with a molting process which is triggered by the secretion of ecdysteroids by larval prothoracic glands. This process retracts the terminals of motoneurons from the larval thoracic body wall muscles that will form specialized flight muscles after complete degeneration. The fibers of these degenerated muscles form the templates of thoracic flight muscles and the myoblasts start to migrate to these templates. The flight muscles continue to develop as they accumulate myoblasts on the fiber templates in which the number of accumulating myoblasts determines the eventual size of the adult muscle. After the onset of muscle formation, motoneuron terminals start to develop: first, the central dendrites are formed, followed by allometric growth of the finer branches in the periphery, in which new synaptic contacts are built with predetermined muscle fibers [Bay 01]. The proliferation of flight muscle motoneuron dendrites occurs during the last two thirds of the pupal stage [Duc 00].

2.3.2 Results of Insertion of Various Structures to Thorax

To describe the EMIT procedure and demonstrate its efficacy, four different structures were surgically implanted in the insect thorax at different stages of pupal development (Figure 3). First, rectangular shaped dummy structures made out of silicon and polyimide substrate were inserted in the pupae (Figure 4, 5). The resulting emergence outcomes were analyzed as well as the surgical dissections (Figure 3). After the dummy structures were inserted, probes with electrically active pads were etched on these two substrates (silicon and polyimide) and inserted in the flight muscles of the insect (Figure 6, 7). In addition to the microfabrication based devices, standard wire electrodes were also inserted in the insect brain (Figure 8), for wire based actuation is the standard method to study invertebrate neural systems. Detailed information about the design and fabrication of these electrodes can be found in Chapter 4.

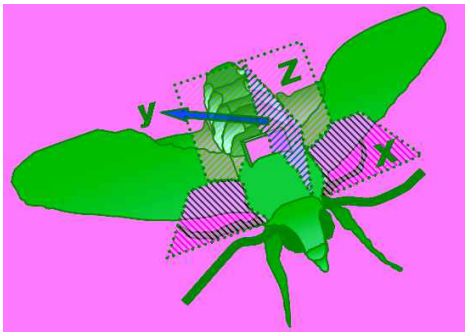

Figure 3: Dissection planes performed on the insect (X: Lateral, Y: Longitudinal, Z: Transverse)

For all the experiments in this study, *Manduca sexta* were obtained from a colony at Boyce Thompson Institute (Ithaca, New York), where they were reared on an artificial diet under a 17:7 hr light/dark cycle regimen at 26ºC and ~60% humidity. More information about the rearing protocol can be found in the Appendix. Both chronological and morphological criteria were used to record the developmental stage

for probe insertion. Different visual patterns on the pupal wings and thorax indicate the stage of metamorphic growth.

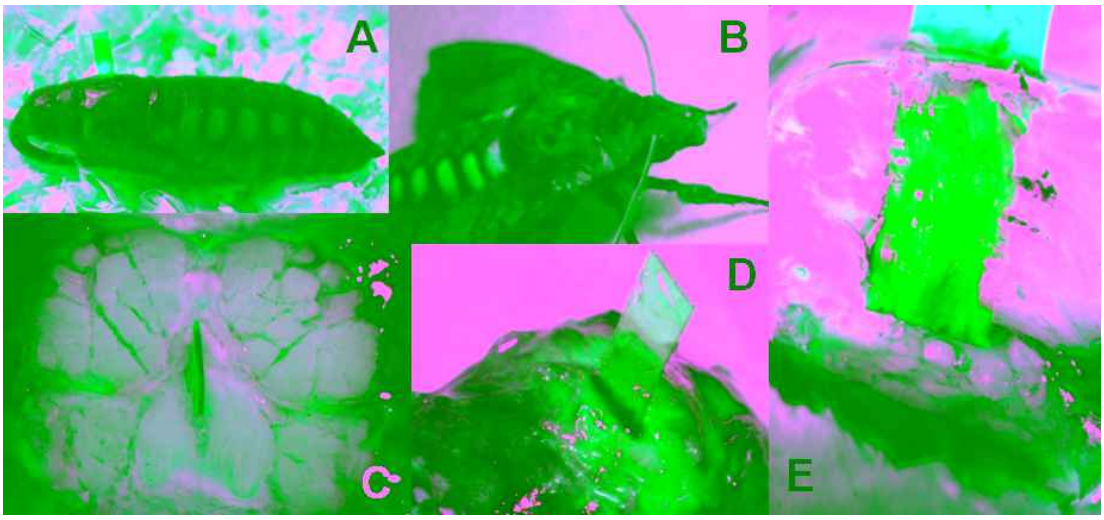

Figure 4: A rectangular shaped dummy polyimide piece was inserted into pupae (A) and it emerged successfully with the adult (B). The longitudinal (E) and transverse (C) cross-sections show no sign of scarring or disturbance in the tissue. The scales were moved from the cuticle at the point of insertion (D) to observe the healing of the cuticle around the insert.

For the surgical insertions, the insect pupae at various stages of metamorphic development were anesthetized through cold treatment (4ºC) for 10–15 minutes. Subsequently, mesothoracic incisions matching the size of the implant were made with a scalpel on the thoracic tergum (both on the epicuticle and exocuticle) of each insect. The implants were pushed into the muscle tissue through these incisions. Pupae were returned to the rearing incubator after the surgery to undergo normal metamorphic growth. The insects with implanted structures were supported from the left and right body sides for at least 24 hours to prevent pupae rotatory movement, which could have shifted the probes before sealing occurred. No adhesive was used to seal the incisions. Instead, the cuticle was allowed to heal naturally, creating a biological seal. It had been discovered that artificial glues adhered the exocuticle to the epicuticle and prevented successful eclosion. All surgeries and dissections were performed according to high standards of ethical behavior.

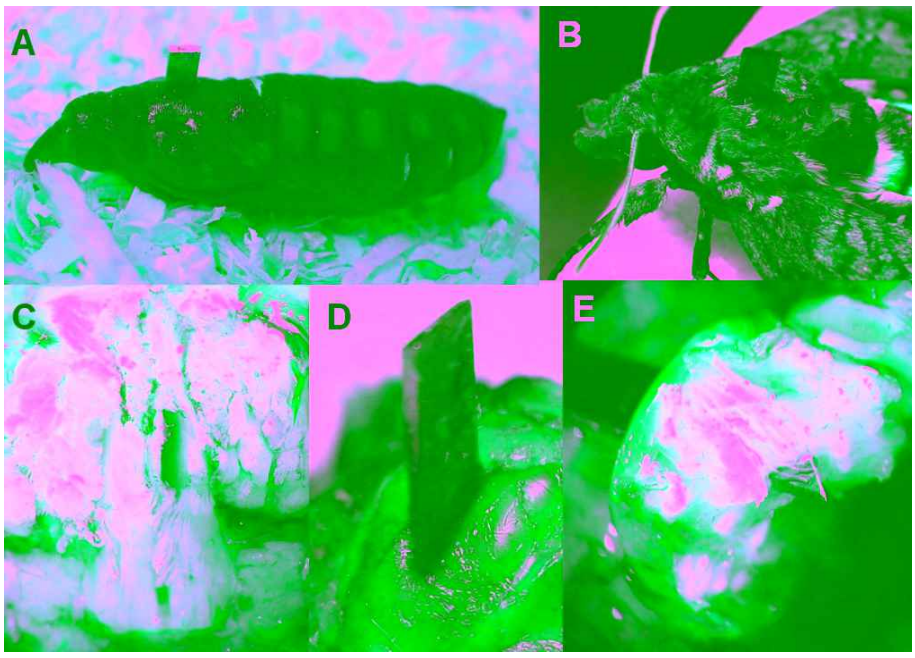

Figure 5: A rectangular shaped dummy silicon piece was inserted into the pupae (A) and emerged successfully with the adult (B). The longitudinal (E) and transverse (C) cross-sections show no sign of scarring or disturbance in the tissue. In (C) the silicon structure was pulled to see the tissue formed around the insert. The scales were moved from the cuticle at the point of insertion (D) to observe the healing of the cuticle around the insert.

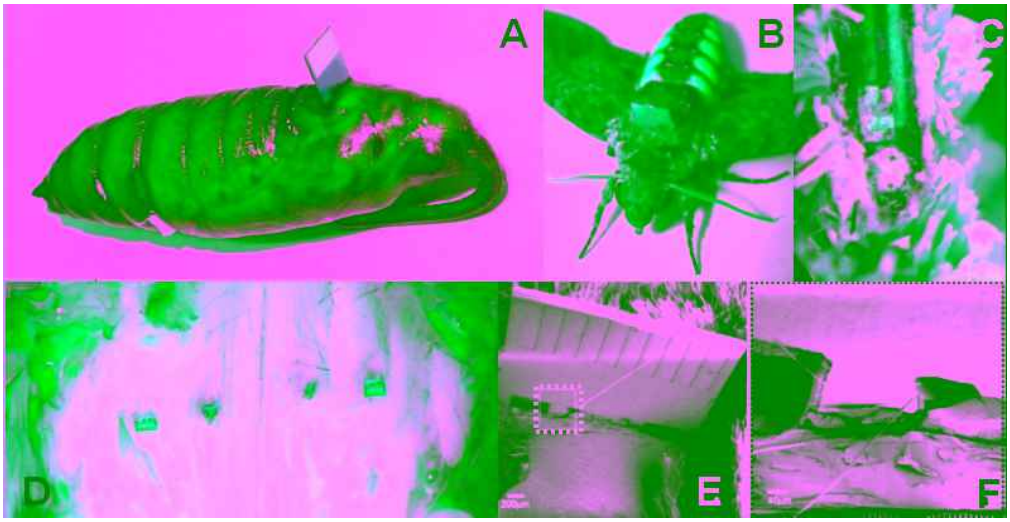

Figure 6: The flexible polyimide probe (see Chapter 4 for details) was inserted into pupae (A) and emerged with the adult successfully (B). The vertical (C) and transverse (D) cross-sections show no sign of scar or disturbance in the tissue. In (C), tissue growth was observed through the holes at the tip. The scales were moved from the cuticle at the point of insertion (E) to observe the healing of cuticle around the insert. The pictures were taken with SEM. (F) is the zoomed in version of dotted part in (E) where cuticle healing around the insert is shown.

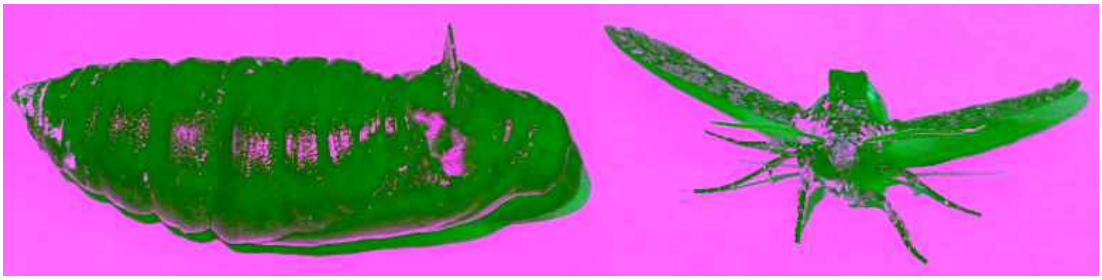

Figure 7: Silicon probes (see Chapter 4 for details) were also inserted into the pupae (A) and emerged successfully with the adult (B). No dissections were performed due to the fragility of silicon probes.

The optimal time for surgical insertion (Figure 2) was found to be seven days before emergence (Table 1). For insertions earlier than seven days, the fluidity of the muscle precursor tissue prevented adequate sealing around the insert and decreased the survival rate when the tissue started leaking out. When inserted later, very close to eclosion, the preformation of epicuticle and muscle fibers resulted in incomplete attachment and inefficient anchoring of the insert to the tissue. In this case, the tethered implants detached easily during the experiments. The insertion process also suffered in the buckling of the flexible microprobe when it was inserted in the stiffer muscle tissue. Moreover, failure of the bioelectrical interface was more frequent with these late inserted probes because of similar failure mechanisms observed with the adult inserted microprobes.

Table 1: The Observed Survival Rates of the Surgeries for Different Stages of Insertions

Insertion Stage	Number of insertions	Survival rate
Larva	10	0%
Pupae	20	95%
Adult	10	80%

To increase the number of successful emergences during eclosion, an additional cracking procedure was found to be effective. This procedure involved

cracking the pupae 24 hours before emergence at a time when the exocuticle is quite brittle. At the end of the pupal stage, the cuticle cracks along the line formed by the surgical incisions and the insects eclode naturally with the implanted structures. The inserted structures can easily slip out following these cracks during eclosion and prevent possible blockages and obstructions on their way. Otherwise, inserted structures may pin the insect to the exocuticle, preventing successful emergence (Figure 9). In this way, the successful emergence rate was increased from an average of 17% to 90% for all the structures in which all of the moths had fully inflated wings.

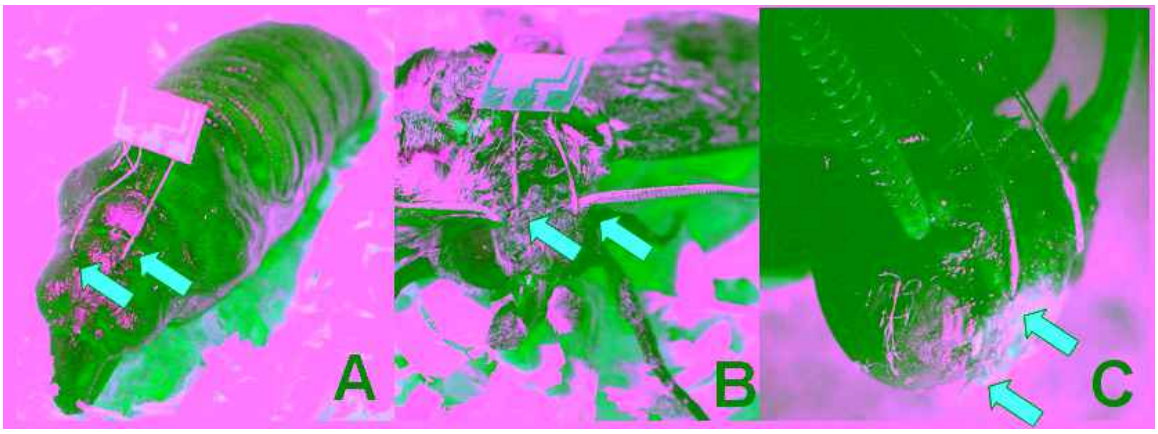

Figure 8: Arrows indicating insertion points of the probe in the pupal stage (A) and on emerged adult insect (B). Probe adoption by the brain tissue (C) revealed with the removal of the vertex (front part of the head)

The rectangular silicon and polyimide structures (Figure 4, 5) demonstrated similar surgical and emergence results. In the case of the shaped probes, the silicon substrate (Figure 7) caused a lower yield of approximately 20% because of the fragility caused by its geometry (Figure 34). The breakage of the electrodes during insertion, emergence or flight control experiments resulted in unsuccessful experimental attempts. The rigid silicon structure also created a strain mismatch with the softer tissue surrounding it. As a result, silicon was not pursued further as a substrate material for this research.

Figure 9: An example of unsuccessful emergence where the insert avoided complete release of the cuticle

2.3.3 Post-emergence Analysis of the Surgical Implants

Potential probe compatibility failures for the emerged adults were inspected to improve the reliability of the implantation technology. These are described below in a chronic timeline. Post-experimental dissections were performed on the implanted insects (Figure 3), and the tissue response to the persistent presence of the probes was inspected. The immunoglobulins that mediate immune reactions in vertebrates are not actually present in insects. Instead, insects utilize humoral mechanisms to identify and fight with foreign objects [Cha 82]. Hemolymph penoloxidases were activated at the site of cuticular injury, and the proteins around the injury site were sclerotized to avoid invasion of microorganisms. Antibacterial hemolymph proteins such as hemolin were simultaneously produced to initiate an immune response against any possible infection. As a result, no inflammation or tissue disturbance was observed at the site of the dissection in any of the insects (Figure 4, 5, 6, 7, 8).

Adverse tissue reactions to the microprobe insertion were not observed visually, probably because the microprobes were inserted in the soft gel-like pupal muscle tissue prior to the formation of flight muscle fibers. The body flexure-induced strain mismatch between the probe and muscle tissue was also minimized because of the flexibility of the substrate when polyimide was used. Force was applied to the insect via a tether cable, which was sustained successfully at the hardened cuticle-

microprobe interface as a result of the rigid matrix that was formed by cross-linked cuticular protein molecules around the implant (Figure 4D, 5D, 6E, 8C). Figure 6F shows how protein formation around the probe at the insertion points healed the cuticle, thereby sealing the points. Tissue adhesion to the microprobe and growth of muscle tissue through the holes at the tip further improved mechanical anchoring (Figure 6C). All these are indications of structural integration with the body tissue during metamorphosis.

When the probes were extracted, as explained in the next section, a considerable amount of tissue was removed with the pupae-inserted probes, which indicates good anchoring and adoption of the tissue (Figure 10, 11). In contrast, when probes were removed from the moths that had been implanted in the adult stage, very little tissue remained on the probe, indicating a weaker biomechanical interface and highlighting a key advantage of early pupae insertion.

2.4 Comparison of the Mechanical Coupling In Vivo

The extraction force of the probes was measured when the insect was anesthetized in order to assure the inertial movement handling of the added payloads by the mechanical coupling of the tissue-probe interface. After the successful emergence of the adult insect, the implants were pulled by a force transducer attached to a micromanipulator (Figure 10). The micromanipulator was programmed to pull the probe at a speed of 100μm/s. The increased force required for EMIT inserted probes indicates that the formation of tissue around the probe increases the reliability of the insert against the stresses encountered during flight.

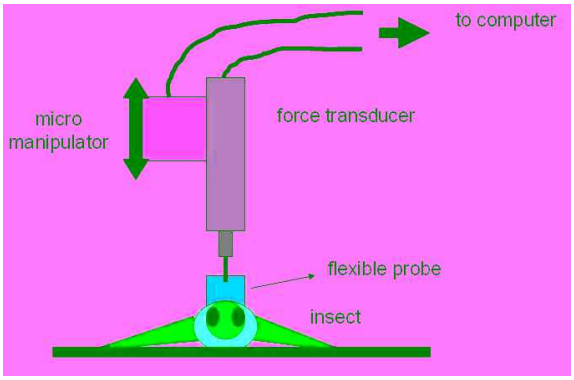

Figure 10: Experimental set-up where implanted flexible probe was pulled from the insect using a force transducer connected to a computer for recording

The typical force curve of the probe extraction from the insect can be seen in Figure 11. An average of approximately 2N was measured on this set-up as the required force for extracting the implant from the insect body, which indicates that an inertial acceleration of around 1000m/s^2 (or ~200 g for an upside down flight) would need to be applied to the attached payload during flight as a result of sudden flight maneuvers.

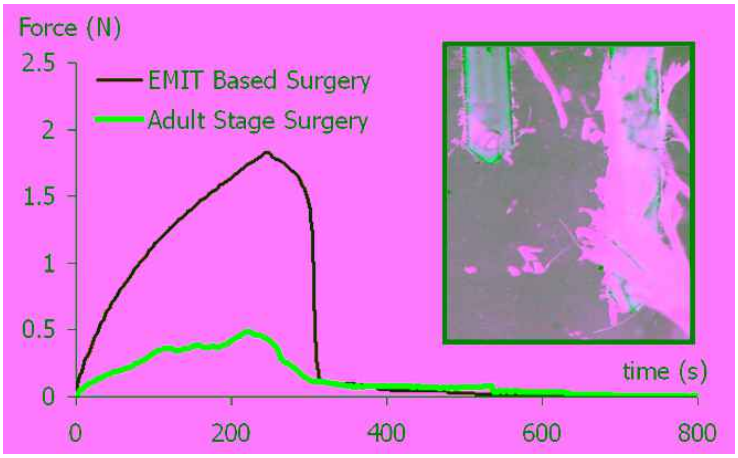

Figure 11: Typical force created with the pulling of the probe from the tissue. Pulling speed was 100µm/s. EMIT based insertion of probes provides a stronger mechanical attachment to the insect versus the adult stage insertion.

2.5 Comparison of Electrical Coupling In Vivo

As shown in the previous section, implanting the stimulation electrodes during the pupal stages of metamorphosis improves the mechanical coupling with the insect, which allows the implants to "fuse" with its neuromechanical system. The goal for such a neuromuscular stimulation system is to induce local potential in the muscular tissue of the insect in order to evoke a biomechanical outcome towards controlling locomotion. To achieve this, collection of electrons temporally shaped into pulse streams are injected into the neuromuscular tissue through coupled metal electrodes. At the interface where electrodes meet tissue, the electronic current is converted into a current of charged ions in the electrolyte. This conversion is a sensitive electrochemical process that limits the ability to form a stable interface with the neuromuscular system of the insect. Furthermore, in the case of vertebrates, the reactive response of the cells and tissue has been hypothesized to be an underlying mechanism for inconsistent electrical interface performance [Sza 03]. Therefore, it is necessary to analyze the electrical performance of electrodes implanted in insects to obtain a stable interface which can be further optimized to achieve a maximal biomechanical outcome with a minimal amount of injected charge.

2.5.1 In Vivo Electrochemical Characterization

Electrochemical measurements enable real time monitoring of the implanted electrodes to follow the tissue-electrode interface in vivo as a function of time {Wei 00]. This technique has the potential to shed light on the mechanisms at the insect tissue-electrode interface so that the charge transport for an enhanced biomechanical response can be facilitated. Below, electrochemical measurement methods were benefited from to monitor the tissue-electrode interface formed with the insect's neuromuscular tissue. Specifically, the improvement in charge injection capability was

investigated when implantations were done during the pupal stages of metamorphosis following Early Metamorphosis Insertion Technology (EMIT) as explained earlier. The obtained results indicate enhancements in the bioelectrical coupling formed with the tissue in pupal insertions, in parallel to improvements in the biomechanical coupling as explained in the previous section.

To characterize the electrochemical properties of the insect tissue-electrode interface, a three-electrode measurement system was formed with the insect. For this, four 75 µm thick PEDOT-PSS coated gold wire electrodes were soldered on a printed circuit board. The wires were cut at the tip at an angle of approximately 60º with the axis of the electrode exposing a 75x140 μm^2 elliptical gold surface. Details of the electrode preparation can be found in Chapter 4. To obtain a three-electrode measurement system, in addition to the PEDOT-PSS coated electrodes, a second PCB was prepared holding reference and counter electrodes (Figure 12). Both electrodes were constructed from 75 µm platinum wires. The reference electrode was coated with 65 µm Teflon with 500 µm exposed at the tip and on the counter electrode was an uncoated bare wire.

A Gamry Femtostat (FAS2) System was used for all the electrochemical characterizations. The impedance amplitude and phase were recorded through the electrochemical impedance spectroscopy (EIS) to characterize the charge transport mechanism. An alternating sinusoidal current with 25mV amplitude and zero bias voltage was used as the input signal. The impedance was recorded between 10Hz and 100kHz at 10 discrete frequencies per decade.

A cyclic voltammetry (CV) analysis was also performed to characterize the ability of the interface to store charge. A scan rate of 500mV/s was used to sweep the range between -0.6 and 0.7V vs. Pt to remain within the safe potential limits associated with hydrogen and oxygen evolution through electrolysis of water (water

window). The area under the CV curve was calculated as a qualitative indication of the amount of stored charge in the water window without any gas evolution.

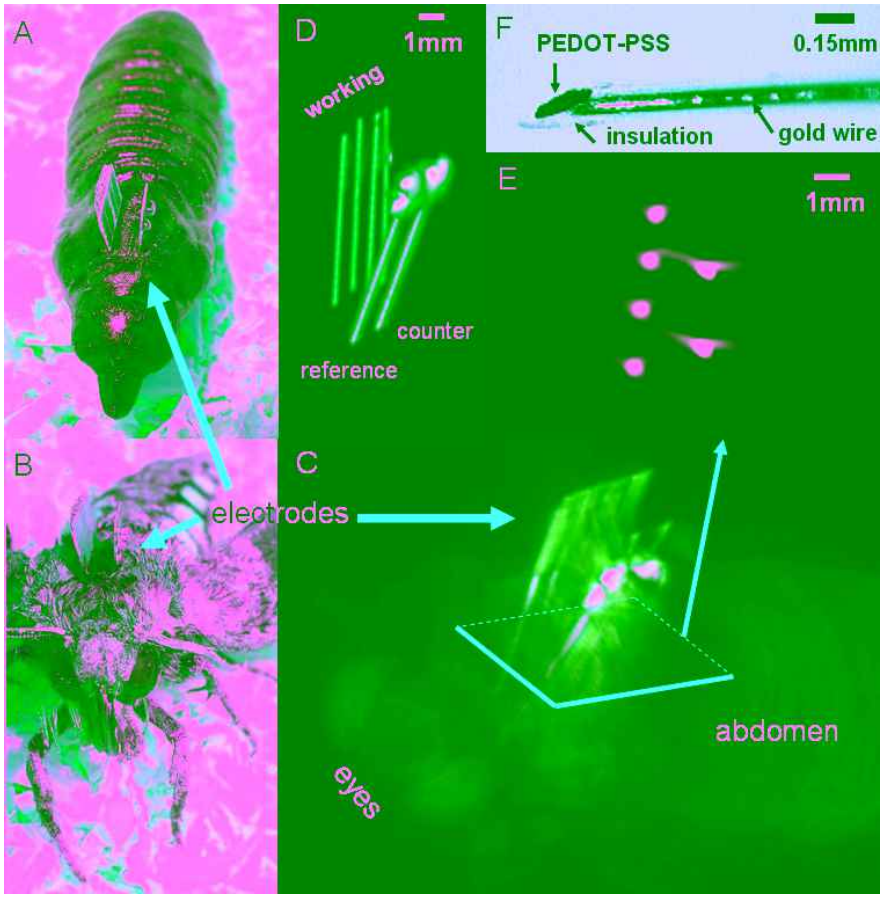

Figure 12: (A) Wire electrodes inserted to the pupae with exposed PCBs. Left-hand side PCB holds the four working electrodes whereas right-hand side PCB is for platinum reference and counter electrodes. (B) The post-metamorphosis emerged adult insect with the electrodes, (C) The reconstruction of the micro-computed tomography images reveal the relative locations of the electrodes in the insect where the tissue is semi-transparent. (D) shows the relative positions of the isolated electrodes from these reconstructions with electrode types as indicated. (F) Tip of the gold working electrodes are coated with PEDOT-PSS.

To study how much of this charge was actually injected into the tissue through biphasic current pulses, voltage excursion studies were run in addition to the impedance and potentiodynamic studies explained above. Studying the voltage

transients through the balanced biphasic pulse excursions allows one, in principle, to address the electrically safe charge injection limitations to keep the operation in the range in which no harmful reactant is released to the tissue. To generate charge balanced, cathodic first, biphasic pulse currents, a programmable stimulator was used (Multichannel Systems STG2008). Pulses of 2ms pulse width, 2% duty cycle and varying degrees of charges (between 0.2 and 20mC/cm^2) were sent to the electrodes in vivo. The resulting waveforms were recorded using an oscilloscope and then post-processed to calculate the actual voltage drop across the interface. This voltage was used to determine the maximum amount of charge that can be safely injected. The maximum permissible voltage drop across the interface was accepted to be -0.6V and 0.7V, which is the limit for hydrolysis.

2.5.2 Day by Day Change at the Interface

The neuromuscular tissue of invertebrates, particularly insects, undergoes extensive change during metamorphic growth as described in the previous chapter. During the metamorphosis, the entire musculature system is degenerated and formed *de novo* to be able to support newly emerging adult behaviors. When the neurostimulating electrodes are implanted in the insect during the pupal stages of metamorphosis, this change is also hypothetically projected to the interface formed between the tissue and electrode.

To characterize this change, the measurements electrodes were implanted into the developing dorsolongitunal flight muscles of the pupae seven days before the emergence and emerged with the adult insects following the completion of the metamorphosis (Figure 12). A typical X-ray micro-CT (computed-tomography) image of the electrodes in the muscle tissue can also be seen in Figure 12. During this time, the changes occurring at the tissue-electrode interface were characterized through EIS

and compared to the interfaces formed as a result of the surgery in the adult stage. The initial impedance curves observed right after the implantation changed noticeably over time for both pupal and adult stage insertions during the course of the measurements. A representative data set for one electrode is provided (Figure 13), exhibiting the change in both magnitude and phase spectra at the right after the insertion and the tenth day after the emergence of the adult insect. While the general shapes of the magnitude and phase curves look similar qualitatively, an upward shift was observed over time in the magnitude plots. The adult stage insertions caused an overall higher magnitude plot right after insertion, resulting in an average impedance magnitude of 11.6 kΩ at 1kHz, compared to 4.1 kΩ for pupal stage insertion. The magnitude shift over time was also larger with these adult stage implanted electrodes, especially at the higher frequencies, which is indicative of a larger resistive change. On the other hand, the nonlinear trend of the change over frequency for the pupal stage inserted electrodes indicates a resistive-capacitive (RC) effect introduced to the system after implantation, which manifests itself over the time course of development.

In vivo cyclic voltammetry allowed a qualitative assessment of the potentiodynamic charge storage behavior of the electrodes during the course of development. The CV data corresponding to the days presented in the EIS data are shown in Figure 13. The area under the CV curve, thus the value of store charged (Q_{stored}), decreased by time, while the shape of the CV data hardly changed. Q_{stored} values were decreased from 81 mC/cm^2 to 51 mC/cm^2 for pupal stage insertions, and from 50 mC/cm^2 to 38 mC/cm^2 for adult stage insertions. Hence, the change in CV can be correlated, especially with the increase in the low-frequency impedance, for the slower ramp waveform of CV concentrates more on the lower-frequency range. The CV data were supplemented by the voltage excursion studies comparing the degree of charge actually injected through the biphasic current pulses during development and

after emergence for both pupal and adult stage insertions (Figure 13). The voltage excursion data were in agreement with the CV data.

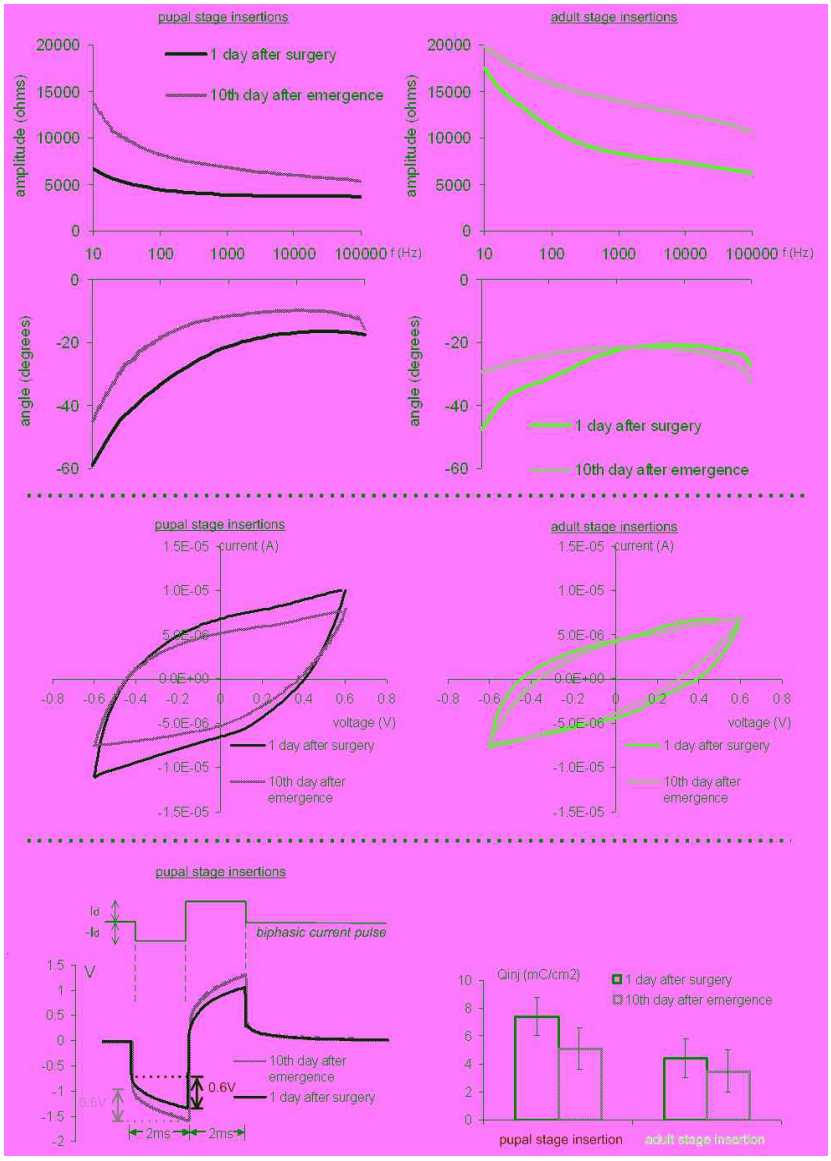

Figure 13: Representative data comparing pupal and adult stage inserted electrodes one day after the surgery and 10th day after emergence. The top graphs shows the magnitude and phase plots obtained through Electrochemical Impedance Spectroscopy. The graphs in the middle display the cyclic voltammetry results. The voltage excursion obtained by sending biphasic current pulses to the pupal stage inserted electrodes is displayed on the bottom. A similar waveform was obtained for adult stage insertions (not displayed). The 0.6V polarization voltage was selected as the level to determine the safely injectable amount of charge (Q_{inj}) as provided in the bottom right for both insertions.

To gain further insight into the change in the interface, day-by-day data of all the electrodes were presented starting 6 days before emergence until the 10th day after emergence (Figure 14). In neurophysiological experiments, it is a tradition to measure the impedance magnitude at 1kHz in order to set a quantitative standard for comparison across different electrodes and subjects as well as published literature because 1kHz is almost the fundamental frequency for action potentials. Therefore, the 1kHz electrochemical impedance magnitude change during this time course can be seen in Figure 14. Over the course of the pupal stage development, a monotonic increase was observed in the average impedance magnitude at 1kHz. The degree of increase was much less than that when the insect emerged. The variation of values about the mean also decreased during emergence. Implanting the electrode during the adult stage caused a higher average 1kHz impedance which followed a similar trend of change with pupal stage electrodes after the emergence of the insect.

The day-by-day changes in the amount of charge stored at the interface (Qstored) were extracted by using the area under the cyclic voltammetry curve and presented in Figure 14. The Qstored plots also exhibited a dramatic decrease over time in metamorphic development and emergence for implanted electrodes in both pupal and adult stages. The average charge storage was higher for pupal stage implants over the entire course by the final day of measurement with respect to the adult implants. Similar to the stored charge, the degree of charge injected through the charge-balanced biphasic pulses in the water window also decreased over time for both kinds of implantations while the pupal stage inserted electrodes were able to inject more charges into the tissue (Figure 14).

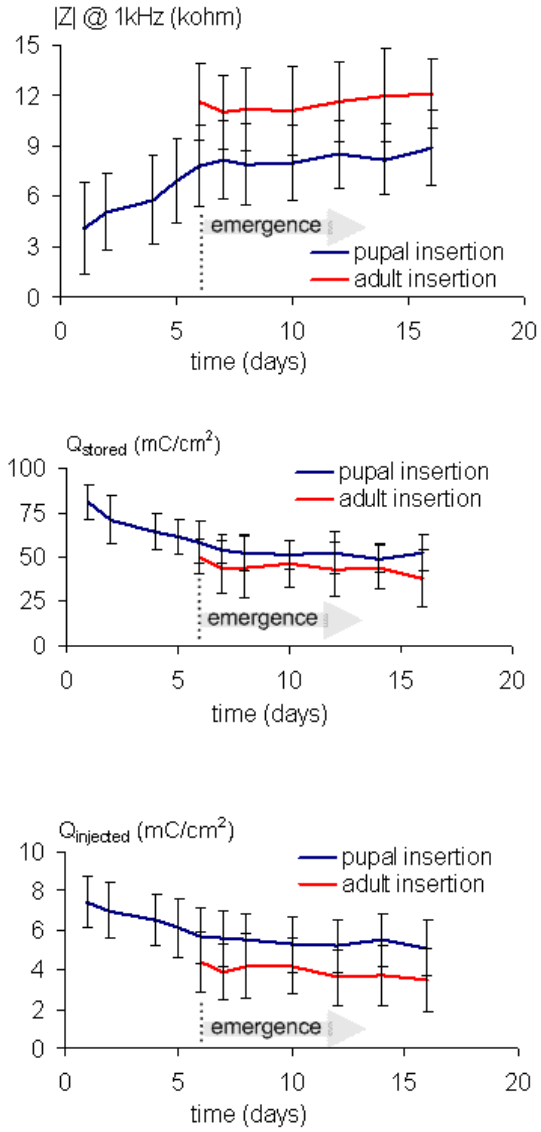

Figure 14: The averaged day by day data indicating the changes in the 1kHz impedance acquired through EIS (top), the amount of charge stored at the interface (Q_{stored}) from CV plots and amount of safely injected charges ($Q_{injected}$) with biphasic pulses obtained via voltage excursion studies. For all the graphs, the emergence occurs at the 6^{th} day for both pupal and adult stage insertions.

2.5.3 Modeling the Interface

The day-by-day changes in the electrochemical analysis can be further analyzed by fitting them to an equivalent circuit model, and the extracted circuit parameters can be used to develop a coherent analytical progression between charge injection capability of electrodes and the metamorphic development of the insect.

These results potentially help us to explain the time course of the bioelectrical changes occurring at the interface and why pupal stage inserted electrodes consistently perform better.

The equivalent circuit model (Figure 15) consists of two parts connected in series representing the pathway in which charge travels from the stimulation electrode to the ground electrode. The first part is the bioelectrical interface between the electrode and the tissue. The ability of the interface to transfer a charge to the tissue is represented by a resistive component (R_{ct}). More charges are transferred to the tissue for given voltage as R_{ct} decreases. Some charges that are collected at the interface cannot be transferred to the tissue due to the limitations imposed by the electrochemical interactions, and this is represented by a double layer capacitance (C_{dl}). Because the porous surface of the electrode consists of conformations that are a nonuniform mixture of these two effects, a constant phase element is also added to the circuit that represents this nonideality. Once transferred to the tissue, the charge follows a pathway either through the cell bodies or through the extracellular fluid surrounding the cells. The cumulative influences of these two mediums (cell membrane and the intra/extra cellular fluid) can be modeled as a parallel RC component. We also added an intermediate resistive component between the tissue-electrode interface and the tissue in order to model any encapsulation around the electrode formed by extracellular proteins. The additional resistances due to the interconnections are also embedded in this resistance.

To provide further insights into the developmental mechanism responsible for the improvement in the pupal stage insertions, we analyzed how the equivalent circuit parameters evolve over time (Figure 16). The charge transfer resistance R_{ct} consistently increased during metamorphic development. However, the degree of increase was reduced dramatically after emergence. The adult stage inserted electrodes

also underwent a similar increase during the subsequent days after emergence, but the initial resistance is much higher when compared to the pupal stage inserted electrodes.

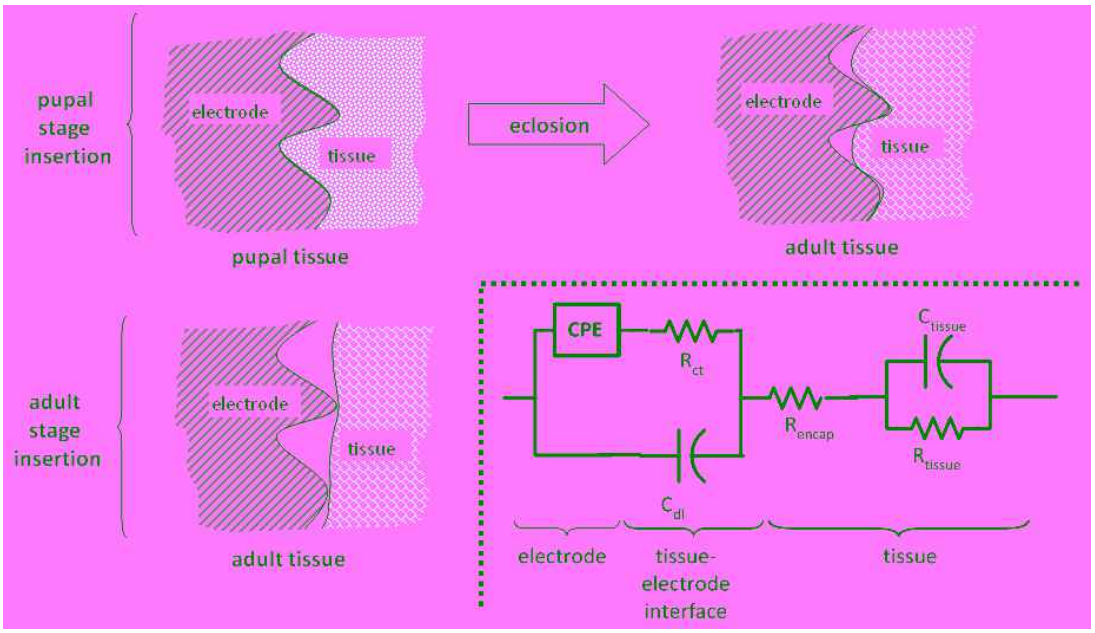

Figure 15: Cartoon illustration of the tissue penetration into the micro and nano scale indentations on the electrode for both pupal (top) and adult (bottom left) stage insertions. The equivalent circuit model representing the electrode-tissue interface, possible reactive responses of the tissue and the cumulative effect of extra/intra cellular resistances and cell membrane capacitances (bottom right)

This may be due to the penetration of the extracellular fluid and cell bodies deep into the perforations and indentations on the electrode (Figure 15). During pupal development, the unformed flight muscle of the insect demonstrates a gel-like, thin fluidic structure. The viscosity of the metamorphic tissue-preform increases over time, finally forming the solid fibrous flight muscles which have a similar structure to the skeletal muscles of vertebrates [Duc 00]. When the electrodes are implanted during the early pupal stages, due to its low viscosity, unformed tissue can easily reach into the micro and nanometer sized gaps and voids on the surface of the microelectrode, thereby increasing the contact area. The surface area directly in contact with electrodes decreases as the developmental formation of the solid muscle tissue progresses; however, a larger area results compared to the adult stage inserted electrodes in the

already developed tissue. Consequently, in parallel to the increase in R_{ct}, C_{dl} also exhibits a noticeable decrease until emergence, which stabilizes with a negligible change after emergence. The adult stage surgeries, on the other hand, resulted in a lower C_{dl}. Hypothetically, this may be because the already formed tissue was not able to penetrate into the electrode as efficiently, which potentially caused pupal stage inserted electrodes to store and inject higher amount of charges with respect to the adult insertions.

Figure 16 also illustrates that R_{tissue} (the resistance of the tissue and the extracellular fluid to charge flow) increased over time during metamorphic development, becoming well established after the insects emerged. A similar resistance value was observed after the surgical insertion in the adult stages, where the resistance value, again, stabilized around a constant value after emergence. This is consistent with the fact that the soft fluidic metamorphic tissue gets harder and more structured during pupal stage development. As the viscosity and the fibrosity of the tissue increases, the charge flowing from one electrode to the other experiences a more resistive pathway. This is because the fibrous tissue made of fatty acids and proteins has much higher resistance than the electrolytic interstitial fluid. Throughout this time, a gradual increase in C_{tissue} was also observed, which can be explained by the formation of new cell and muscle fiber membranes each consecutive day during development. The complete formation of the tissue caused the stability around a constant value of this parameter when emergence occurred. Pupal and adult stage values also followed a similar trend in this case.

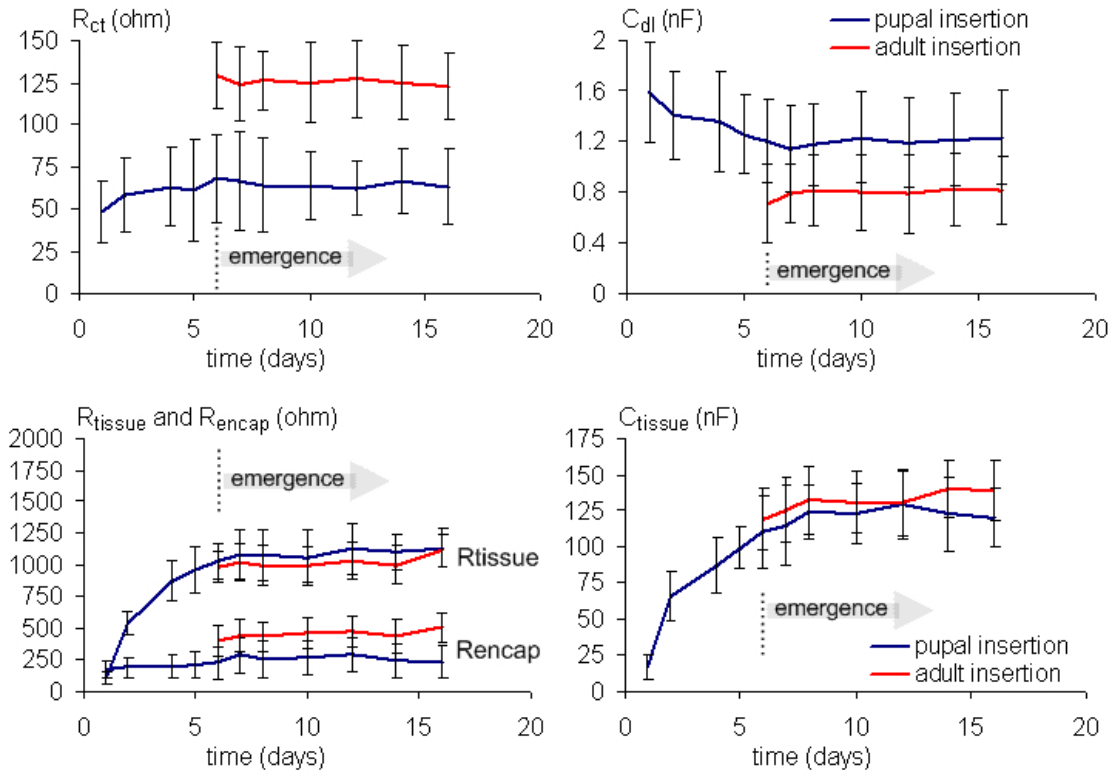

Figure 16: The averaged day by day change in the equivalent circuit parameters: charge transfer resistance (R_{ct}), double layer capacitance (C_{dl}), tissue related resistances capacitances (R_{tissue}, C_{tissue}) and resistance caused by the potential reactive response of the tissue and the cabling of the electrodes (R_{encap}). The emergence occurred at the 6th day for all the graphs for both pupal and adult stage insertions.

Extensive studies in the literature demonstrate that an encapsulating tissue sheath forms surrounding implantations to the vertebrate brain, thereby affecting the electrochemical characteristics of the electrode-tissue coupling [Gri 94]. However, in the case of the invertebrate muscle tissue, the expected tissue reaction is less because the immunoglobulins and astroglia that mediate immune reactions in the vertebrate brain are not present in insects. Instead, humoral mechanisms are utilized to identify and fight with foreign objects [Cha 82]. In accordance with this, we were not able to observe any inflammation or tissue disturbance at the sites of post experimental dissections in the persistent presence of the implanted electrodes as presented previously in Chapter 2. This observation was also confirmed with the extracted R_{encap}

values of adult stage insertions in this study (Figure 16), where the change in average values was negligible with respect to the orders of magnitude of higher values of change observed with vertebrate implantations [Gri 94, Joh 04]. The pupal stage insertions, on the other hand, caused a relatively lower R_{encap} where the surgery related tissue reactions were further minimized since the fluidic metamorphic tissue-preform was not disturbed mechanically by electrode insertions.

As suggested in the literature [Bui 98], we also made the fundamental assumption during the fitting procedure that the constant phase element was an electrode property and did not change significantly over time due to metamorphic development. This assumption was also supported by the consistency of the parameter estimation results obtained at the end of each fitting exercise. It should also be noted that we have not observed an important difference in the spatial distribution of the electrochemical measurements within the given tissue segment of dorsolongitudinal muscles, which suggests that the factors causing the change were uniform in this tissue segment.

CHAPTER 3
NEUROMUSCULAR SYSTEM OF LEPIDOPTERA

Insects demonstrate stereotypical behaviors triggered by environmental stimuli during their daily activities of finding food, reproducing, and escaping from enemies. Various signals are detected by their olfactory chemoreceptors, mechanoreceptors and visual receptors that are distributed from the tip of the antenna to the base of the wing and converted into orderly contractions of specialized muscle groups. These genetically programmed actions are established through the sensor to muscle neural pathways directly hardwired by the genes to each other during metamorphosis [Klo 02]. This hard wired sensorimotor reflex system acts like an autopilot inside the insect and helps it to obtain stable locomotion behavior (Figure 17). Therefore, control of certain behaviors, particularly locomotion, is possible and more straightforward with respect to the larger animals. Electronic systems can be implanted in insects to study and control their flight by actuating individual sensory, neural or muscular systems or combinations and also recording them (Figure 17). In this study, only the order of the Lepidoptera will be considered since *Manduca sexta* was chosen to be the model insect. However, the methodologies presented here could also be easily applied to other orders of invertebrates.

3.1 Anatomy and Function of Lepidoptera Flight Muscles

Unlike birds, insects do not have any built in muscles on their wings to maintain aerial locomotion. Instead, their specialized thoracic muscles move their wings, which function as passive airfoils. Sensory feedback is extensively used for both spatial orientation and flight stabilization by directly contracting the flight muscles. This contraction moves the wing through the movement of the thoracic

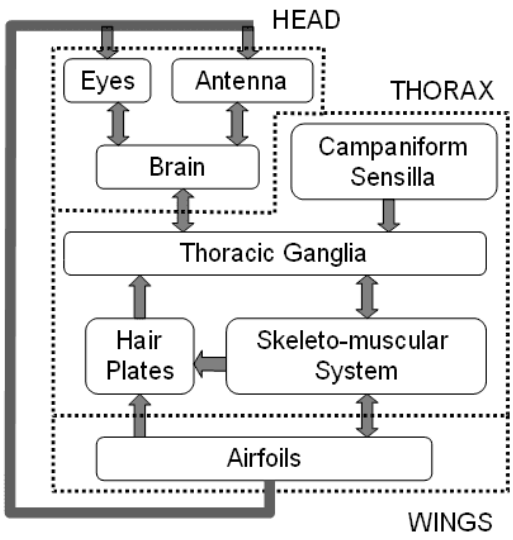

Figure 17: Functional and anatomical organization of insect's autonomous flight control system

exoskeleton and axillary sclerites, which are a number of mechanical joints at the points of articulation with the wing [Eat 71]. As a result, the aerodynamic forces creating propulsion are obtained. To modulate the flight maneuvers of the insect externally, these forces can be altered by manipulating the insect's motor system, which may be possible by applying either exterioceptive inputs to the sensor organs or proprioceptive inputs to various muscle groups (Figure 17). In the context of this study, only specific muscles in the insect will be focused on, as outlined below.

3.1.1 Indirect Flight Muscles

Occupying most of the space in the thorax, the flight muscles alone can comprise as much as 65% of the total body mass in most flying insects [Cha 82] (Figure 18). The basic wing beat is realized by the morphological arrangement of the main flight powering dorsolongitudinal (*dl*) and the dorsoventral (*dv*) muscles, and their interaction with the wing articulation geometry [Eat 71]. The insertion of muscles in the exoskeleton can be seen in Figure 19. The small movement of

articulation at the proximal end of the wing is transformed into flapping in which the wings act like a lever and are pulled by *dl* and *dv* muscles.

The contraction of the *dl* muscles changes the conformation of the thorax, causing the tergum to elevate and produce a downstroke by depressing the wing (Figure 20). When the *dv* muscles pull the tergum down, the wing is elevated to produce an upstroke. During straight flight, the *dl* and *dv* muscles contract approximately 180º out of phase. When turning, the *dv* muscles on the turning direction side are activated earlier with respect to the other side, which causes a reduction of thrust in that direction. Contraction of other smaller muscles that are attached directly into axillary sclerites, twist and rotate the wing to increase steering precision, as will be described later. However, the normal wing beats for turning and tilting can also be achieved by stimulating only the *dl* and *dv* muscles, without requiring actuation of other smaller flight muscle groups [Wen 02].

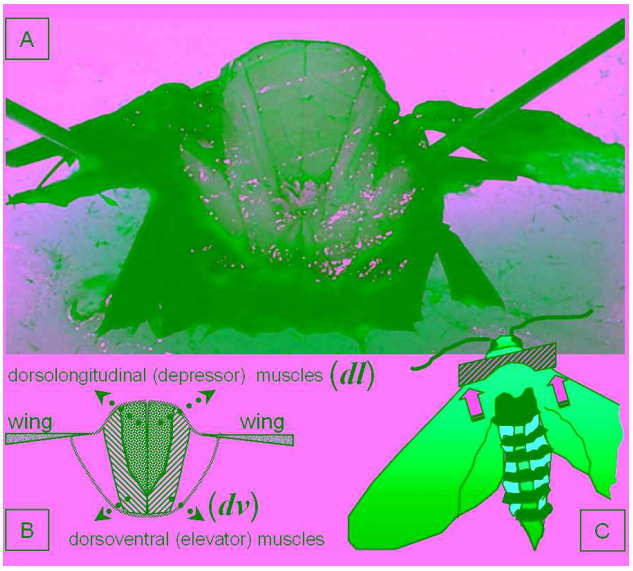

Figure 18: Dissection (A) of *Manduca sexta* thorax to identify dorsoventral (*dv*) and dorsolongitudinal (*dl*) flight power muscles as illustrated in (B). These muscles power and modulate the up- and down-stroke of *Manduca sexta* both for lift and steering. Dissection plane is in C.

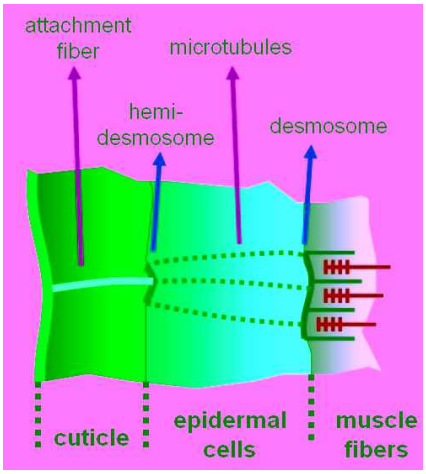

Figure 19: Muscle fibers are connected to the thorax to pull the wings by changing the conformation of the thorax.

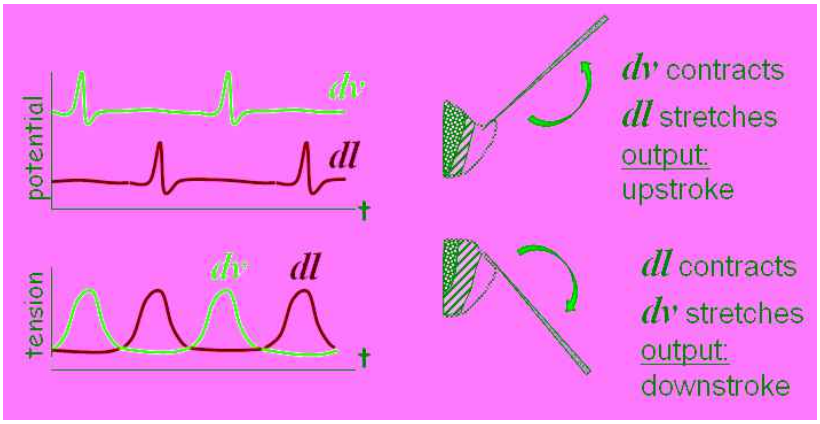

Figure 20: The up and downstroke of the wings are obtained with out-of-phase contraction of the *dl* and *dv* muscle groups.

3.1.2 Direct Flight Muscles

The indirect flight muscles are attached to the exoskeleton, which changes the conformation of the thorax so the wings can be moved up and down, whereas the direct flight muscles are attached to the base of the wings to bend them directly. Turning behavior is obtained by asymmetric alterations in the angle of attack, wing movements and deformation of the wings created by these direct flight muscles in which the four motions of the wings required for complex maneuvers during flight are created: promotion, retraction, pronation and supination.

The most important and functional direct flight muscle is the "third axillary muscle" connected to the third axillary sclerite (Figure 21). The contraction of these muscles causes the wings to bend independently of elevation and depression status as well as the remotion of the contralateral wing. This muscle group has three subunits (upper, middle, lower) located in the mesothorax, each innervated by a single motoneuron.

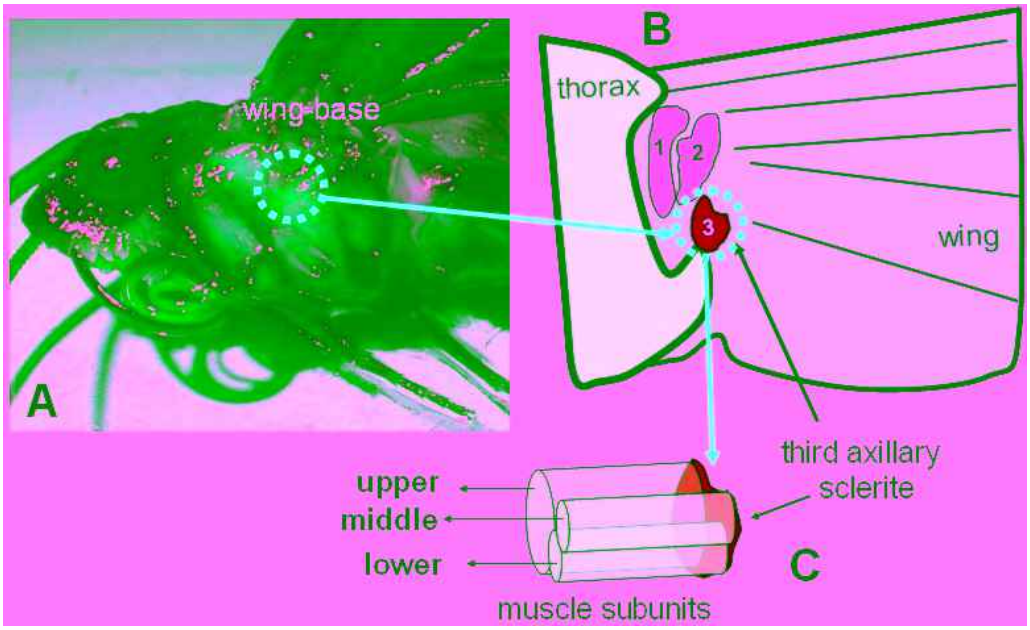

Figure 21: The third axillary sclerite of *Manduca sexta* in the wing base (A) with the relative position with respect to other axillary sclerites (B). Three subunits are attached to this sclerite forming third axillary muscles.

The third axillary muscles were studied in the literature in terms of their effect in turning flight, especially the relationship of the phase differences with indirect flight muscles [Rhe 87, Kam 71, And 04, Wen 93, Bha 74]. It was found that the phase difference between the upper unit of the third axillary muscle and *dv* muscle retracts the wing during both up and down strokes [Rhe 87, Kam 71, Wen 93]. The third axillary muscle phase was also found to have a correlation with the pitch angle [And 04] by modulating the appropriate upstroke movement of the wing. Because the

stroke plane follows the pitch angle of the body, the generated force by indirect flight muscles propels the insect in the direction affected by the third axillary muscle.

When turning towards the left, the left third axillary muscle is activated just before the *dl* muscle, creating a remotion. When making a right turn, on the other hand, the left third axillary muscle fires with the *dl* muscle. A similar phase relation was also observed symmetrically in the right third axillary muscle during a right and a left turn. The phase differences between the axillary muscles and the indirect flight muscles also occurred in decapitated animals, and this suggests that the phase control is independent from the signals coming from the brain [Kam 71].

3.2 Physiology of Lepidoptera Flight Muscles

The flight muscles of the *Manduca sexta* have a similar morphology with other skeletal muscles of invertebrates and vertebrates [Smi 84]. They are composed of muscle cells (fibers) that are made up of a number of myofibrils extending from one end to the other. Myofibrils contract through their molecular filaments that act like contractile machinery. Having two subgroups (thick filaments myosin and thin filaments actin), these filaments are highly ordered polymerized assemblies of protein molecules. In a typical myofibril, one can find repeated banded structures called sarcomeres, each of which is formed by overlapping myosin and actin filaments (Figure 22).

All these structures are located in a kind of plasma known as sarcoplasm, which is similar to the cytoplasm of the cells. In the flight muscles of insects, each myosin filament is surrounded by six actin elements with an overall ratio of three to one (Figure 23). This muscle is different from the other skeletal muscles of the insect body in which 12 actin elements surround each myosin with a ratio of six to one [Smi 84].

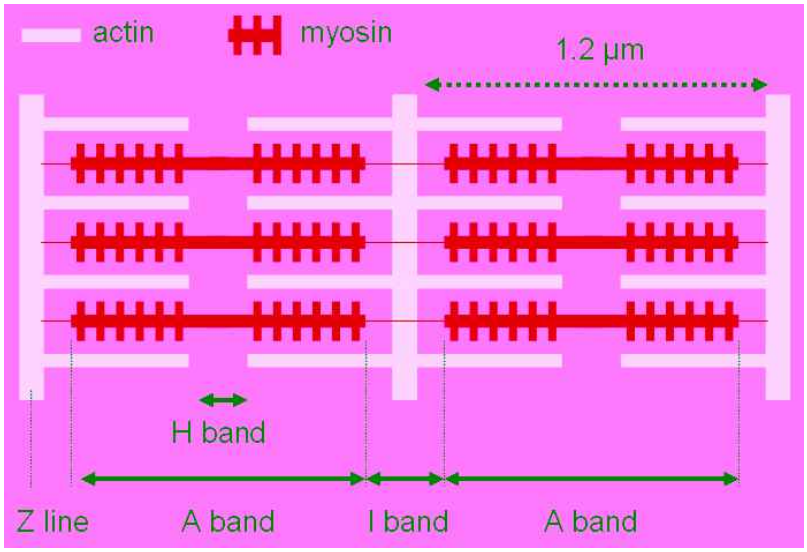

Figure 22: The longitudinal cross section of the skeletal muscle where the repeating bands of the sarcomere are indicated

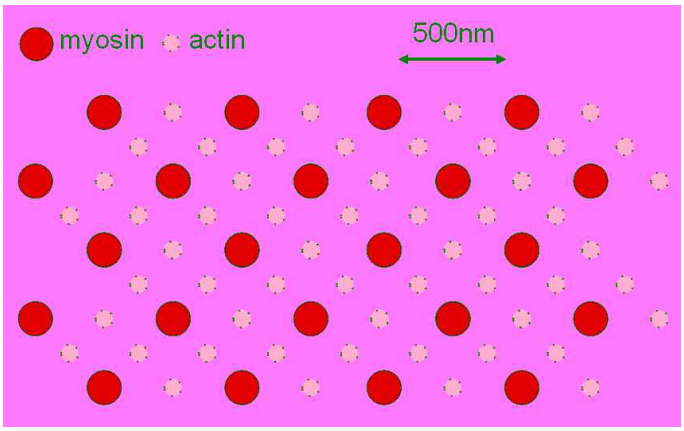

Figure 23: The transverse cross-section of *Manduca sexta* indirect flight muscles

Muscle contractions occur as a result of the actin and myosin filaments sliding past each other, shortening the "I" and "H" bands to increase their area of overlap (see Figure 22 for band descriptions). When energized with ATP, the myosin forms a cross-bridge as it attaches to the actin (Figure 24). With an additional supply of ATP, the head of the myosin molecule undergoes a conformational change that propels the actin-filament. The action ends with the detachment of the cross-bridge. This cycle

repeats many times during a regular contraction, each cycle resulting in a movement of 10nm for each head. With an average head number of 300 for each filament and a cycle speed of 5 times per second, filaments can be moved at a velocity of 15µm/s. Therefore, the myofibrils given in Figure 22 can be transformed from a fully extended to a fully contracted state in about one-tenth of a second [Cha 98, Guy 96]. The contraction action requires the existence of calcium (Ca^{++}) as a catalyst to form the cross-bridge. Therefore, it is not enough to have ATP molecules present near the filaments. The contraction happens as a result of a necessary Ca^{++} supply which is triggered by the nerve innervations.

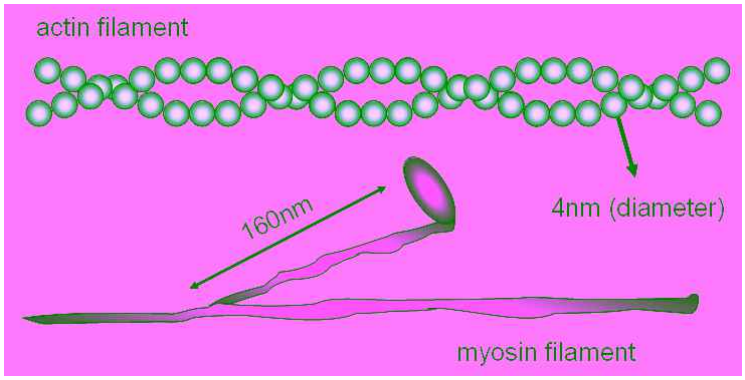

Figure 24: The molecular elements of the cross-bridge structure propelling the filaments of the myofibril

The sequential events that cause a muscle contraction can be summarized as follows [Sie 00]: the action potential coming from the axon reaches the terminal and innervates the muscle cell. At the neuromuscular junction between the neuron and the muscle cell, acetylcholine (ACh) is secreted as a result of the action potential. The secreted ACh travels to the muscle membrane and binds to the proteins that turn on the ACh-gated ion channels that let sodium (Na^{+}) ions in. The voltage change caused by an in-flush of Na^{+} ions triggers an action potential which not only travels along the myofibril membrane (with similar mechanisms to nerve membrane conduction) but

that also travels deeply into the myofibril, prompting the sarcoplasmic reticulum to release the Ca^{++} that it stores. With the presence of ATP, Ca^{++} triggers the formation of cross-bridges where the myosin head propels actin molecules. The Ca^{++} is rapidly pumped back to the sarcoplasmic reticulum via special Ca^{++} pumps that detach the cross-bridge, ending one cycle of the molecular machinery.

This event series causes a twitch contraction on the muscle (Figure 25). The twitch contraction starts with a delay when Ca^{++} ions are released with the incoming action potentials to the neuromuscular junction. This duration takes 2–3ms. During this period, the contractile molecular machinery starts to operate, increasing tension whose increase continues until the Ca^{++} ions are pumped back to the sarcoplasmic reticulum, decreasing the number of formed cross-bridges. As a result, the generated tension decreases by time and the generated contractile activity is fully terminated, eventually.

There are two ways to increase the created tension; first is spatial summation. Some nerve ends terminate more than one muscle fiber. In this case, the generated tensions from each fiber are summed up spatially and a larger tension is obtained. In the second case, each muscle fiber is excited rapidly before the preceding contraction is over. As a result, the next contraction is temporally added to the previous one, thereby increasing the generated force. As the frequency of the applied impulses increases, the contraction takes place in a smooth and continuous manner. This contraction is known as tetanus. The generated force saturates when all the actin-myosin cross-bridges are formed (Figure 26). The time course of a twitch muscle contraction of a *Manduca sexta* flight muscle was studied by Tu et al. [Tu 04], which is shown in Figure 25. According to this graph, the application of pulses faster than 25 Hz will cause temporal summation, and tetanus contraction will result in for frequencies in the order of 70Hz and faster.

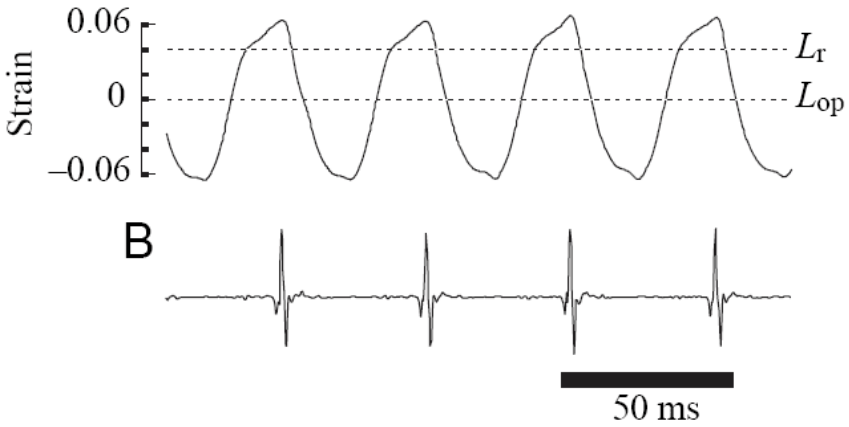

Figure 25: Natural twitch response of the *Manduca sexta* dl muscle with incoming neuromuscular spikes (from [Tu 04]).

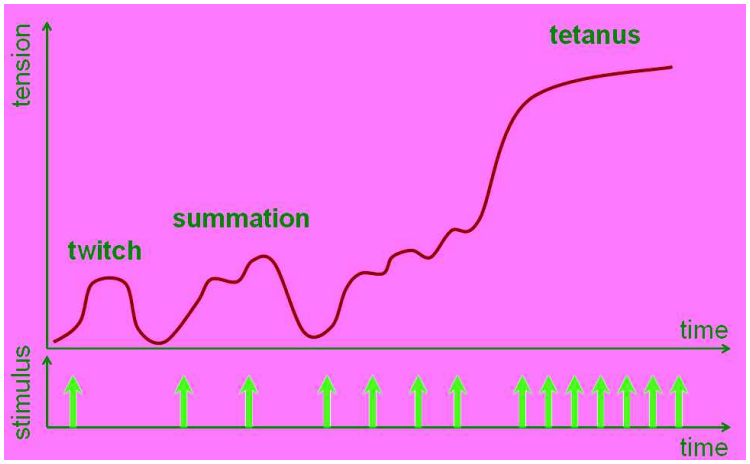

Figure 26: The summation of twitch responses with increasing frequency where tetanus is observed with higher frequency spikes

The tension obtained from the contraction is a function of the sarcomere length, for the strength of the contraction depends on the overlap area between the actin and myosin filaments. Maximum tension occurs when all the myosin heads are employed to form cross-bridges. This is demonstrated in Figure 27. When the myofibril is fully extended, the sarcomere is at its maximum length, and the actin-myosin overlap is minimal. When a contraction begins, more overlap occurs, which results in greater tension. After all the myosin heads are deployed, the tension does not increase any more and stays constant. With additional contractions, as the sarcomere

length shortens, the "H" band (see Figure 22) disappears and two adjacent actin filaments start to overlap, breaking some of the pre-formed cross-bridges, which results in a decrease in the tension that was obtained, which decreases even more as a result of more jamming up of the adjacent actin filaments.

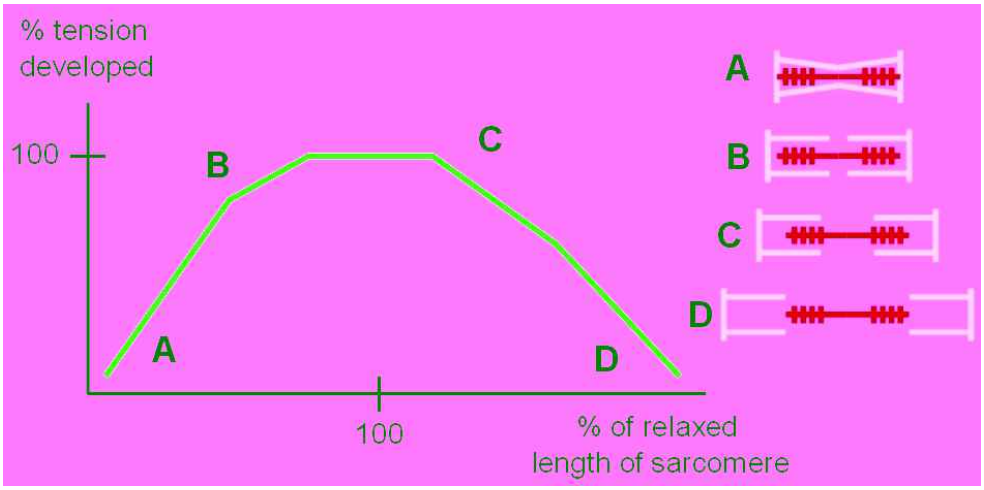

Figure 27: Tension developed with contraction and relaxation of sarcomeres. Relative positions of actin and myosin filaments are given for different parts of the curve (A-D)

The tension-length curve for a single muscle fiber can be seen in Figure 27. The whole muscle contains some connective tissue in addition to the many individual myofibrils; and there may be a slight time difference between myofibril contractions at different parts of the muscle. Despite these additional factors, the whole muscle exhibits a similar shape to the tension-length curve of the single myofibril with an expected increase in the dimensions.

The tension length curve of *Manduca sexta* was characterized by Tu et al. [Tu 04]. In their study, with the help of force transducers and translation stages, the researchers plotted the twitch length-tension curve of *dl* muscle in intact *Manduca sexta*. Their result shows that *dl* muscle has a steep and narrow shape more similar to vertebrate cardiac-muscle than to vertebrate skeletal muscle (Figure 28). The study

predicts several underlying mechanisms for this difference in function, one of which is the change in function of the troponin protein. Being connected to the actin filaments, troponin plays a role in the formation of an actin-myosin cross-bridge on the onset of the contraction. The other potential reason suggested in this study is the local extracellular concentration change around the muscle fibers. Regardless of the underlying factor, this property of the Manduca *dl* muscles allows large amplitude strains that can accommodate transient increases in wing stroke amplitude during turning behavior. The smaller basalar and axillary direct flight muscles change the conformation of the wing during rotation, which in turn creates a conformational change in the thorax, thereby affecting the strain of the *dl* muscle (under normal conditions, during turning behavior, the *dl* muscle follows a firing pattern similar to non-turning behavior) . The *dl* muscle can easily restore the muscle length changes to their steady state value and absorb the turning behavior induced changes in the strain. This regulatory property for stabilizing movement in response to perturbations is supplied by trading off maximum power generation, for the *dl* operates on the ascending region of the tension-length curve, rather than the maximum point.

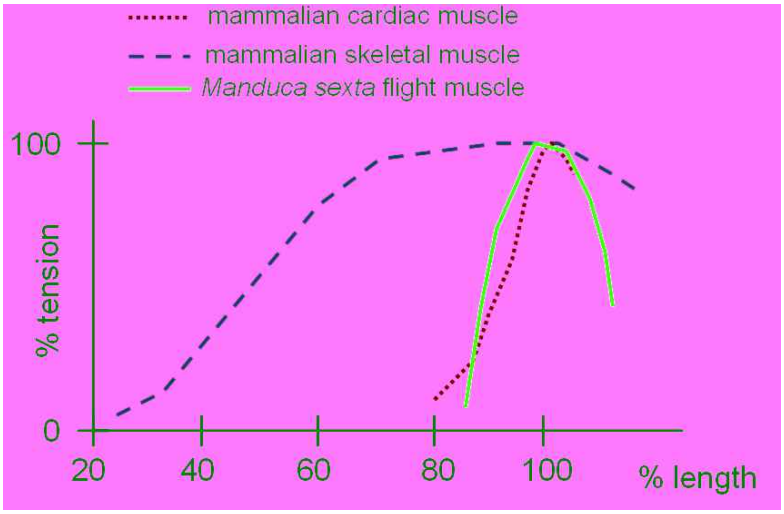

Figure 28: The tension length curve of *Manduca sexta* dl muscle in comparison to the curves of vertebrate skeletal and cardiac muscle (modified from [Tu 04])

3.3 Thermoregulation in Metamorphic Insects

Muscle actuation in insects is most efficient at a muscle temperature of 39°C as the catalyst driven biochemical pathways for sugar breakdown are optimized in this temperature range. The elevated in-flight thoracic temperature results in higher contraction frequency and power output per stroke required for take-off and flight. Therefore, a precursor heat is produced by the "shivering" of the insects, depending on the external temperature. The insect temperature quickly reaches thermal equilibrium according to the environment, for these insects are heterothermic endotherms [Hei 74, May 79]. In order to warm up, moths generate heat by shivering, vibrating their wings through small angles of 5–20°. The thoracic-temperature increases at a rate of 3–4°C/min by *in-phase* contraction of the flight muscles working against each other (Figure 29). In contrast, these muscles activate 180° out of phase during flight, resulting in lift. The rest of the body stays close to the ambient temperature at all times [Hei 71]. Thoracic heat production is not regulated during the warm-up period and is turned on completely to minimize the duration when the moving insect can be easily detected by predators but are not yet able to fly [Hei 71].

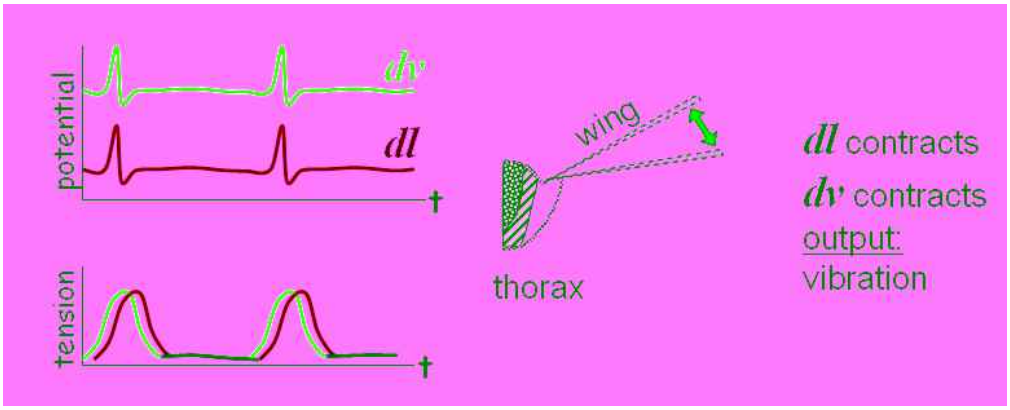

Figure 29: Illustrated action potentials and muscle twitch force at the flight power muscles and the resulting motor output at the wings. Compare preflight warm-up waveform here with flight at waveforms in Figure 20. Shivering and flight occur as a result of the phase difference between *dl* and *dv*.

3.4 Sensorimotor System of the Lepidoptera

As described at the beginning of this chapter, a moth's flight control system consists of sensory organs (antenna, eyes, hair cell, campaniform sensilla, and so on) connected either directly to the brain or to the ganglia distributed along the body (Figure 17). Environmental signals received through these sensors are converted into actions through the neuromuscular system after having being processed by the ganglia. The antennal and optical lobes are two of the most significant parts of the flight control systems during natural flight. It is well established that during natural flight, moths sense various chemical stimuli through their antennal lobe that are released from food sources, host plants or the opposite sex [Klo 97], and they maneuver towards targeted locations [Wil 91]. Using their compound eyes, they detect visual cues and use the related visual information to find and recognize these targets to direct their locomotion.

Moths feed by locating flowers and hovering in front of them, both of which are guided by visual cues and colors. It has been found that Lepidoptera can sense three colors (blue, green and ultraviolet) with the pigments in their eyes. Moreover, nocturnal moths can also use color in addition to achromatic, intensity related cues for detecting flowers at intensities as low as the starlight level [Cut 95]. The color vision of the insect is integrated into its functional flight control algorithms in order to achieve a stable flight through different steps of neuromuscular processing. The detected and perceived optical signals are evaluated via the sensory-motor integration centers which give commands to flight actuators to modulate the kinematics of flight. [Kel 03]

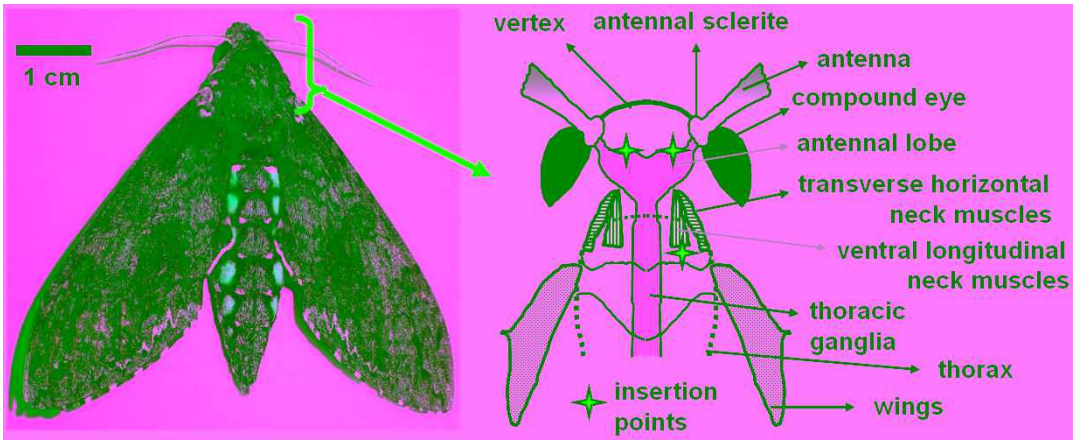

Figure 30: The anatomical description of *Manduca sexta* head-neck anatomy

The eyes of the insect are part of the exoskeleton. They can only be moved with the head to stabilize the retinal image of the target. During yaw, for example, the contraction of wing muscles is preceded by the rotation of the head towards the aimed direction through the neck muscles. Therefore, the neck muscles are directly involved in motion directivity [Mil 92] by controlling the motion of the compound eyes. In conclusion, the antennal and optical lobes (thus the neck muscles) are the two key sensory systems used to control locomotion in the hawkmoth *Manduca sexta* (Figure 30).

CHAPTER 4
DEVELOPMENT OF IMPLANTABLE TECHNOLOGIES

Developing the technological platforms to be embedded on the insect proposes important engineering challenges. These platforms can be analyzed under two categories: the probes that are implanted in the insect tissue to form an electrochemical bridge between the insect's biological processes and the electronic control systems, and the backpack holding the electronic communications and control systems that will form a bridge between the probes and the external world. For the aforementioned categories, the most important engineering challenges are (1) the efficient injection of the charges in the insect's tissue to obtain a biomechanical output and (2) the low-power and low-weight systems payloads that will operate for an extended duration with minimal loading effects on locomotion performance that result from the induced weight.

4.1 Microprobe Design and Fabrication

The microprobe is the interface between the neuromuscular system of the insect and the control electronics that couple the two media to each other. Stimulating probes are composed of three layers: substrate, metal and insulation. The choice of each of these materials can be optimized considering three criteria: biocompatibility, electrode tissue impedance and ease/cost of microfabrication. The geometrical design of the stimulation probe along with the material selection for the actuation pads and the substrate material are the most important concerns in the design and manufacturing process. In this chapter, different materials were analyzed and compared for optimal operation. The geometrical properties of the probes were determined according to the tissue segment targeted.

4.1.1 Selection of the Electrode Material

The optimized selection of the electrode metal for stimulation is an important criterion in the design process. In the selection process, factors such as charge injection capacity, electrochemical stability and mechanical strength should be considered. The metal selected for the electrode should be able to deliver current at high charge densities without corroding or dissolving in saline solution.

The interface between the electrode metal and the tissue (considered to be an electrolyte in this case) is critical in terms of stimulation performance. The electrode-solution interface and related interfacial processes can be modeled using electrical equivalent circuit elements, which can be characterized using Electronic Impedance Spectroscopy (EIS) [Fra 05, McA 95] as will be described later in more detail. Cyclic Voltammetry (CV) traces can also be used to measure the amount of charge transferred during oxidation-reduction reactions as the electrode potential is swept.

In a simplified and generalized model [Fra 05], the processes occurring at the electrode-electrolyte surface involve a double layer capacitance on the interface, charge transfer resistance, diffusion layer impedance and the resistance of the solution (Figure 31). This model may vary slightly depending on the electrode and electrolyte properties. The *double layer capacitance* is formed as a result of the electrostatic interactions among the surface metal atoms and the electrolyte ions through the intermediate adsorbed polar molecules attached to the surface metal atoms. The amount of injected charge is a strong function of this capacitance. The *charge transfer resistance* is caused by the electrochemical reactions that form the electrons that are injected in the electrolyte solution. The resistance depends on the reaction kinetics as well as the speed with which reactants and products diffuse towards and away from the electrode. The diffusion of ions in this way causes an impedance known as the *Wardburg impedance* [War 01], which can be modeled as a constant phase shift

element. This specific impedance is low for higher frequencies because ion concentration changes occur very quickly and diffusion is not as significant. However, when the applied frequency is low, diffusion is more effective, for the reactants and products diffuse further. Finally, the charge transfer from anode to cathode through the solution creates an *electrolyte resistance*. Depending on how bad a conductor the electrolyte is, this electrolyte resistance becomes more significant. A reference electrode located very close to the double layer capacitance can be used to measure and compensate for this parasitic resistance.

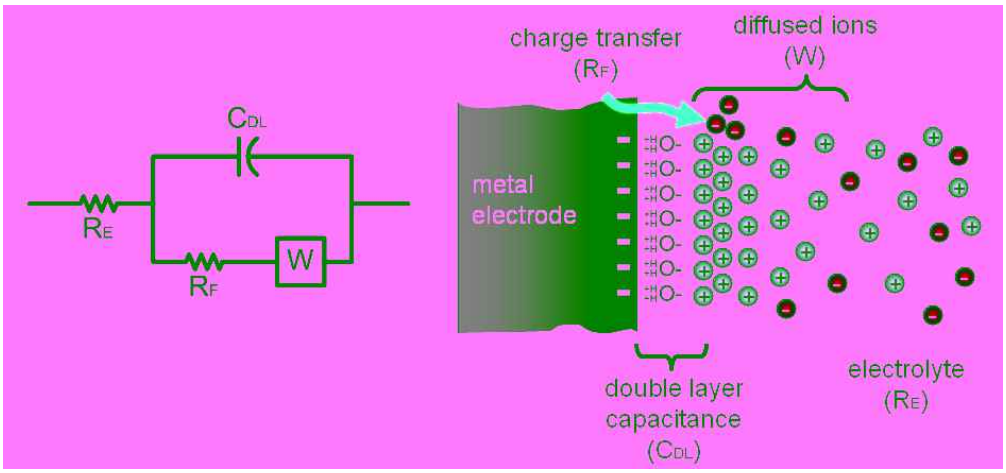

Figure 31: Electrical model of the electrode-electrolyte interface with the physical components of the model indicated.

The operation of the electrode-electrolyte interface and charge transfer is electrochemical and highly dependent on the applied voltage (Figure 32). Until a limit potential is reached, the interface acts capacitively and applied voltage only collects more ions in the interface (no electrochemical reactions are observed). The double layer capacitance is parallel to the charge injection resistance which is in series with the Wardburg impedance (Figure 31). When no Faradic current is present, the charge injection resistance becomes infinite and the double layer capacitance dominates. When the voltages go beyond the limit of Faradic current, the double layer capacitance

becomes infinite and the charges are transferred from the metal to the solution. This electrical current results from electrochemical reactions. If the reaction is not reversible, the current causes metal electrode corrosion, so the performance is adversely affected; hence, it is unsafe to operate outside the capacitive region for corroding electrodes such as iron. Ideally, to solve this problem, non-corroding metals should be used for stimulation purposes like Au, Pt and IrOx (Table 2).

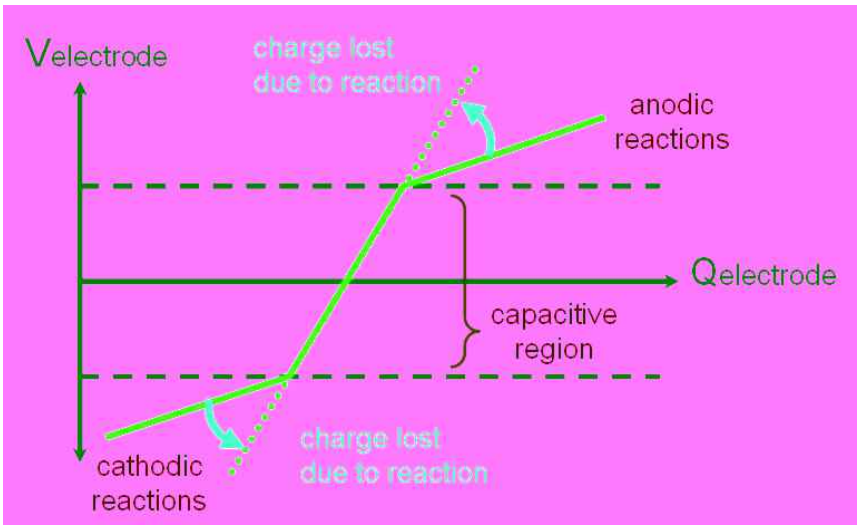

Figure 32: Diagram illustrating the concept of capacitive and charge injection regions for varying electrode voltages

Table 2: Charge Injection Capacities for Different Metals in the Literature

Metal	Charge Injection Capacity (mC/cm^2)	Reference
Gold (Au)	0.020	[Bec 99]
Platinum (Pt)	0.075	[Wha 06]
Platinum Iridium (PtIr)	0.3	[Cog 05]
Titanium Nitride (TiN)	0.87	[Wei 02]
Iridium Oxide (IrOx)	3.9	[Wei 02, Cog 05]

Gold electrodes have been used initially for the experiments presented here because it is easily accessible and is a soft/flexible metal. Being a noble metal, the following reactions were listed for the gold in electrochemical equilibrium in aqueous media [Pou 66].

$$2Au+3H_2O \Leftrightarrow Au_2O_3+6H^++6e^- \quad E^o=1.457V$$

$$Au_2O_3+H_2O \Leftrightarrow 2AuO_2+2H^++2e^- \quad E^o=2.630V$$

where both products and reactants are solids. Therefore, the redox reaction has a reversible behavior.

It has been shown that other chemically inert metals like Pt, Ti, Ir or their compounds (such as IrOx) have a higher charge injection capacity with respect to Au (Table 2). Although the deposition of Au over the copper is easier, and an integrated part of the processing technology for flexible printed circuit technology (as will be explained in the next section), these noble metals can also be electroplated over gold for performance comparison, which will be discussed in Section 4.1.4. Beyond in vitro characterization, an in vivo electrochemical analysis should also be performed to quantify the injected charges for these materials because in vivo processes [Car 92] such as fluid circulation inside the insect may improve performance.

4.1.2 Wire Electrodes

Wire electrodes have been used for a long time to stimulate and record from the neuromuscular system of invertebrates before the semiconductor micromachining became a convenient methodology for fabricating microscale electrodes. For the studies done for this dissertation, these probes were also used due to the easy availability and low fabrication cost. Silver and gold were used as the electrode materials because of low flexural rigidity, proven biocompatibility, low cost and commercial availability [Rou 01]. Although their chemical stability that prevents

electrolytic corrosion is not as good as some other noble metals (such as titanium or iridium), silver and gold were more advantageous because the softness and flexibility of the wires were required to match the forces encountered mechanically during the mechanical motion of the insect's body parts.

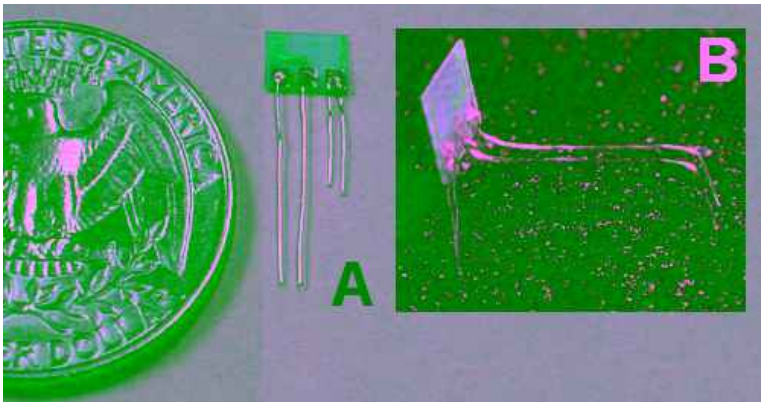

Figure 33: Wire electrodes soldered on a PCB (A) and bent into a three-dimensional shape

To build the wire probes, either gold or silver (typical diameter 200µm, A-M Systems, Inc.) was soldered on a miniature FR-4 board (typical size 4x5mm^2) and the wires were bent to a three-dimensional shape depending on the targeted location (Figure 33). The shaping of the wire electrodes for the antennal lobe and the neck muscle insertion, for example, can be seen in Figure 8. Printed-circuit-board fabrication techniques were used to manufacture the stimulation probe body seen in this figure. The copper traces (200µm) on the probe body match a FFC (Flat Flex Cable) connector (Figure 61). This connector joins the control electronics to the wire electrodes through the PCB body of the stimulation probe. The probe was designed to be surgically inserted in the insect during the pupal stage, where the wire electrodes are located in the tissue and the FR-4 board body is exposed outside (Figure 8). The control electronics are connected to the probe after the adult insect emerges (Figure 73). Therefore, the same control electronics can be re-used several times for different

insects. The actual probes, though, are disposed with the insects when they complete their adult life cycle. The typical weight of the manufactured probe with soldered wire electrodes was in the order of 30–50mg.

4.1.3 Microfabricated Electrodes

In the last fifteen years, micromachining technology enhanced neuroprosthetics research by providing tiny electrical probes that can be implanted into neural tissue and thus create and measure evoked functions. Moreover, recent advancements in silicon technology, in particular CMOS based electronics, have enabled large amounts of information processing and storage capability to fit into mm^3 volumes. Combined together, these technological achievements in micromachining and CMOS have great potential to study insect locomotion in a more detailed way with respect to the wire electrodes.

In order to electrically excite the neuromuscular cells at the targeted locations, all-silicon rigid microprobes were initially fabricated. These microprobes provide higher resolution stimulation by scaling electrode size (down to hundreds of nanometers) enabling higher density probing. A sample probe can be seen in Figure 34 for targeting the indirect flight muscles located in the dorsal thorax of the *Manduca sexta* (Figure 35) As explained in Chapter 2, these probes failed either during insertion or during the actual experiments because of their inherent fragility, yielding around 10% successful insertions.

Therefore, probe flexibility is a required design property for wider probe geometries, for the probe has the potential to affect the biomechanics of muscle contraction. Conversely, muscle contraction can cause impact and high strain damage to the probe. Moreover, the fragility of the probes, while handling during insertion and throughout the experiments, is less of a concern with a flexible probe. Polyimide was

chosen as the base material instead of silicon because the mechanical flexibility of polyimide could be approximated to the flexural rigidity of the insect muscles, thereby minimizing the relative stress between the implant and the tissue. For an all-silicon probe with a similar stiffness to the flexible probe, a silicon thickness of 30 µm would be required. Furthermore, polyimide is a proven biocompatible material for long term chronic neuroprosthetic applications [Rou 01].

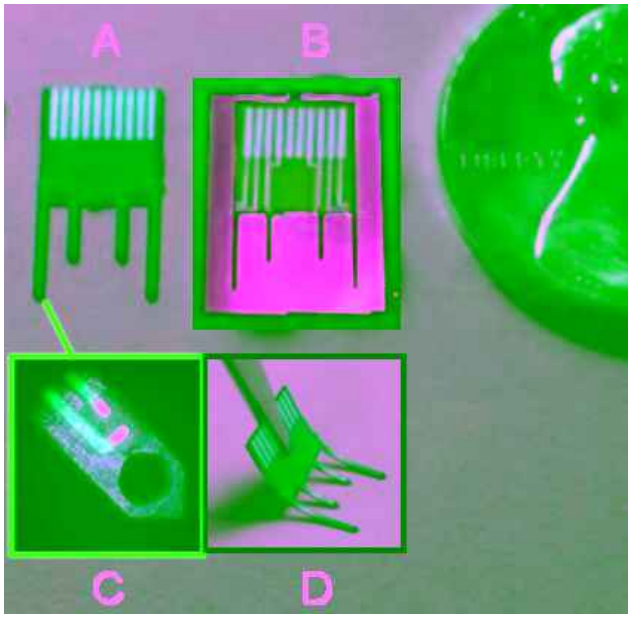

Figure 34: The flexible polyimide probe (A) and silicon probe (B). The close-up view of the tip in (C) with the hole for muscle growth, and the flexibility of the probe (D) are also given.

Polyimide based microelectrodes can be fabricated through conventional cleanroom processing, and a typical process flow can be found in Rou et al. [Rou 01]. However, a novel way of fabricating polyimide based electrodes is described in the next section. All the polyimide based microprobes used in the context of this study were fabricated following this novel procedure.

4.1.4 Flexible Printed Circuit Board based Electrodes

EMIT surgical procedure may benefit extensively from metamorphic development to couple electrically active microelectrodes into the electrically responsive tissue of the insect to enable an automated mass production line as mentioned earlier in Chapter 2. The cost of microfabricating the metamorphosis-implanted electrodes on this production line is an important concern, especially for the biobotic applications in which a large number of insects would be employed.

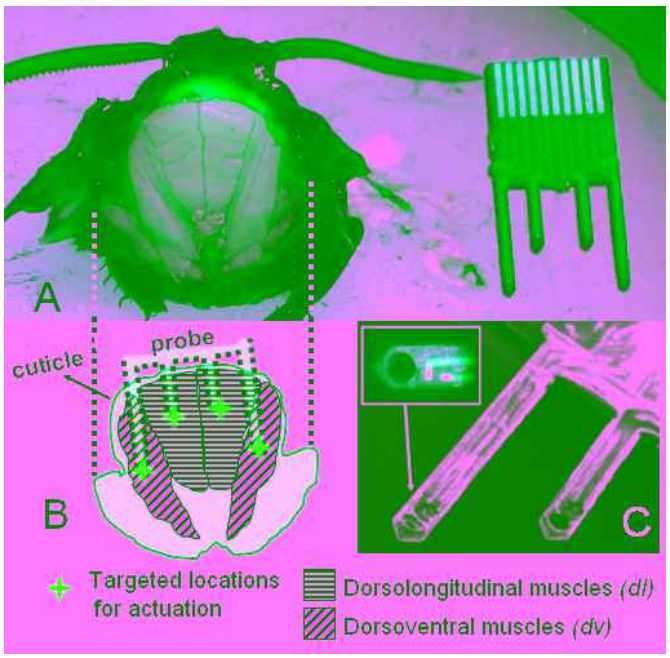

Figure 35: Cross-section (A) and illustrated diagram (B) of the flight muscles powering the up- and down-stroke of *Manduca sexta* wings. The tips of the flexible probe in (A) target the flight powering muscles *dl* and *dv* (B). SEM image of the flexible-probe tip with expanded image of the ground and actuation pads can be seen in (C). The hole at the tip is opened for muscle growth.

Nevertheless, the design constraints of these invertebrate microelectrodes can be relaxed with respect to vertebrate microelectrodes, potentially enabling a reduction in the cost of fabrication. The vertebrate implantable microelectrodes are often designed to be used in chronic long term applications. Hence, the endurance of these

devices is an important design criterion during the implantation process and against the long term reactions from the biochemical agents that exist in biological tissue. In addition, higher sensitivity and specificity are required to obtain a successful outcome from the sophisticated vertebrate motor control system. Therefore, implantable stimulating microelectrodes are often produced following high-cost conventional thin-film processing technologies derived from semiconductor fabrication techniques [Wise 05]. And even then, the lifetime and reliability of microelectrodes is limited in vertebrate systems. On the other hand, immunoreaction is less of an issue for invertebrates, and the lifespan of the electrodes in tissue is relatively unimportant due to the shorter lifespan of insects. Moreover, depending on the electrical actuation and movement control scheme, lower spatial resolution for site specificity can be tolerated due to the relatively less intricate insect motor control system of the insect. This difference allows the use of larger pad areas with further inter-pad distance. These features provide the opportunity to fabricate implantable electrodes for invertebrates using highly standardized and commonly available flexible printed circuit board (flex-PCB) technologies where the production cost is optimized for high volume markets. Polyimide, the most common substrate for flex-PCB production, is a biocompatible material [Rou 01]. Polyimide substrates are often covered with copper as a conductive layer, which can easily be further coated with gold for biocompatibility as a standard part of the flex-PCB production line. In addition to these, the electrode size (50 to 100µm on each side) and density (50 to 100µm pitch size) obtained with conventional flex-PCB technologies can be successfully accommodated for insect-biobot applications. Using this manufacturing technology, the circuit components for control and data handling can also be directly assembled on the non-rigid microelectrode substrate, which is beneficial for reducing the size, power, and noise of the electronics.

So far, the use of flex-PCB technology in neural engineering research has been limited to manufacturing flexible interconnects between silicon-based microelectrode arrays and control microelectronics [Nor 02]. This technology also has been incorporated in *in-vitro* culture dishes to "record" the electrical activity of cultured cardiac-cells [Gio 06]. The fabrication and use of implantable *in-vivo* flex-PCB "stimulation" electrodes, however, require further analysis and modification.

The study described below reports on the improvement of electrical and electrochemical behavior of flex-PCB probes that will be used as implantable insect tissue stimulation microelectrodes. We present the in vitro characterization of morphological, electrical, and electrochemical properties of these surface modifications through scanning electron microscopy, cyclic voltammetry, electrochemical impedance spectroscopy, and current-pulse induced voltage excursions in phosphate buffered saline solutions.

4.1.4.1 Flexible Printed Circuit Board Fabrication.

The design layout of the stimulation electrodes were prepared using Target3001 software (Ing.-Buero FRIEDRICH, Germany) and the generated Gerber files were submitted to Hughes Circuits, Inc. (San Marcos, CA, USA) for production. For the substrate, 100µm (~4-mil) thick Kapton® polyimide film (AP8545, DuPont^{TM}, DE, USA) was used, which was laminated with 17µm (0.5oz/ft^2) thick copper on one side only. The thinnest available material was 50µm (2-mil) thick polyimide (AP7156, DuPont^{TM}) with 0.25oz/ft^2 of copper. The patterned traces on the copper layer were coated with 20µm of liquid photo imageable (LPI) soldermask (PSR 900 FXT, Taiyo, Inc., NV, USA) for insulation. The minimum allowable width of the traces was 75µm (~3-mil) with a line-to-line spacing of 75µm. Next, openings were made in the insulation through laser etching where the stimulation pads are desired. The laser etching of LPI enables insulation openings in the order of 75µm (3-mil) on each side.

The outer shape of the electrodes was defined using laser milling to fit into a FFC (flat-flex-connector). The copper pads were coated using both electroplated (1.5µm thick, ASTM B 488 type III Grade A) and electroless nickel - immersion gold (ENIG) (125nm and 2.5µm thickness respectively) for biocompability. We used pads of two sizes: 75×150µm^2 and 100×100µm^2. The fabrication layers can be seen in Figure 36. In some probes, we used orifices that had been opened at the tip with laser drilling. The tissue growing through these orifices provides mechanical anchoring in in-vivo setups, but that is outside the scope of this dissertation.

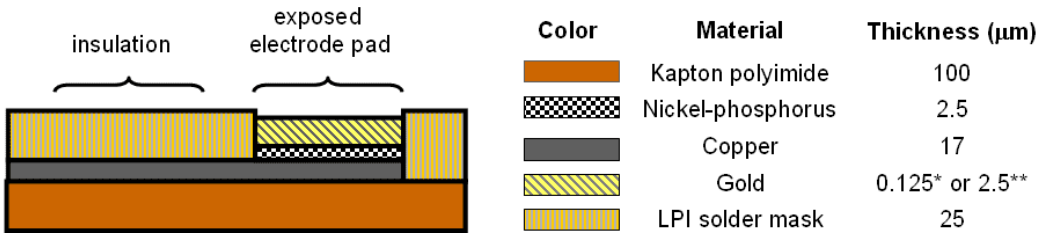

Figure 36: Cross-section diagram of the one-layer flexible circuit board electrode (*immersion gold, ** electroplated gold). Nickel-phosphorus layer is only for immersion plating (ENIG).

4.1.4.2 Cleaning of the Laser Ablation.

Laser drilling and milling have been widely used to define miniature structures on flex PCB substrates. Carbon rich debris has been known to occur as a result of photothermal and photochemical mechanisms leading to the ablation of the polymer [Cou 98]. To remove the laser ablation debris, we cleaned the received probes ultrasonically by soaking them in acetone and then isopropyl alcohol (IPA) baths, each for 10 minutes. Acetone and IPA are known to affect the molecular orientation of the polyimide; meanwhile, the ultrasonic pulsing has the potential to irritate the deposited gold surface, so we performed an electrochemical analysis to characterize the effect of the probe cleaning procedure.

After the flex-PCB was manufactured, the electrodes had an extensive amount of surface debris, especially at the laser patterned tips as a result of carbonization and charring of the ablated organic material (Figure 37). It is very likely that such contamination adversely affects the biocompatibility of the substrate and the electrochemical quality of the formed tissue-electrode coupling; therefore, it needs to be removed before tissue implantation. We were only able to "partially" remove the debris by just wiping the electrodes with acetone/alcohol or leaving the electrodes in acetone and alcohol overnight without applying any ultrasound, both of which are the most common cleaning techniques when implanting micromachined probes into tissue. It has been reported in the literature that it is possible to dry-clean the debris through applying relatively weak laser pulses or plasma-ashing [Kor 88]. Because it is costly to have access to the required laser and plasma etcher, and both methods can deform the patterned shapes, wet-cleaning was used to clean the debris. The contaminated and cleaned probe tips after ultrasonic acetone and IPA cleaning can be seen in Figure 37. The EIS and CV measurements revealed that the ultrasonic cleaning process had an insignificant amount of degradation in the electrochemical performance of the gold surface (Figure 37). Therefore, it is safe and necessary to incorporate a final ultrasonic cleaning step in the production of the flex-PCB microelectrodes in order to use them as neuromuscular stimulation probes.

It may also be possible to use the same laser for ablation to remove the debris. However, this requires adjusting the intensity of the laser pulses to be reapplied for cleaning after the ablation process, for it is often difficult to have access to and be able to modify the tools in the commercial foundries for research purposes; this option was not considered in the scope of this dissertation.

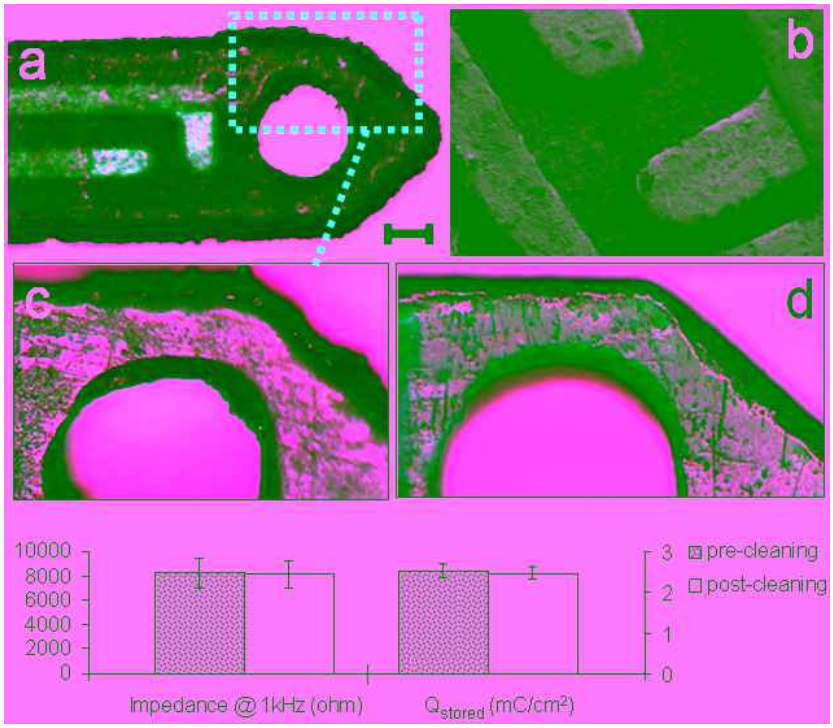

Figure 37: (a) Ablation debris caused by laser milling and drilling, scale bar: 100µm (b) SEM of contaminated gold pads (c,d) removal of the debris with ultrasonic cleaning. The stored charge and impedance at 1kHz is given at the bottom for pre- and post cleaning.

4.1.4.3 Electrochemical Analysis Methods.

The coatings on the electrodes were visually analyzed through optical microscopy (Olympus BHMLJ) and scanning electron microscopy (SEM, Zeiss Supra). The roughness parameters (roughness average and surface curtosis) were obtained using a Wyko NT9100 Optical Profiling System. The body of the electrodes was shaped to fit into an FFC connector, enabling external electrical connection for both electrochemical deposition and characterization. Gamry Femtostat (FAS2) was used for all the electrochemical characterizations where a 0.1M PBS buffer was used as the electrolyte. We used a 2.5×2.5 cm^2 platinum sheet as the counter electrode and an Ag|AgCl electrode as the reference. The complex impedance was recorded through electrochemical impedance spectroscopy (EIS) to characterize the charge transport mechanism. An alternating sinusoidal current with a 25mV amplitude and zero bias

voltage was used as the input signal. The impedance was recorded between 10 Hz and 100 kHz at 10 discrete frequencies per decade. The obtained graphs were fit to the equivalent circuit parameters for further analysis in which the circuit parameters were initially estimated using graphical cues. Then, EIS300 software (Gamry Instruments) was used to fit the impedance values iteratively to the equivalent circuit models to refine the circuit parameter estimates until a 1 to 10% difference was obtained between the measured and calculated impedances.

The cyclic voltammetry (CV) curve reveals the ability of the interface to store the charge. A scan rate of 500mV/s was used to sweep the range between -0.6 and 0.7V vs. Ag|AgCl to remain within the water window. The water window is defined through the safe potential limits associated with the hydrogen and oxygen evolution in electrolysis of water. The area under the CV curve was calculated as an indication of the amount of stored/injectable charge in the water window without any gas evolution.

To be considered biocompatible, the charge needs to be transferred to the tissue either through reversible Faradic reactions or capacitive discharge where no new substance that may harm the tissue is produced. This situation limits the amount of voltage that can be created across the interface. Otherwise, electrical failure of the implant occurs either because of electrochemical damage to the electrode itself or because of the biological damage to the surrounding tissue caused by these electrochemical reaction products. Typically, a balanced charge biphasic waveform is used to prevent tissue damage at the electrode/tissue interface induced by irreversible electrochemical reactions. In this paradigm, the current is first passed in one direction, followed immediately by a second pulse which passes the current in the opposite direction using an equal amount of charge. It is difficult to extrapolate the results studied with slow potential sweep methods of cyclic voltammetry to the time scale of these pulsed potentials. On the other hand, studying the voltage transients through the

pulse excursions allows one, in principle, to address the electrically safe charge injection limitations to keep the operation in a range where no harmful reactant is released to the tissue.

To generate charge balanced, cathodic first, biphasic pulse currents, a programmable stimulator was used (Multichannel Systems STG2008). Pulses with 2ms pulse width, 2% duty cycle and charges between 0.2 and 20mC/cm^2 were sent to the electrodes in the saline solution. The resulting waveforms were recorded using an oscilloscope and then post-processed to fit to the equivalent circuit parameters.

4.1.4.4 Comparison of Gold Plating Techniques.

Gold is the most common finish-coating for flex-PCBs for passivating the underlying copper pads to improve soldering or wire bonding performance. However, in this study, gold plating was required for biocompatibility in covering the copper, which is poisonous for tissue [Bre 10]. During flex-PCB production, the deposition of gold is generally achieved either through electrochemical (electroplating) or chemical (electroless or immersion plating) means. The electroplating of gold requires extra traces on the substrate to raise the potential of the pads during the deposition. These traces are preferably removed during the release of the microelectrodes. Therefore, electroless or immersion plating methods lead to simpler layouts and production because the voltage application is not necessary during deposition.

On the other hand, one of the foremost concerns in electrically stimulating the neuro-muscular system is the injection of charges from electronically-conductive metal electrode into ionically conductive tissue. Therefore, a comparison is required of the electrochemical properties of these surfaces in order to evaluate charge injection efficiency. Electroplated gold was found to have more surface roughness and thus a larger electroactive surface area with respect to the immersion plated gold (Figure 38) probably due to the electrical field effects during the deposition. We also compared

these surfaces with the gold directly sputtered on the polyimide surface to compare the flex-PCB fabrication with conventional microfabrication methods. The directly sputtered gold had negligible roughness when compared to the flex-PCB based gold surfaces (Figure 38). We obtained the electrochemical impedance and cyclic voltammetry curves to characterize the effect of these surface topologies on the interfacial charge transfer characteristics for neural stimulation applications.

One important point that needs to be mentioned is the poorness of the step coverage for the immersion plating method. Although the sidewalls of the copper pads were successfully covered with gold through electroplating, the side surfaces partially remained uncoated in the case of immersion plating (see the arrow in Figure 38). To solve this issue, the metal traces were designed to be larger than the $100\times100\mu m^2$ insulation openings covering them (Figure 39). By using this method, the corners were kept under the insulation and partial deposition was avoided at the cost of larger traces. Moreover, copper traces can be patterned more precisely (down to 1µm resolution) with respect to the insulation openings (10-30µm resolution). Therefore, the variation in the pad size is more controllable when the insulation holes are wider than the metal traces, as in the case of electroplated gold (Figure 39). Another advantage for electroplating is that any desired thickness for the gold can be obtained, allowing for several microns of thickness for a safe coverage of the underlying copper. In contrast, immersion plating results in a difficult-to-control final thickness in the range of 100 to 200nm.

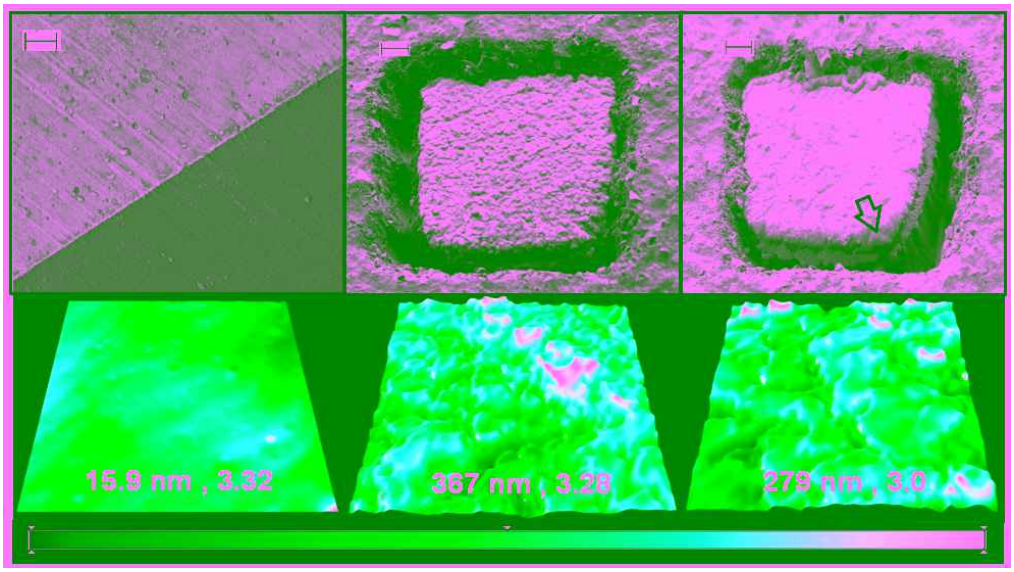

Figure 38: SEM and profilometer images of the sputtered (left), electroplated (middle) and immersion plated (right) gold surfaces; arrow indicating the partial plating at the corner of immersion plating. The scale bars on the SEM indicate 20µm and bottom edge of the each profilometer image is 30µm. The bottom color bar for the profilometer shows the range of 0 to 3µm for right and middle images and 0 to 300nm for left image. The roughness average (in nm) and surface kurtosis, respectively, are provided for each image.

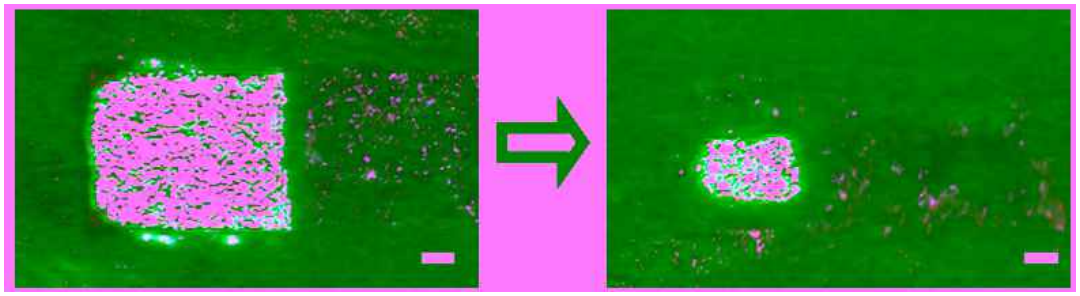

Figure 39: Immersion gold plated electrodes with insulation openings larger (left) and smaller (right) than the underlying traces to avoid partial coverage of the corners. Scale bar shows 25µm.

The analysis of the CV curves reveals that the plated gold, in both the immersion and electroplating processes, had a much higher number of stored charges available for injection than the sputtered gold (Figure 40). Furthermore, the electroplated gold had 1.3 times more charge with respect to the immersion plated gold. The EIS curves can be used to interpret these differences. For this purpose, the obtained EIS curves were satisfactorily fit to the equivalent circuit models in Figure

41 (Table 3). In the case of sputtered gold, the impedance was formed by the resistance of the electrolyte solution (R_s) and a series double layer capacitor (C_{dl}) formed at the relatively smooth gold-saline solution interface. The electroplating of gold over copper resulted in a similar equivalent circuit, but with a constant phase element (CPE) in parallel to the double layer capacitance. This CPE represents the non-ideality of the surface caused by increased roughness due to the underlying copper and the effects of the electrical fields during electroplating. In the case of immersion plating, covering the corners with an insulating layer introduced a capacitance (C_{ins}) in series to the CPE, despite the fact that it solved the step coverage related problems. We also needed to add a parallel charge transfer resistance (R_{ct}) to C_{ins} to have a satisfactory model fit. This ohmic representation, modeled as resistance, can be interpreted as the leakage from the copper to the electrolyte solution as a result of the poorly coated parts of the copper surface with a relatively thinner gold layer. The similarities of recorded R_s values for all the surfaces validate the models. The higher roughness of electroplated gold causes a higher capacitance, and a smoother sputtered gold surface results in lower capacitance. The CPE has an impedance defined as $(Yo(jw)^n)^{-1}$ where lowness of Yo means more non-ideality. As n gets closer to 1, the non-ideality begins to demonstrate a more capacitive behavior. The increased roughness of the electroplated gold also matches the lower Yo value, where the non-ideality is more capacitive with respect to the more resistive leaky immersion plated gold surface.

The above analysis shows that the maximum amount of charge that can be capacitively discharged from the gold coated copper pads of flex-PCB probes is 3 to 4 mC/cm^2 in the water window. To obtain a higher amount of charge for neural stimulation, one needs to exceed the water window, which causes oxygen reduction, where the free radical products of oxygen are known to be harmful to the cellular

function in the long term [Mor 94]. Higher voltages also potentially expose poisonous copper to the tissue by dissolving/delaminating the gold coating. Therefore, direct use of flex-PCB as a stable and long-term stimulation electrode is not feasible for applications requiring more than 3 to 4 mC/cm^2 to initiate a biomechanical response.

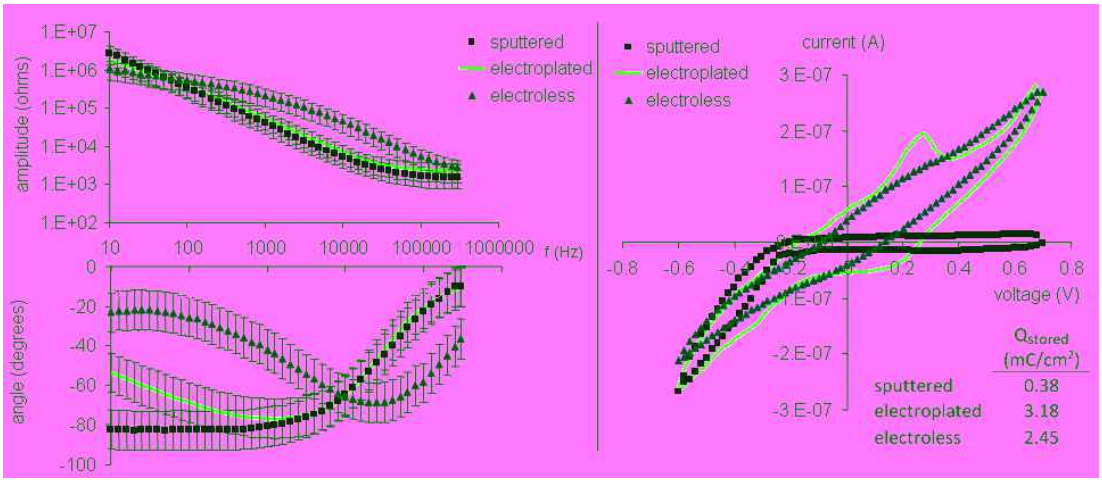

Figure 40: Averaged amplitude and phase plots obtained through EIS (left) and averaged CV plots (right) for 100×100µm^2 gold pads deposited through sputtering, electroplating and immersion plating. Inner table shows the area under each CV curve indicating the stored/injectable charge for each material.

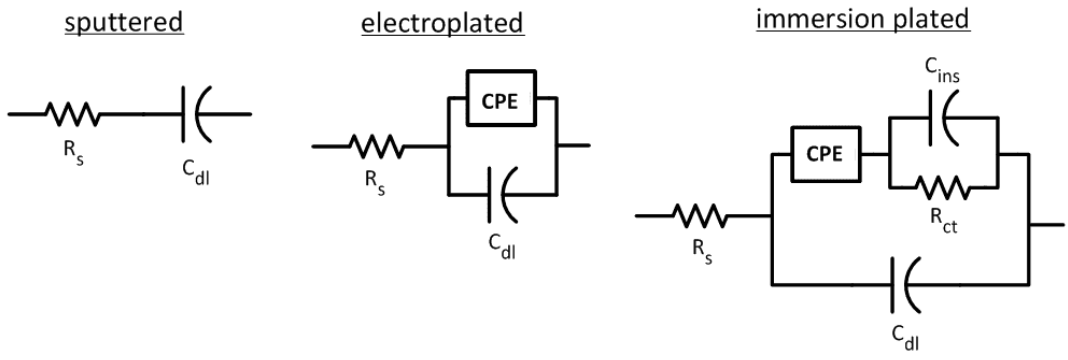

Figure 41: Equivalent circuit models for the electrolyte-metal interface on gold pads deposited through sputtering, electroplating and immersion plating

Table 3: The Averaged Values of the Model Parameters Extracted through Curve Fitting

material	R_s	C_{dl}	R_{ct}	C_{ins}	Y_o	a_1
sputtered	4196	2.47E-11	-	-	-	-
electroplated	4246	2.26E-09	-	-	4.89E-08	0.54
electroless plated	5115	7.90E-10	1.41E+04	1.82E-08	9.46E-07	0.26

4.1.4.5 Improvement with Iridium Oxide and PEDOT Coating.

To enhance the electrochemical properties of the flex-PCB electrodes, we electrodeposited iridium oxide and electropolymerized Poly(3,4-ethylenedioxythiophene) poly(styrene-sulfonate) (PEDOT-PSS) over the gold coated electrodes to facilitate extra charge transfer across the interface. For the deposition of iridium oxide, we followed a recipe similar to [Yam 89]. Seventy-five milligrams of iridium(IV) chloride hydrate was dissolved in 50ml of deionized water by stirring for 30 minutes at room temperature, which formed a black colored solution. Then, 0.5ml of 30% hydrogen peroxide solution were added to the solution and stirred for 10 minutes, which turned the color of the solution to yellow. Adding 250mg of oxalic acid dihydrate turned the color of the solution blue, and that was stirred for another 10 minutes. Small amounts of anhydrous potassium carbonate were slowly added to the solution, until a pH of 10.9 was obtained. The solution was kept at room temperature for 2 days to reach equilibrium before the deposition.

PEDOT-PSS monomer solution was prepared by stirring 35mg of 3,4-ethylenedioxythiophene (EDOT) with 250mg poly(styrenesulfonic acid sodium salt) in 25ml of deionized water for 2 hours until all of the globules of EDOT that had formed were dissolved [Cui 07]. All the chemicals for both solutions were purchased from Sigma Aldrich, Inc.

In both cases, flex-PCB electrodes were immersed in the solution to act as anodic working electrodes. The cathodic counter electrode was a $2.5\times2.5cm^2$ platinum sheet. Galvonastatic charges of 40 and $100\mu A/mm^2$ were applied for 60 and 120 seconds for iridium oxide and PEDOT-PSS respectively. The electrodes were rinsed with DI water and nitrogen-dried.

Because the flex-PCB electrodes were manufactured using a commercial process and received as finished products, we were only able to pursue the use of wet deposition techniques that require no masks to coat the surface. For the coating material, we studied iridium oxide and PEDOT which are currently considered as the best performing conductive thin films to improve the charge transport efficiency from metal stimulating electrodes into the aqueous media [Cui 07]. Coating the electrodes with either material required a gold coated surface, rather than bare copper. The immersion gold was problematic during the coating of either material when there were poorly coated regions; therefore, electroplated gold was used for the starting surface.

The optical and SEM images of the bare and coated surfaces can be found in Figure 42. The PEDOT-PSS facilitated a significant decrease in the impedance curve, much greater than the decrease achieved with iridium oxide (Figure 43). The decrease in the impedance indicates a lower charge transfer resistance and thus a more efficient electrical signal transduction from metal to the electrolyte. This result is also matched with a much higher number of injectable charges for PEDOT-PSS with respect to the iridium oxide as characterized by the cyclic voltammetry (Figure 43).

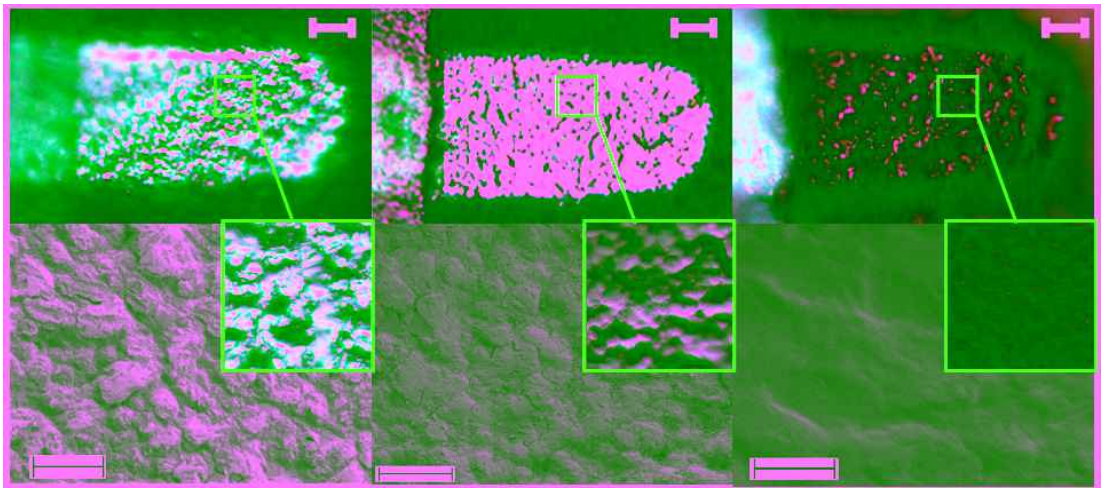

Figure 42: Electrodeposited iridium oxide (middle column) and electropolymerized PEDOT-PSS (right column) over the electroplated gold pad (left column) at three different scales. The top row shows the optical image of the pad (scale-bar:25µm) with a magnified view in the middle squares (each side 25µm). The higher resolution image was obtained through SEM as presented at the bottom (scale-bar: 2µm).

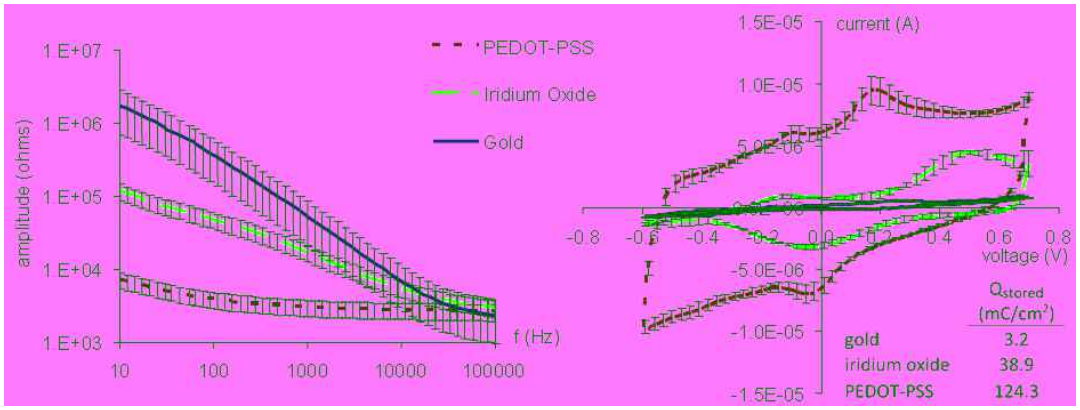

Figure 43: Average improvements in the impedance and charge injection capacity with the deposition of iridium oxide and PEDOT-PSS over electroplated gold as characterized through EIS (left) and CV (right). Inner table shows the area under each CV curve indicating the stored/injectable charge for each material.

The central feature of the improvement with PEDOT-PSS deposition was the introduction of ionic dopants with extra available mobile charge carriers, causing an enhanced charge transport into the electrolyte solution [Cui 07]. In the case of the iridium oxide coating, the electrochemical reaction involved a reversible conversion between redox states of Ir^{+3} and Ir^{+4} where the produced or dissipated charge was

balanced by the counterions in the electrolyte through a Faradic charge transfer mechanism [Mey 01]. The charge applied to the electronically conductive electrode developed a voltage at the interface and this forced iridium oxide to transfer to a higher valance by ejecting protons into the ionically conductive solution, which was reversed when the charge was removed from the surface towards the electrode. Also, for either material, additional surface irregularities are formed, increasing the roughness or porosity to alter the impedance properties [Cui 07, Mey 01].

Although the electrochemical properties were improved, exceeding the water window still causes irreversible reactions, where gas formation and soluble dissolution products occur. These products diffuse away to the tissue, promoting tissue damage, and cannot be converted back to the corresponding reactants. The voltage excursion studies of the sent biphasic pulses revealed that the amount of charge that can be safely injected to the tissue was in the order of 10mC/cm^2 for PEDOT-PSS, whereas this charge was approximately 1mC/cm^2 for iridium oxide and around 0.1mC/cm^2 for the gold surface (Figure 44). More than these values, the charges caused a polarization voltage (Vp) higher than -0.6V, pushing the operation to unsafe regions outside the water window. The polarization voltage was calculated by subtracting the voltage drop due to the solution resistance ($I_d \times R_s$ where I_d is induced drive current and Rs is the solution resistance) from the overall drive voltage (V_d) recorded at the electrode (Figure 45). PEDOT-PSS also caused a smaller residual voltage, which was an indication of the irreversible reactions occurring due to the non-ideality of the system. Ideally, the residual voltage should return to 0V at the end of the second pulse of the biphasic sequence. The residual, drive and polarization voltages (Figure 45) that were recorded for different injected charges are presented in Figure 46.

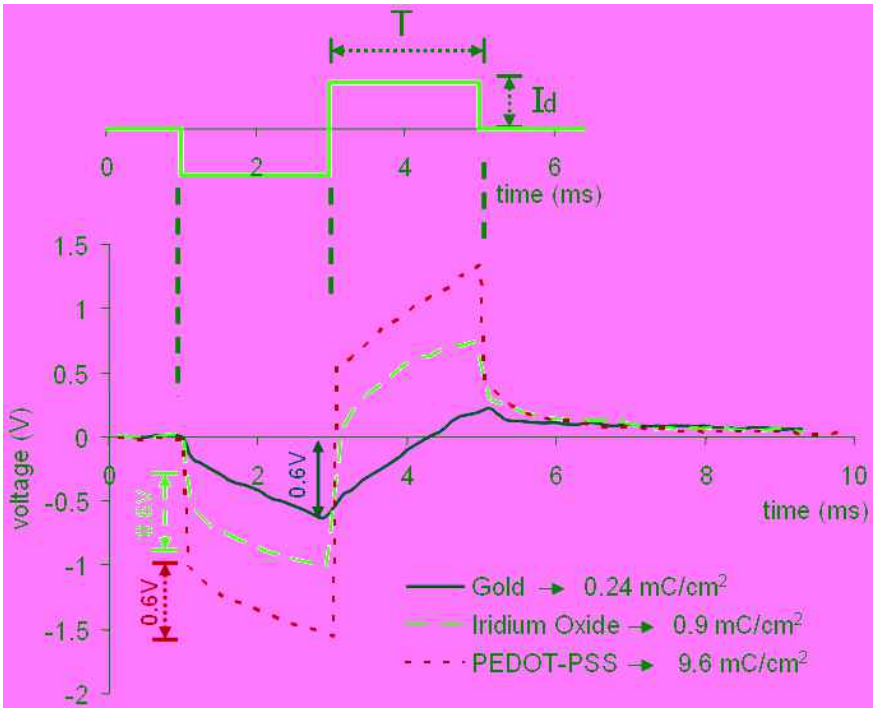

Figure 44: Voltage excursions obtained by passing biphasic current pulses (top) to the electode-electrolyte junction. The bottom graph demonstrates the drive voltage with the obtained -0.6V polarization voltage across each material. The required currents to obtain this voltage are given next to each material.

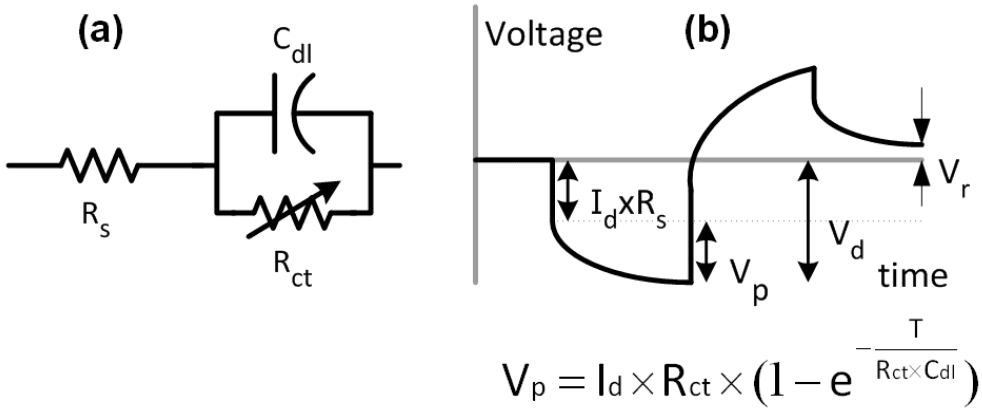

Figure 45: (a) Equivalent circuit model used for fitting the voltage excursions (b) definitions of the polarization, drive and residual voltage on the voltage transient curve

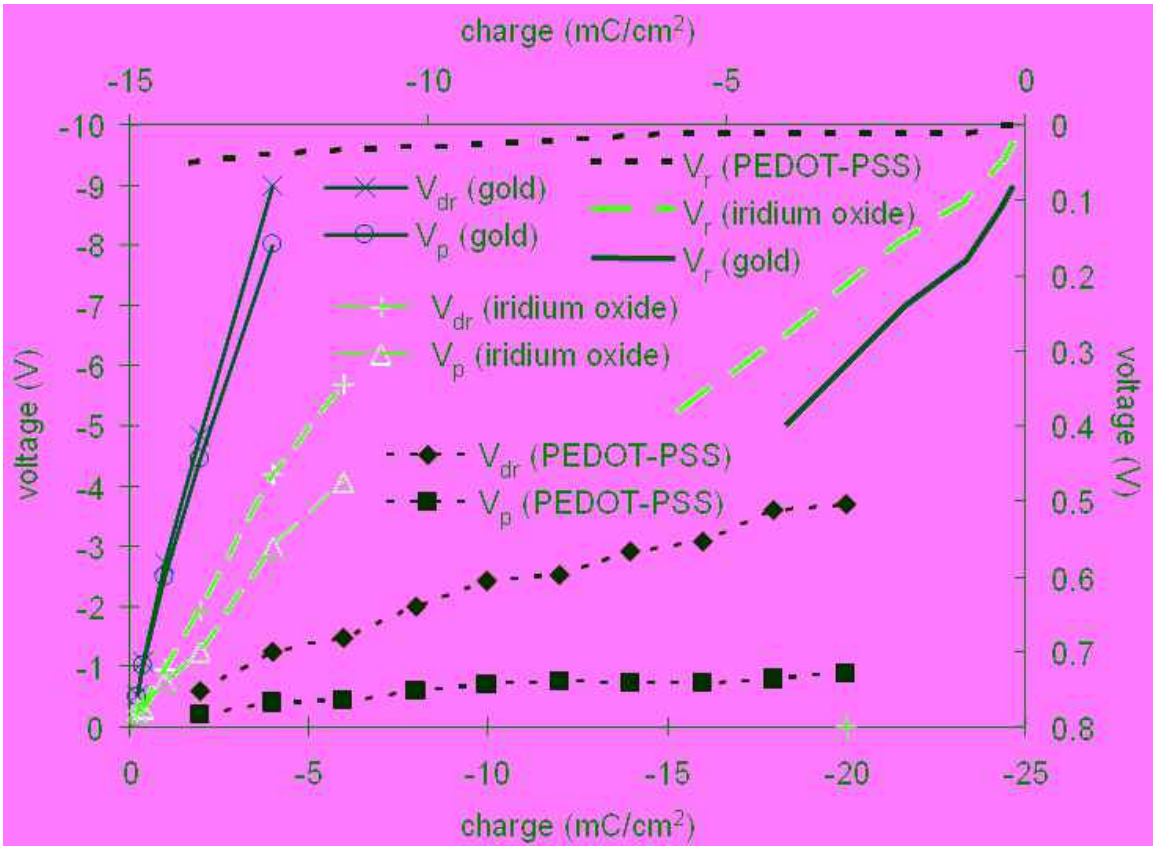

Figure 46: Polarization, drive and residual voltages obtained for different biphasic current amplitudes applied to gold, iridium oxide and PEDOT-PSS surfaces.

The voltage transients for these three surfaces can be thoroughly characterized and compared by fitting them into the equivalent circuit models (Figure 44), thus allowing formulation of general insights into the behavior of electrodes under pulsed conditions (Table 4). For PEDOT-PSS coating, the introduced ionic dopants with extra mobile charge carriers, in addition to the improved surface topology obtained during electropolymerization, provided more charge storage (higher C_{dl}) and an easier and more efficient charge transport (lower R_{ct}) with respect to the additional reversible Faradic reactions introduced with the deposition of iridium oxide. For the given electrode size, the lower impedance obtained with the PEDOT-PSS at the metal electrolyte enables a lower stimulus voltage that will induce sufficient current to initiate a biomechanical response during neuromuscular stimulation applications. The

reduced stimulus voltage in turn decreases the size, supply voltage and power consumption of the electronic circuitry providing the stimulus pulses.

Table 4: The Averaged Values of the Model Parameters Extracted from Voltage Excursion Curves

material	Q_{inj} (mC/cm^2)	R_s ($k\Omega$)	R_{ct} ($k\Omega$)	C_{dl} (nF)
gold	0.2	3.8±2.3	-	40.4±0.9
	2	4.2±2.1	-	43.9±0.6
	4	5.1±1.7	-	49.7±0.5
iridium oxide	0.2	3.2±2.6	32.2±5.2	96.9±22.2
	2	5.2±2.3	28.9±4.1	99.6±17.1
	4	6.1±2.0	26.1±3.8	100.4±14.5
PEDOT-PSS	2	4.1±2.7	2.7±1.6	705.6±253
	4	4.7±2.1	2.5±1.2	773.9±282
	10	5.2±1.8	2.0±1.1	892.1±232

In addition to this important advantage, the aqueous monomer solution for electropolymerization of PEDOT-PSS is much easier to prepare, can be stored longer and requires less expensive chemicals with respect to the electrodeposition solution of iridium oxide. Iridium oxide also required a narrow range of current to be applied during the electrodeposition, and was less tolerant to the deviations in these values. The deviations from the required value caused poor adherence to the underlying substrate where delamination was observed during later voltage or current pulsing, a phenomenon reported previously in the literature [Mey 01].

4.1.4.6 Characterization of Water Permeability.

The long term stability of the electrodes against water permeability was evaluated under both charge injected and non-injected conditions. The electrodes were dipped into a saline solution for 40 days while the impedance at 1kHz and injectable

charge amount (through current pulsed voltage excursion analysis) were recorded on a daily basis. The electrodes were monitored in the absence and presence of charge transfer between the metal pad and the electrolyte solution. The charge was applied as cathodic first, charge balanced biphasic current pulses (150uC/cm^2 for gold and 2mC/cm^2 and 10mC/cm^2 for PEDOT-PSS) with 2ms of pulse width and 2% duty cycle.

While PEDOT-PSS coating results in a much improved electrochemical performance, the lifetime of this inherently conductive polymer for neural recording and stimulation applications is still under investigation. Absorption of water by polyimide is also known to cause delamination between metal and polyimide as a result of the associated mechanical stresses [Xu 06]. The potential of PEDOT-PSS coated flex-PCB electrodes for neuromuscular stimulation was assessed with a 40-day saline solution dip test. When immersed in the saline solution, the average 1kHz impedance of the electrodeposited gold pads decreased from 21kΩ to 5kΩ in 5 days and were stabilized afterwards. The average injected charge to cause a polarization voltage of -0.6V was 150uC/cm^2 on the first day and increased to 510uC/cm^2 during the first 15 days and stabilized afterwards (Figure 47). The gold pads continuously pulsed with 150uC/cm^2 biphasic pulses and followed a similar trend with nonpulsed pads but with a higher standard deviation. We also had some of the pads completely covered with polyimide as the insulation layer, thus without any insulation openings. The impedance of these pads was "open" during the course of the measurement and did not change at all. Therefore, the penetration of water through the polyimide insulation was not an issue for water dipped flex-PCB electrodes during the duration of the test. This may indicate that the improvement in the impedance and injectable charge by time was caused by the penetration of water into the exposed metal pads at nano- and micro-scales which potentially facilitated the charge transport mechanism.

The average impedance of the nonpulsed PEDOT-PSS coated electrodes also followed a decreasing trend (from 1.6 to 1.1 kΩ) which was stabilized around the 10th day. In the meantime, the injectable charge rose to 14.2 from 10 mC/cm^2 in 4 day period (Figure 48). The continuously pulsed electrodes (with pulse amplitude of 2 mC/cm^2) followed a similar trend. We also observed this trend with the electrodes pulsed with 10 mC/cm^2 pulses, however just until the 17th day, then, increasing the number of failed pads with each additional day. By the 40th day, all the pads (both pulsed and non-pulsed) had delaminated spots on the PEDOT-PSS coating where the average impedance was around 80 and 85kΩ and the average injectable charge was 0.5 and 0.3 mC/cm^2 for nonpulsed and pulsed pads, respectively (Figure 48).

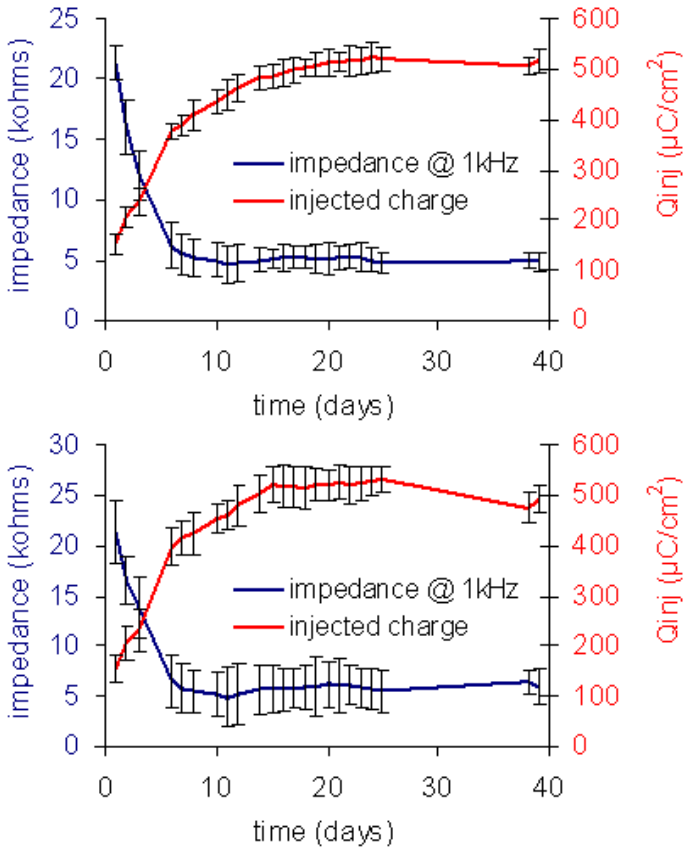

Figure 47: Average impedance amplitude at 1 kHz and injectable amount of charge recorded over 40 days in saline solution. The bottom graph shows voltage pulsed gold-electrolyte interface and nonpulsed interface presented at the top.

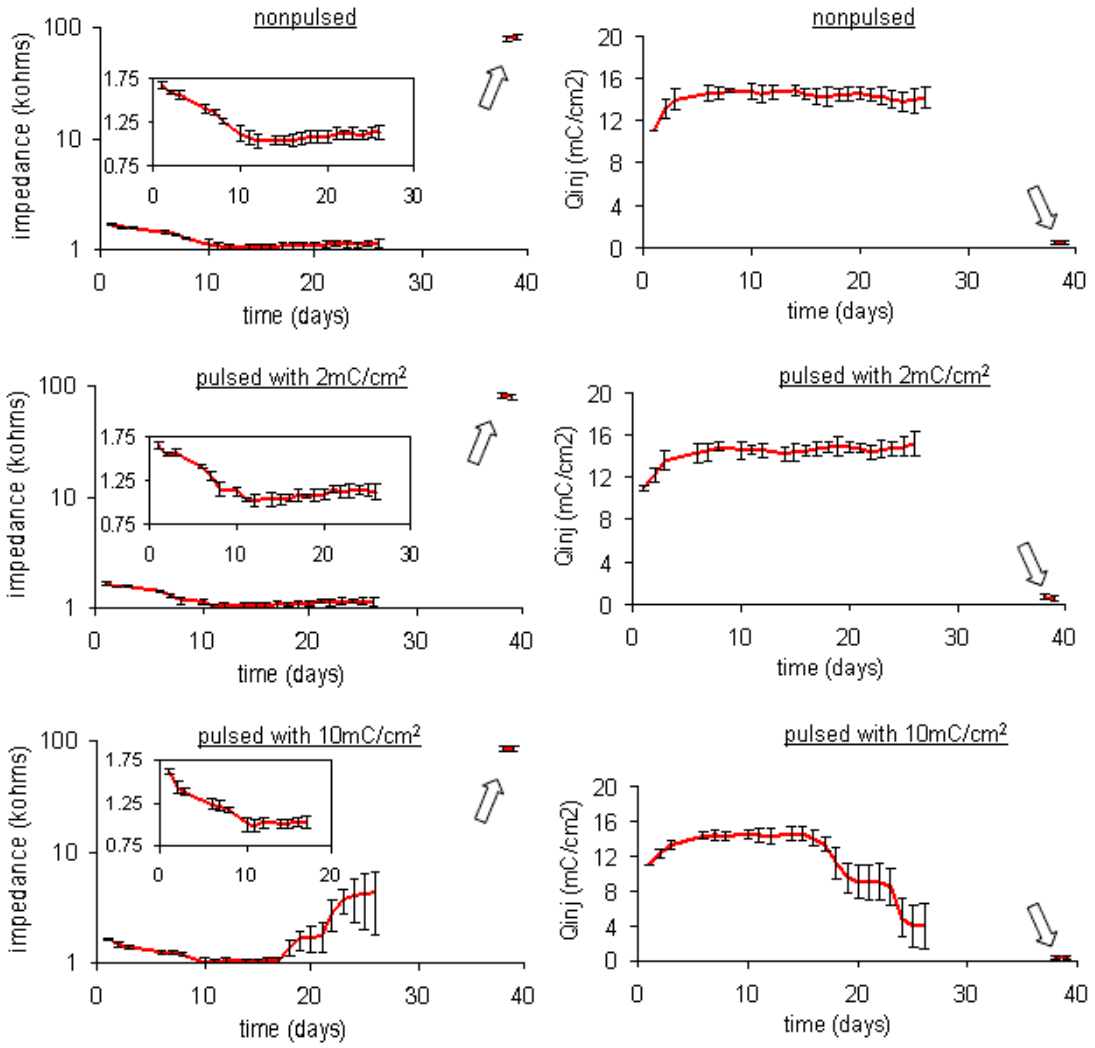

Figure 48: Average impedance amplitude at 1 kHz (left) and injectable amount of charge (right) for high (bottom) and low (middle) current density pulsed and nonpulsed (top) PEDOT-PSS surfaces in saline solution recorded over 40 days. The inner graphs are the magnified and linear version of the impedance data for the first 26 and 17 days for nonpulsed and pulsed interfaces respectively. Arrows emphasize the data on the last two days.

During the 40-day tests, we observed that the change in the electrochemical properties of PEDOT-PSS was much lower compared to change in the gold electrodes; therefore, PEDOT PSS provided a more stable interface during the first 4-weeks after having been dipped in the saline solution. The pulsing of the gold did not change the average electrochemical performance of the stimulation electrodes but caused a higher

variation due to the possible surface degradation with continuous charge transfer. In the case of PEDOT-PSS, a similar result was observed during the first 17 days of the operation. Then, the high density current pulsing caused an earlier delamination of the PEDOT-PSS. While the nonpulsed and low density current pulsed PEDOT-PSS electrodes survived the first 4 weeks, one needs to be cautious about the applications that require continuous pulsing of the pads with higher current densities.

The four-week lifetime of these electrodes in water allows us to hypothesize a stable operation during the aforementioned neuromuscular stimulation applications in insects, for many relevant insects', such as moths', lifespan is usually less than a month. It also should be mentioned here that under in-vivo conditions, having tissue mechanically adhere to the probe surface may eliminate/reduce the delamination further increasing the stable operation duration.

This study presents a good starting point for further extending the deposition of other emerging conductors such as carbon nanotubes, graphene or other inherently conductive polymers. These can improve the electrochemical properties of the flex-PCB electrodes for neural stimulation applications.

4.1.5 Selection of the Substrate Materials

As the substrate material, polyimide and silicon were used until the present for the scope of the study. Because of the fragility of the probes, silicon is only used for experimental setups in which the insect body and thorax was mechanically fixed. Polymer based flexible materials were considered for general use to provide strain relief against the potential motion between the implanted material and the tissue. As the flexible biocompatible material [Ric 93], polyimide was selected because it is the most common material used in commercial flexible circuit manufacturing. One concern about this fabrication process is that the minimum producible feature size is

75µm with a line-pitch of 75µm. This feature limits the capability of fabricating probes with multiple pads (in the order of 10 to 20) providing denser probing for more advanced studies. In this case, standard cleanroom processing can be utilized. During the cleanroom fabrication, Parylene™ can be considered as an alternative to polyimide as the substrate material. A typical process flow for parylene based probes can be found in Figure 49, allowing a higher number of channels (by means of thinner conductive lines) and improved flexibility (thinner substrate). Parylene has similar mechanical (Young's modulus for parylene 3.2GPa, polyimide 2.5GPa) and biocompatibility properties to polyimide [Sch 88].

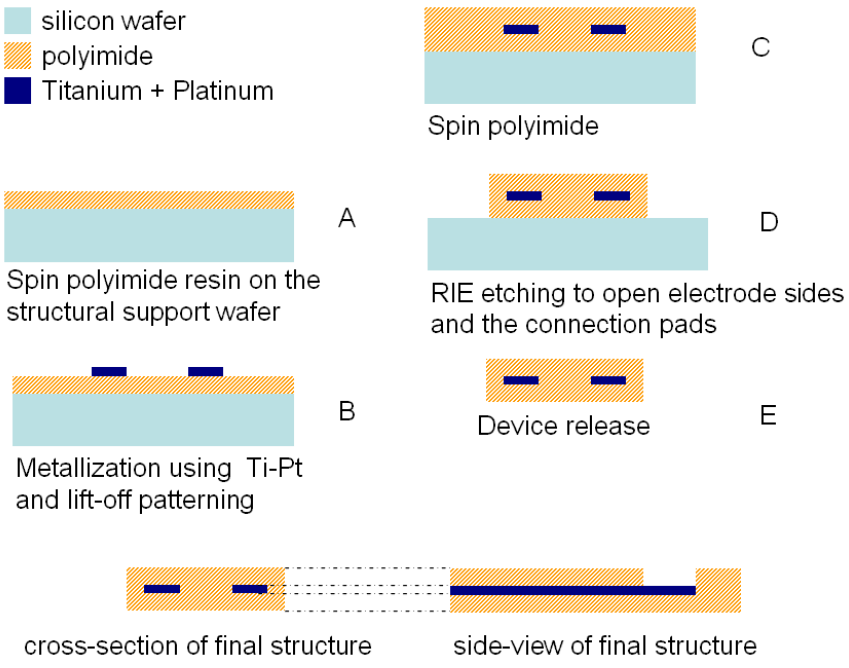

Figure 49: Cross-section and the layers of the proposed parylene-based microprobe

An issue of using flexible polymers as a substrate is their water absorption in the long run. However, as explained in the previous section, because insects have an

average life time of 3–4 weeks, water absorption is not an issue for biobotic insect applications.

4.1.6 Actuation of the Third Axillary Muscles

As a direct flight muscle, the third axillary muscle plays an important role in turning flight, as described in Chapter 3. Although it is possible to induce rotating motor output by stimulating only indirect flight muscles dl and dv, actuating direct flight muscles may create a more pronounced affect. The third axillary muscles will not be studied in the scope of this thesis; however, two alternatives will be presented for reaching the third axillary muscles through pupal EMIT based implantations. The third axillary muscles are located under the wings, and these muscles are difficult to reach directly because the wings are wrapped around the body just above the muscles (Figure 18, 21) during metamorphic growth. One method is to build extended arms to the *dl* and *dv* targeting probes and to wait for the insect to emerge without inserting the 3rd axillary probes (Figure 50). After emergence, the insect can be anesthetized, and probes can be inserted and fixed using biocompatible glues.

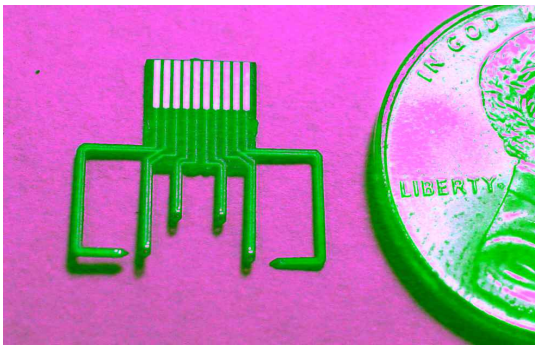

Figure 50: Flexible polyimide probe with extended arms to be inserted under the wings after emergence

Another potential method is to build probes that will reach these muscles from inside, and this allows complete pupal stage insertion. A layout for such a probe can be seen in Figure 51. This probe requires a tilting action after the insertion, which may damage some of the preformed tissue. Therefore, the pupal implantations must be done in the early stages of metamorphosis.

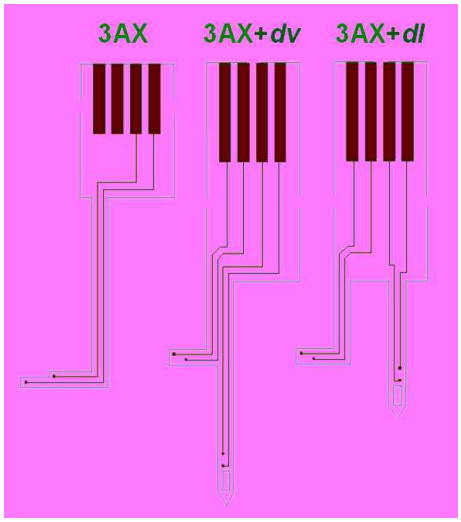

Figure 51: Probes designed to target third axillary muscle alone (left), with *dv* muscle (middle) and with *dl* muscle (right). Blue lines show the conductor metal and the brown line is the outline of the polyimide substrate. See Figure 21 for the location of the third axillary muscle.

4.1.7 Optimization of Probe Geometry and Metal Pad Allocation

The motor response can be improved enormously by bioelectrically mapping the flight muscles of the *Manduca sexta* because stimulation performance depends on the distance to the closest neuron intervening the flight muscles. The actuation of the nerves requires smaller voltages with respect to muscle fibers, for multiple muscle fibers can contract with the actuation of a single nerve. Nonetheless, targeting the nerves directly is difficult as it requires a more detailed surgical operation to localize nerves during EMIT based surgical insertions. On the other hand, by increasing the

inter-pad distances, the probability of covering the regions where the nerves are located can be increased. Moreover, the increased inter-pad distances also increase the direct recruitment of a higher number of muscle fibers. In both cases, the location of pads in the flight muscle is critical in order to create the desired motor output. This electrical mapping requires the testing of different actuation pad locations and inter-pad distances. The optimization of these geometrical parameters is required for an ideal simulation probe but is beyond the scope of this dissertation. Such optimization can be achieved by micromachining microprobes with multiple numbers of actuation pads (>20) and actuating the different combinations of the pads while observing the motor output.

4.1.8 Thermal Electrodes (Thermodes)

Microfabricated polyimide based flexible "thermal" microprobes were also developed for the artificial endogenous heating of the insect thorax to decrease the preflight warm up duration. Each probe was designed to be used with Flexible-Flat-Cable (FFC) connectors. The connectors can be joined with flexible wires for tethered experiments, or they can be joined to a battery-powered tiny printed circuit board for untethered experimental setups (Figure 52). Upilex®-S type polyimide film (25µm thick) with electrodeposited copper (125µm-wide and 35µm-thick) was wet-etched to define the conductive traces. Commercially available 0201 size surface mount thermodes (50-100Ω) and surface mount thermistors (100Ω) were solder-assembled on the probes for heating and temperature recording in different geometries (Figure 53). The height, width and length of the surface mount components were 230, 300 and 600µm. The probes were coated with 10µm-thick Parylene-C™ using a PDS-2010 deposition system (Speciality Coating Systems, Inc.) for bio-compatibility and electrical isolation from the tissue.

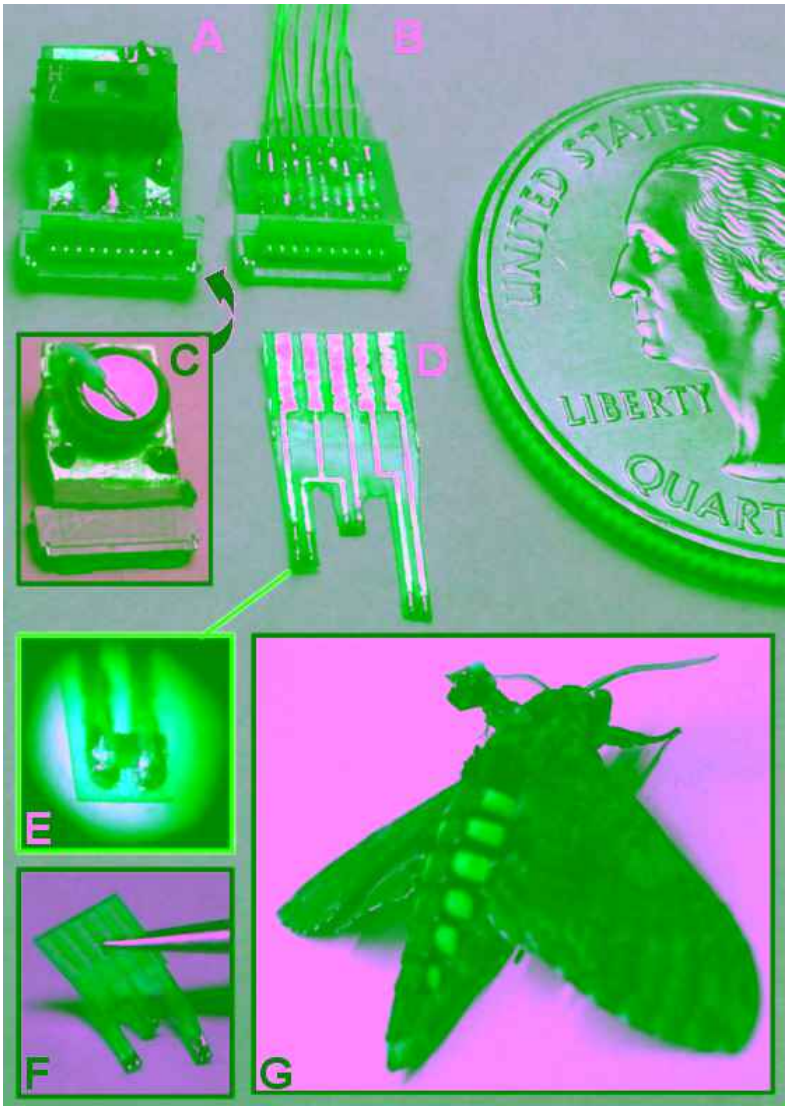

Figure 52: Polyimide flexible thermal probe (D) with attached thermistors (E) for recording via flexible-wires connected through an FFC connector (B). The wires also function as a tether. Flexibility of the probe is demonstrated in (F). The tiny PCB (A) with a slide switch, LED indicator, FFC connector and watch battery (at the backside of the board as shown in C) is attached to the insect easily without anesthesia (G) for untethered heating. The overall system (G) weighs 350mg where payload capacity is more than a gram. The scale-bar (G) represents 5mm.

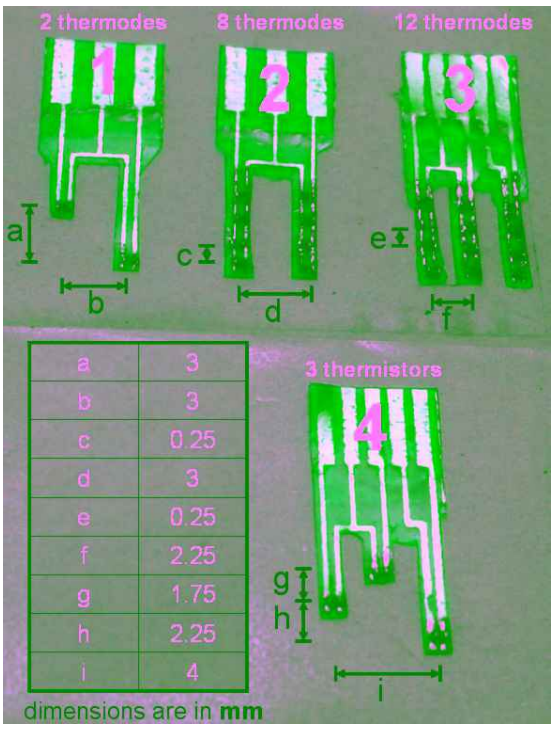

Figure 53: Thermal probes holding different number of thermodes (probe numbers 1, 2 and 3) at various geometries for heating the tissue and the probe (numbered as 4) with three thermistors to record the temperature at three different locations. The reported temperatures were calculated by averaging the temperatures recorded by these three thermistors.

4.2 Tethered Experimental Platforms

The experimental protocols presented in Chapter 5 consist of tethered insects in which the insect neuromuscular system is actuated through the flexible wires, as well as non-tethered setups in which there are no attached wires, and the free-flight of the insect can be realized. The microprobes described in the previous section can work with both tethered and untether setups (Figure 34). For tethered muscle excitation experiments, a flexible cable can be connected to the external probe body in which the cable can used both for signal delivery and mechanical suspension (Figure 70). Tethered wires give experimental design flexibility and can be replaced with radio frequency controlled microsystems for specific applications.

The polarity of the applied pulse through the tethered wires is an important point affecting the electrical stimulation efficiency of the neuromuscular system. During the stimulation process, the charge collected during an applied monophasic pulse in the capacitive region leaks away very slowly. Therefore, if the inter-pulse duration is not wide enough, charges build up and push the operating curve outside the capacitive region (Figure 32). Even for non-corroding noble metals, this region is not preferred, for it causes uncontrolled charge injection. To solve this problem, balanced biphasic pulses are generally used where an opposite polarity pulse is sent after an applied monophasic pulse (Figure 54). For a balanced charge stimulation, A1×D1 must be equal to A2×D2. Different responses were reported in the literature for mono and biphasic pulses [Fie 03]. The pulse parameters (amplitude, duty cycle and frequency) can be changed to alter motor output. In particular, response to different frequencies is important, for the motor output can be tailored with a spectrum of responses from single twitches to complete tetanus [Guy 96].

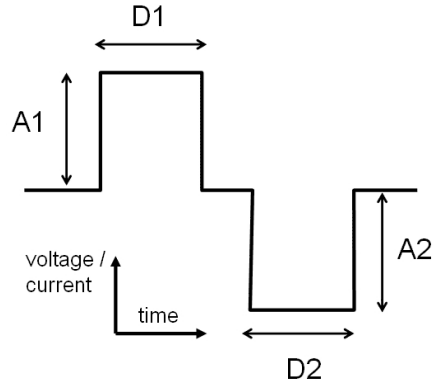

Figure 54: Biphasic pulse waveform where A denotes the amplitude and D denotes the duration of the stimulation

4.3 Backpacks for Tetherless Locomotion Control

The wireless insect neuro-muscular stimulator platform consists of two layers that are connected to the microprobes on the insect: the control electronics and the power unit (Figure 55). The control electronics part consists of a microcontroller with

or without a radio-receiver connection. In the following sections, the details of these subsystems will be presented.

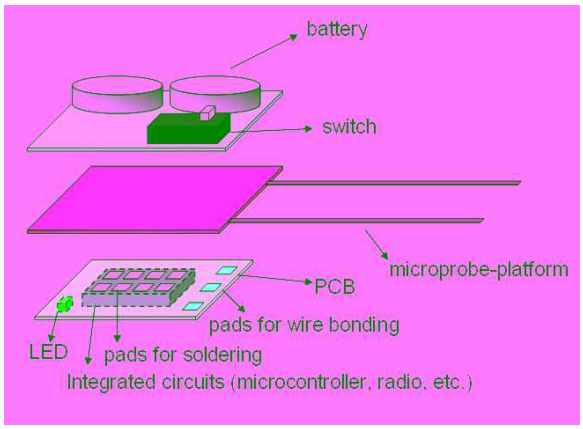

Figure 55: Layers of the wireless micro-stimulation platform: power (top), probe (middle) and control electronics (bottom)

4.3.1 Microcontroller-based Operation

For some applications in highly controlled environments, a predetermined pulse streams may be sent to the probes for controlled navigation. In this case, a preprogrammed microcontroller may be used to store the pulse streams, and send them sequentially. In this case, the control electronics layer of the microsystem consists of only a microcontroller. Such a system can be seen on the insect in Figure 56 and 57. In this system, the control layer is an 8×8 mm^2 PCB holding the microcontroller (Atmel Tiny13V) and an LED. The microcontroller was electrically connected to the PCB via flip-chip bonding. Wire-bonding was used to connect the PCB to the probe layer. The power layer is comprised of two coin batteries and a slide-switch (weight: 30mg) positioned on a printed circuit board (PCB). Coin batteries (SR516SW, Maxell) can supply enough current to power the microcontroller (240μA active, 0.1μA stand-by). Each battery has an energy capacity of 8mAh and weighs 120mg. Conductive adhesive was used to attach the batteries to the platform, and the micro probe is

sandwiched between these two layers. The overall system has dimensions of 8×7 mm^2 and a total weight of 500 milligrams including the batteries (Table 5).

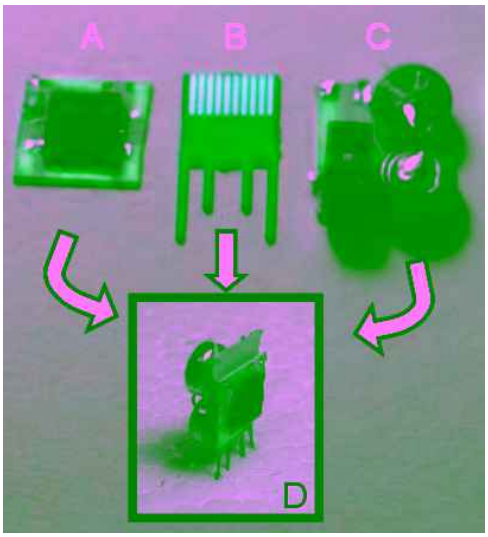

Figure 56: The microsystem including microprocessor (A), flexible probe (B), and battery unit for power (C). The assembled system is given in (D).

Table 5: Weights and Sizes of the Microcontroller Based Stimulator Parts

component	power/energy	size (mm)	weight (mg)
attiny13v	0.5mW (active)	4 x 4	75
battery	8mAh	5.8 (diameter)	120
switch	-	6 x 1.5	30
LED	1.8mW	1.6 x 0.8	10
PCB	-	8 x 8	75

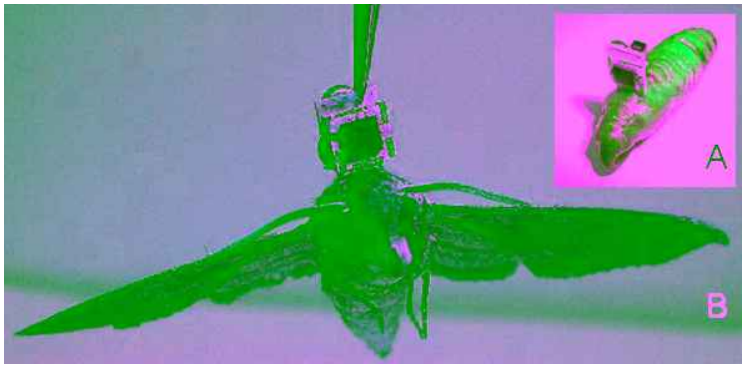

Figure 57: Pupal stage insertion (A) and successful emergence (B). The microsystem platform on (ii) is held with tweezers to show wing opening of the moth.

4.3.2. Super-regenerative Based Radio

In most applications, a radio link will be required to transmit dynamically changing neuromuscular excitation pulse streams to the insect. In this case, the control electronics layer should also include a radio in addition to the microcontroller. In this case, super-regenerative based architecture would be very advantageous and require fewer electrical components, thereby weighing less and consuming minimal power as a result of the self-oscillatory and self-quenching advantages of the "super-regeneration" principle [Sha 99]. The super-regenerative detector located in the center of this radio architecture (Figure 58) acts like an amplifier with automatic gain control to provide self-mixing RF detection, eliminating extra components for local oscillator, frequency mixer and tuned amplifier in traditional superheterodyne topologies [Sha 99]. A typical circuit diagram is presented in Figure 59.

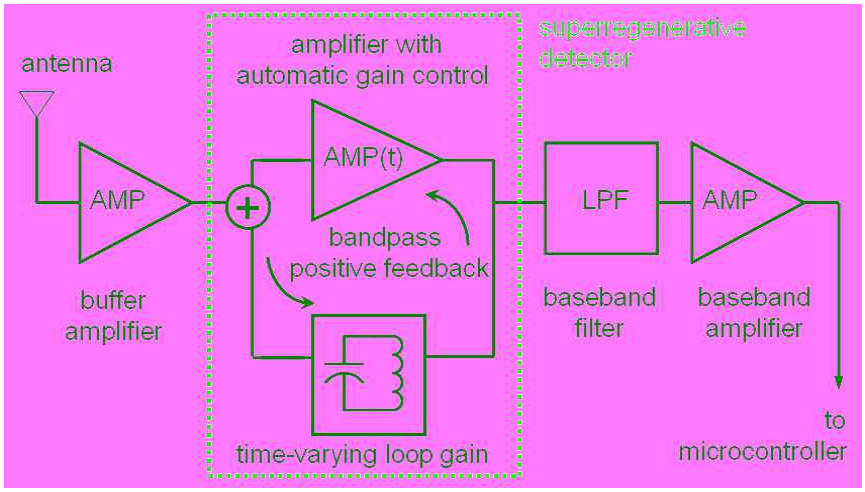

Figure 58: Super-regenerative receiver architecture. Super-regenerative detector realizes self-oscillation and -quenching as the result of automatic gain controlled bandpass positive feedback.

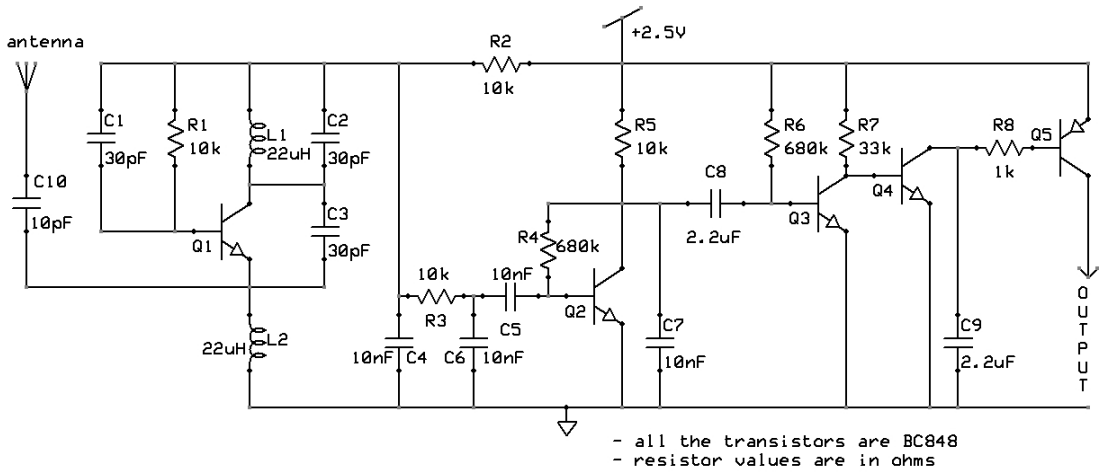

Figure 59: A typical circuit diagram with component values for a super-regenerative based receiver

Commercially available (Futaba, Inc.) two-joystick 3 channels 72MHz AM transmitters (Figure 60) were used for the radio to transmit PPM (Pulse-Position-Modulation) pulses remotely to the insect neuromuscular system. These transmitters are widely used in remote controlled (RC) systems to control the flight of micro-air-vehicles, model airplanes, helicopters, etc.

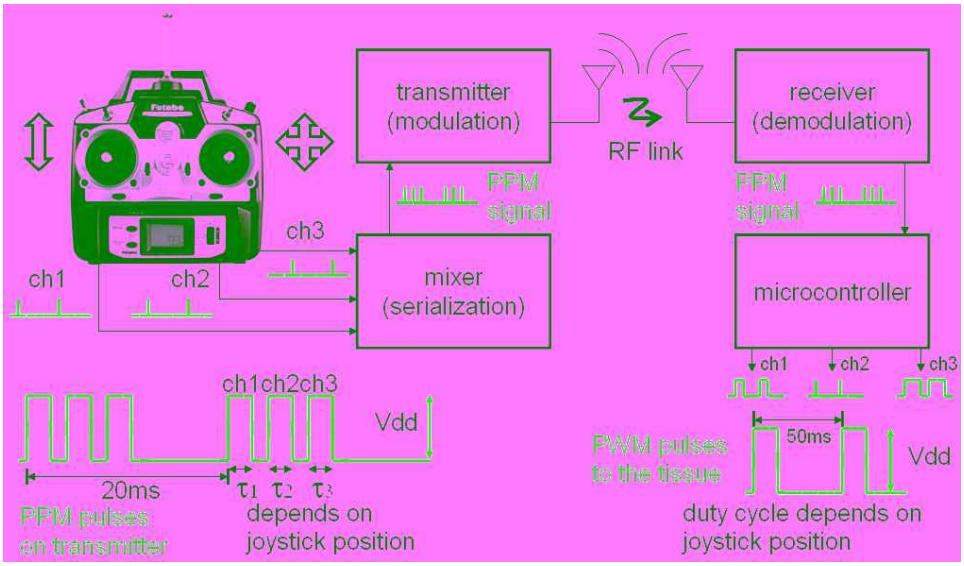

Figure 60: Pulse shaping at transmitter and receiver sides of the radio frequency remote controlling system (Vdd=3.5 V)

As the receiver part of the radio, a super-regenerative based architecture was custom built on a FR-4 PCB (Figure 61), to receive and demodulate the transmitted PPM stream by the transmitter. A microcontroller (PIC12F615) was also connected to the receiver output to separate the PPM stream into different channels. The electronics board that holds the receiver and microcontroller weighs only 70mg and consumes less than 1 mW of power (~ 750 µWatts static, ~1 mW dynamic). The FFC connectors are added to the board to be joined to the stimulation probes as well as the power source. FFC connectors allows the batteries to be detached and attached easily to turn the system on and off. A Li-Po battery (3.6volts, 8.5mAh) was used as a power source; this battery weighs 300mg, one of the smallest batteries in terms of size/energy criteria for given supply voltage [Buc 99]. The overall system weighs 750 mg (including batteries, Table 6 shows the weight of the each part on the board) and consumes 750µWatts static and 1 mW dynamic power. Even with continuous pulsing, the batteries last more than 5 hours. The line-of-sight transmission distance between the transmitter and receiver was measured at around 50m.

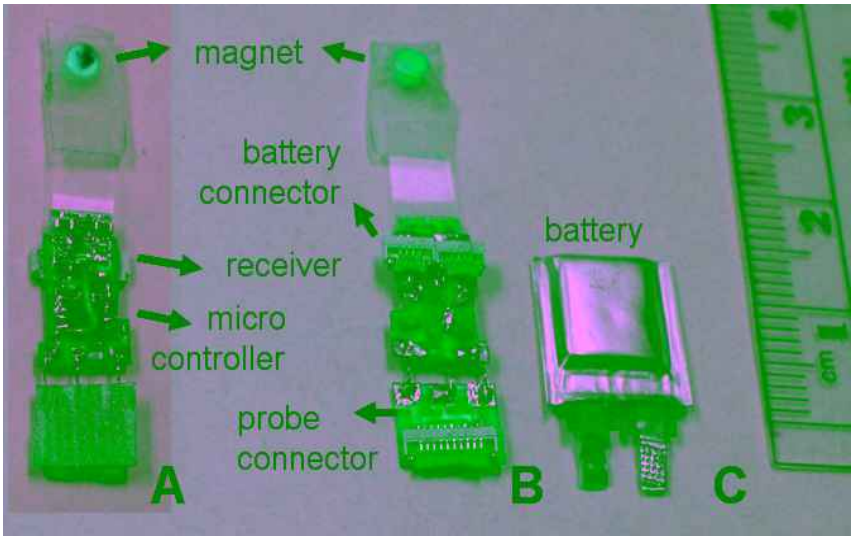

Figure 61: Front side of the assembled radio (A) holding the microcontroller and the receiver. The FFC/FPC connectors for the battery (C) and the probe can be seen on the backside (B). Magnets are also added for attachment of the helium balloon.

Table 6: Weights and Sizes of the Radio Controlled Stimulator Parts

component	weight (mg)	size (mm×mm)
receiver	70	6x5
microcontroller	15	4x4
probe	30	4x5
battery connector	15	2x4
probe connector	50	7x5
battery	300	13x12

The operation principle of the wireless remote controlled system can be summarized as follows (Figure 61): The position of the joysticks on the transmitter are converted into electronic signals and mixed into a PPM (Pulse Position Modulation) stream to be transmitted as AM radio signal at 72MHz. In PPM, the analog information is coded along the distance between the two positive edges of the pulses. On the receiver side, the super-regenerative receiver demodulates the AM signal into PPM code, which is then separated into different channels through the microcontroller and converted to pulse width modulated (PWM) waveforms to be applied to the tissue. As a result, the position of the joystick on the transmitter determines the duty cycle of the PWM pulses and so the amount of charge injected into the tissue.

4.3.3 System-on-Chip Solution

Combining silicon and system based expertise; recent developments in the system-on-chip technologies (SoC) have provided a number of capabilities by integrating process with function. The ability to fuse multiple systems on a single silicon chip has not only increased product functionality, but has also further enhanced quality and performance while cutting the development cycle.

Several SoC systems have been proposed to combine analog, digital and mixed-signal with radio-frequency functions on a single substrate level, especially for

embedded systems applications. A typical SoC consists a microcontroller, various memory blocks (ROM, RAM, EEPROM and flash), oscillators and phase-locked-loops as timing sources; ADCs and DACs as analog-digital interfaces; and voltage regulators with power management circuits. Some of these systems are tailored on the software level to fit in with high level communication protocols and standards such as Zigbee or IEEE 802.15.4 and thus enable small, low-power digital radios.

A backpack was also developed using system-on-chip technology as an alternative to the System-on-PCB backpack with surface-mount-components as described in the previous section. For this, a single chip solution from Texas Instruments (TI) was used. CC2530 from TI combines an 8051 microcontroller with a high performance RF transceiver, while providing 8KB of RAM and up to 256KB of flash memory. Optimizing the power budget of the intended application is also possible with its four flexible power modes. This single-chip system is an ideal solution for the insect backpack with its 21 general-purpose I/O pins and 8 channel 12-Bit ADC. The block-diagram of this system can be seen in Figure 62.

As the external components, CC2530 only requires a crystal oscillator with two loading capacitors, a bias resistor and a decoupling capacitor. All the required resistive and capacitive components are available in 0201 surface mount technology sizes (0.6 mm × 0.3 mm) to reduce the weight-loading and the overall circuit size. For the crystal oscillator, a quartz solution was used with a size of 1.6 mm × 1.2 mm. The circuit diagram of the backpack can be seen in Figure 63. The weight of the assembled backpack (Figure 64) is around 200 mg and has dimensions of $8 \times 17 \times 1$ mm^3. A line-of-sight reception range of more than 50 m was obtained. Including the batteries, the complete system is around 400 mg. The system connected to an insect through probes inserted in the dorsal thorax can be seen in Figure 65.

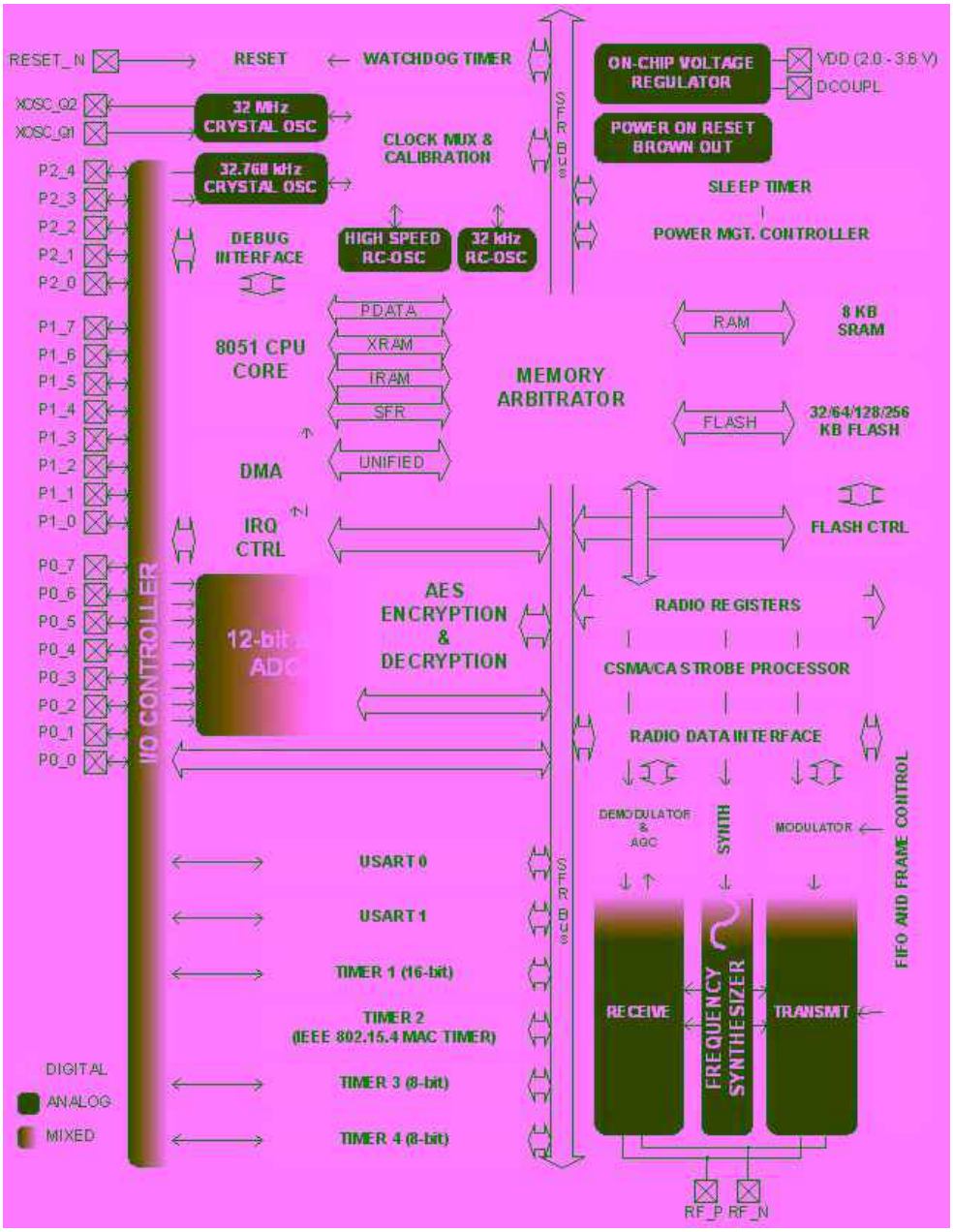

Figure 62: Block diagram of the CC2530 (modified from the datasheet) describing how different parts of the systems function and communicate on a hardware/circuit level

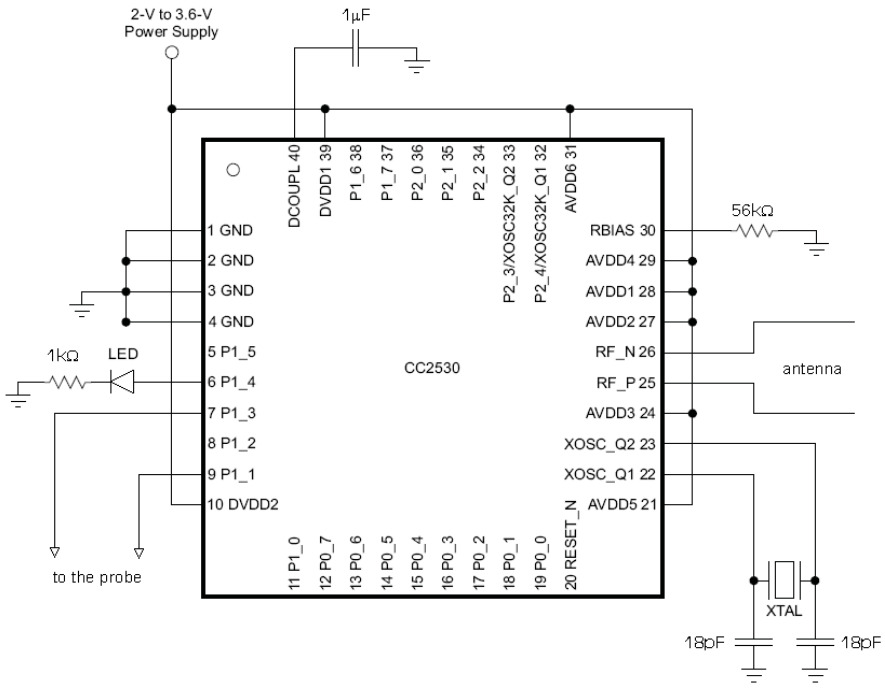

Figure 63: Circuit diagram of the SoC based backpack demonstrating the values and connections of the external components. An LED was added on the backpack to indicate that the system is turned on.

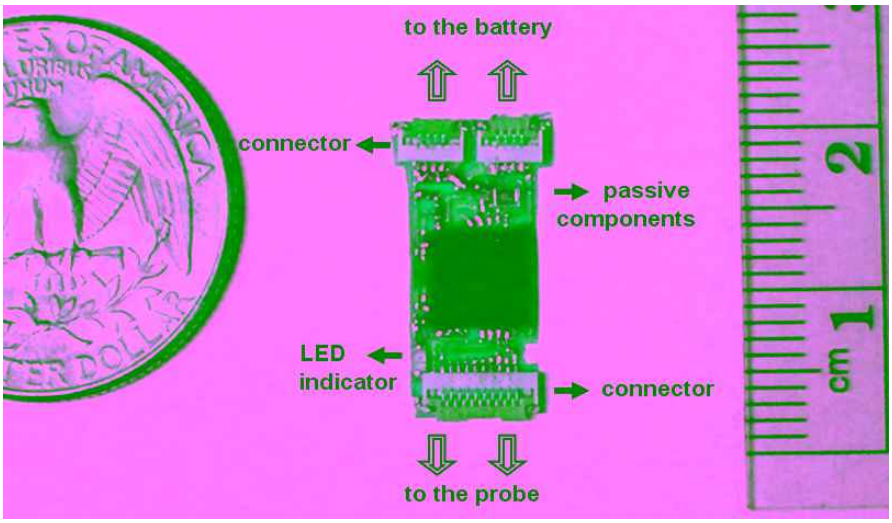

Figure 64: Assembled SoC based backpack with FFC connectors added for battery and probe connections

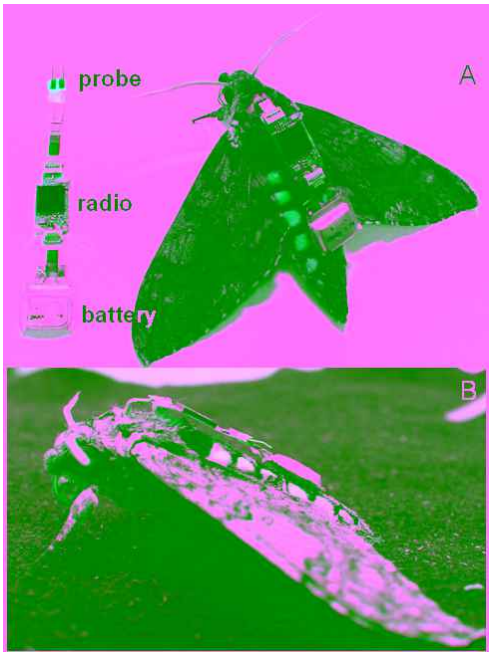

Figure 65: The Li-Po battery powered SoC based backpack is connected to the probe inserted in the dorsal thorax of the insect: (A) top view (B) side view.

4.3.4 Lift Assisted Backpack Technology

The payload capacity of most insects is limited to subgram weights, which restricts the application space of aerial and terrestrial insect biobots. *Manduca sexta* can carry up to 1-gram of payload. However, as the payload weight increases, the flight distance decreases from kilometers for 0g to approximately 5m for 1g and flight duration from hours for 0g to around 50s for 1g [unpublished observations]. To overcome this problem, balloon-assisted insect flight is introduced here to reduce the effective weight lifted by insect flight. For this purpose, a helium filled latex balloon was attached to the electronics board using two tiny magnets, one glued to the balloon side and the other to the printed circuit board holding the radio (Figure 66). Magnets provide on demand attaching/detaching. The lifting force of the balloon (~1g/L) was balanced with the weight of the insect and the electronic payload (~3g). Assistance with the lifting potentially increases the mission duration by conserving biological energy and also allows for adding other electronic components such as sensors and

actuators for further detailed analysis and control of insect flight. Experimental results are provided in Chapter 5.

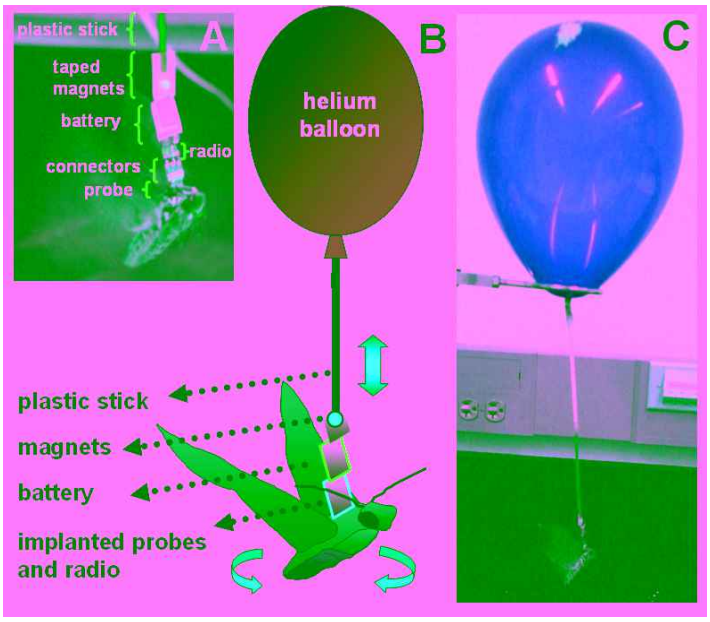

Figure 66: Description (B) of the balloon assisted flight setup (C). The details of the balloon to circuit connection can be seen in (A).

4.3.5 Discussion: Future Systems

Various technological platforms for locomotion control of the insect have been described throughout the preceding sections. It is possible to enrich these platforms with additional systems with different functions to increase the precision of remote navigation by localizing the insect's location more precisely. For this, MEMS based sensors can be embedded on the backpack to function as an accelerometer, a compass or GPS tracking. For the indoor locomotion control applications, the proposed lift-assistance mechanism in the previous sections would help the insect to carry additional weight due to these sensors and related electronic circuitry. The size, weight and power consumption of these systems decrease day by day, and adding these systems on the insect for outdoor applications will be more practical in the near future.

One concern with the described platforms is the requirement for charging the battery powering the backpack electronics for extended experimentation periods. Although the given Li-Po batteries can operate for days with the optimization of the power budget, for autonomous applications that require weeks of operation, the batteries need to be charged. One solution is inductively transmitting RF waves to charge the batteries while the insect is resting. It would be possible to scavenge some power piezoelectrically from the insect's own motion [Akt 08], [Rei 08]. Another solution and a more feasible one is embedding renewable energy storage on the system to benefit from available light sources by integrating photovoltaic devices on the insect. All these ideas are promising for increasing the mission duration of the hybrid insect-machine platform, while their deployment depends on the weight-loading they induce on the insect's locomotion performance.

CHAPTER 5
BIOBOTIC INSECT CONTROL

Navigating and domesticating insects such as *Manduca sexta* require the ability to elicit reproducible flight maneuvers. Different stimulation schemes need to be developed for each maneuver, and these maneuvers should be combined to obtain more precise and complex locomotion behavior. Different parts of the insect's locomotion control physiology could be tapped with an EMIT surgical procedure and various external stimulation methods could be applied to alter its locomotion. Below, experimental results obtained through electrical, thermal and optomotor stimulation of the insect's physiology are presented.

5.1 Electrical Stimulation of the Locomotory System

Injecting charge packets in the neuromuscular systems of the insect is the most straightforward and well-studied means to induce biomechanical output. The stimulation process of the various parts of the insect's locomotory anatomy is presented below.

5.1.1 Actuation of the Flight Muscles

As explained in Chapter 3, using the indirect flight muscles of *Manduca sexta* is one way to possibly control its locomotion. These main flight powering muscles are located in the dorsal-thorax of the *Manduca sexta* in which electronic implants can be located (Figure 35). The dorsovental and dorsolongitudinal muscle groups move the wings by changing the conformation of the thorax, which supplies the mechanical power for up and down strokes. The alternating relaxation and contraction of these muscles create the alternating up and down strokes, hence flight. Therefore, controlling flight by targeting and actuating these muscle groups may be possible. As

a starting point, to evoke a yawing maneuver, flight muscles *dl* and *dv* of a tethered *Manduca sexta* were stimulated by applying electrical pulses via indwelling probes, while motor nerve activity and wing movement were monitored (Figure 6).

5.1.1.1 Results of the Surgical Insertions.

The details of the post-surgical analysis obtained through dissections can be found in Chapter 2. Post-experimental X-ray and CT imaging were also performed to assess the success rate of the microprobe geometry for localizing the targeted flight muscles (Figure 67). A success rate of 98% was measured in more than 100 insertions. The few placement errors that occurred resulted from bending the probe in the muscle tissue during the insertion process.

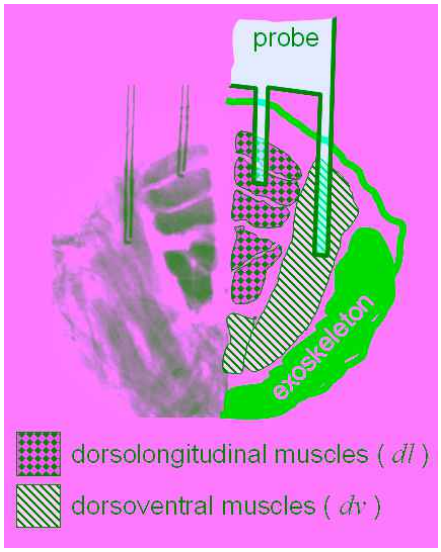

Figure 67: The X-ray image of the thorax shows probe localization to the targeted muscle groups with an explanatory schematic of thoracic flight muscles.

5.1.1.2 Rapid Inspection of the Bioelectrical Coupling

Flexible microprobes were designed and fabricated following standard micromachining procedures for flexible circuit technology, as described in Chapter 4. Twenty percent of the tested pads on late-pupae inserted probes did not actuate the flight mechanism due to the failed interface between the gold actuation pad and the muscle tissue. No systematic study was conducted to assess the failure mode. The

electrical coupling between the probe and the tissue was rapidly inspected before actuating the wing muscles using two methods: (a) measuring I-V curves across the different probes in a tethered flight setup and (b) recording the muscle potentials when the wings were flapping. The failed pads can easily be identified via pre-experiment I-V curve measurements. Typical I-V curves of satisfactory coupling and a failed probe can be seen in Figure 68. I-V measurements were performed on a visually quiescent moth using a Keithley-4200 I-V Characterization System. The interface between the probe pads and the actuated muscle fibers can be modeled with a simplified equivalent circuit. The detailed version of the model and the applied analysis can be found in Chapter 2. In this simplified model, R_M denotes the resistance of intra- and extracellular fluids of muscle fibers, whereas R_I and C_I are the resistance and capacitance at the metal-tissue interface. Other elements such as the resistance of the metal trace and the capacitance of the insulator between the metal trace of the electrode and the conducting interstitial fluid were omitted because they are negligible. Lines were fitted to the I-V curves at DC in order to give the approximate addition of R_I and R_M. The obtained resistivity sum from this analysis (ρ; see Table 7) for the satisfactory probe-tissue interface is in good agreement with the reported skeletal muscle resistivity (300-500 Ω·cm) [Zhe 84, Spe 61, Spe 91] and the metal-tissue interface resistance measured in 0.9% saline solution (75 Ω·cm). Failed probes, however, give abnormally reduced resistivity values, as indicated in Table 7.

Table 7: Lines Fitted to I-V Curves in Figure 68 to Calculate Resistivities (Channel 4 with Poor Electrical Coupling)

Channel	Trendline	ρ (ohm·cm)
Ch1	x = 516,804y	484
Ch2	x = 303,739y	285
Ch3	x = 354,742y	332
Ch4	x= 22.9y	0.021

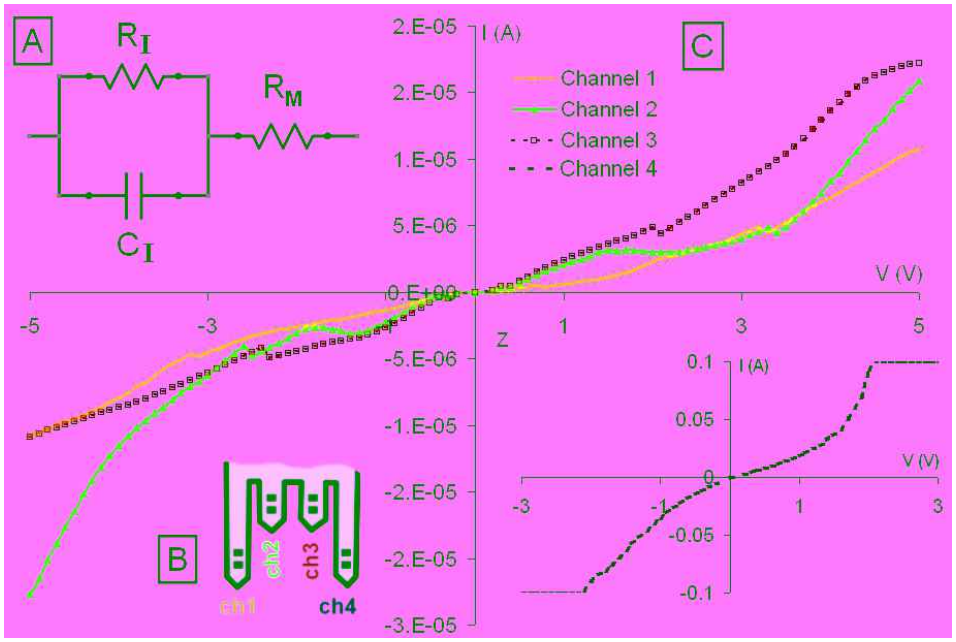

Figure 68: I-V curves of each electrical pad (C) and a simple RC network (A) modeling the muscle between the pads. The pad diagram is given in (C). In this example, Channel 4 (shown separately in 4th quadrant) has poor bio-electrical coupling.

The implanted probes can also be used to record electrophysiological signals during natural flight in order to study locomotive behavior (Figure 69). A good muscle potential recording was regarded as an indication of the integrity of the probe operation. The observed inter-spike duration is consistent with the wing flapping rate of moths (20–25Hz). Further feedback studies of insect muscle can be conducted to optimize flight control by recording and analyzing the phase difference between *dl* and *dv* muscle and altering this difference through these recordings. Such an analysis is beyond the scope of this dissertation, but the recording capability was used solely to assess the success of bioelectrical coupling. Probes and insects that failed in any of these tests were not tested any further. Working intramuscular electrodes were capable of efficiently exciting the motor neurons arborized within the muscles in which they were implanted. These electrodes were used to control the muscle motion.

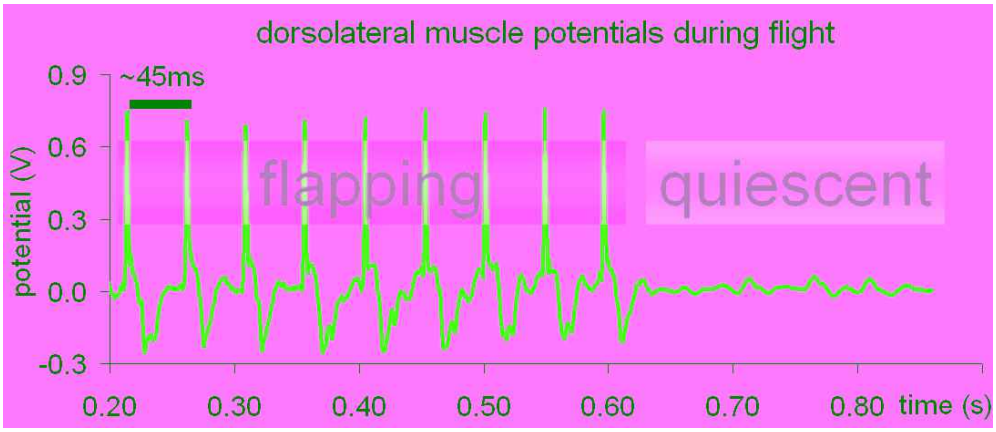

Figure 69: Actuation probes were also used to record muscle potentials as an indication of efficient tissue-probe coupling. Potentials recorded from the dorsolongitudinal muscles (multiple-cell recording with 50-100 times amplification) have spiking frequency similar to wing-flapping rate (~23Hz). Observed spikes disappeared immediately when wing flapping stopped.

5.1.1.3 Neuromuscular Stimulation of a Resting Insect

The phased actuation of the *dl* and *dv* muscles with biphasic pulses allowed us to control wing motion in a highly selective manner. The outputs of the stimulation outcome were simultaneously monitored at motor output level. When the moth was resting in a quiescent state, stimulating the *dl* muscle on one side of the insect caused the wing on that side to move downward, whereas stimulation of the *dv* muscle caused the wing to move upward. The depression and elevation of the wing persisted as long as the stimulation was continued and both bilateral and unilateral wing actuation were demonstrated reproducibly. Following stimulation cessation, the wing rebounded passively to its resting position as a result of thorax elasticity (Figure 70). A wing rebound time of around 250ms was measured using a high speed camera. Upstroke and downstroke actuation on "one" or both wings were demonstrated with power consumption as low as 10 microWatts (V=2.5V, I=4μA). An even lower stimulation current was required for longer stimulus pulse width to create similar wing actuations. Pulse application frequency ranges were swept between 1 and 10 Hz to separate the effect of contracting *dv* and *dl* muscles visually and temporally. The wings followed a

similar flapping frequency with the applied pulses. The wing actuation and flight direction can be seen best in a visual movie format (see appendix).

5.1.1.4 Neuromuscular Stimulation of a Naturally Flying Insect

When a unilateral stimulation pulse was applied to a tethered insect flying naturally in a straight direction, the most striking effect was a yawing maneuver towards the stimulated side. A backward shift of the wings occurred on the stimulated side, whereas the wings on the opposite side were drawn forward (Figure 70). Flight stopped immediately when these two muscles contracted simultaneously with high frequency pulses (70-100Hz). When the *dl* and *dv* muscles were activated together, they opposed each other, stopping the wing flapping altogether (Figure 71). These initial results prove the concept of steering an insect by applying external stimuli through implanted structures.

5.1.1.5 Discussion: Characterization of the Motor Output

Being beyond the scope of this dissertation, quantitative parameters can be set to evaluate the output of motor response obtained from the insect's wings. For this process, a mechanical model of the wing can be built to evaluate the related model parameters. The indirect flight muscles of *Manduca sexta* can be modeled using a damped mass-spring system (Figure 72). The muscle itself acts like a spring having an origin in a fixed, more proximal part and an insertion in a distal, movable part. The cross-bridges formed by the muscle fibers are modeled as a force generator (f_m) connected in series with elastic spring elements of the muscle (k_m) and the connective tissue joining muscles to the cuticle. The wing and air resistance is the load (m_w) suspended from these springs. The antagonistic muscles are also represented as resistance to movement. This model can be embedded in another larger scale model that represents the relationship between the neural input and the produced motion output.

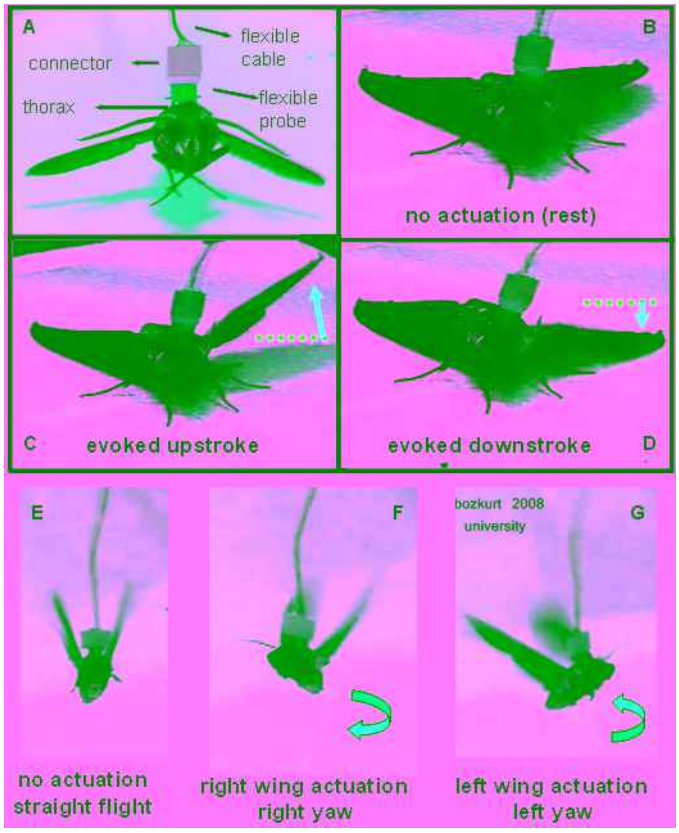

Figure 70: Evoked up- and downstroke of a "single" wing (A-D) obtained by applying 5V pulses to the indirect flight muscles (snapshots from the recorded movie). Under natural conditions, moths flap both wings together. Illustrated responses to pulse application to the wings during natural flight (E-G).

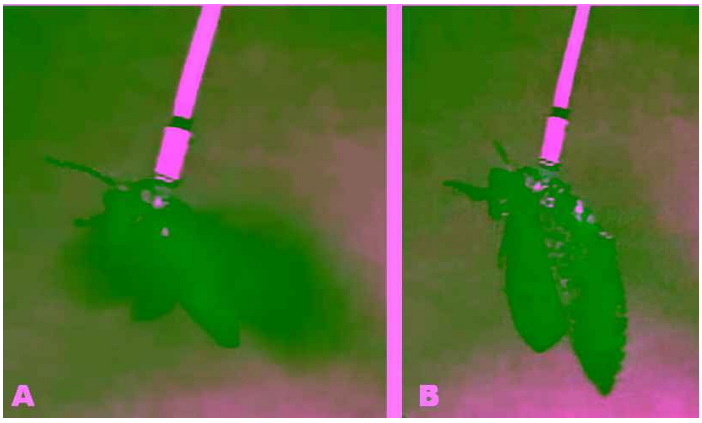

Figure 71: Contraction of *dl* and *dv* together during natural flight (A) with high frequency pulses stops flight (B). Flight continues as the induced contraction is removed.

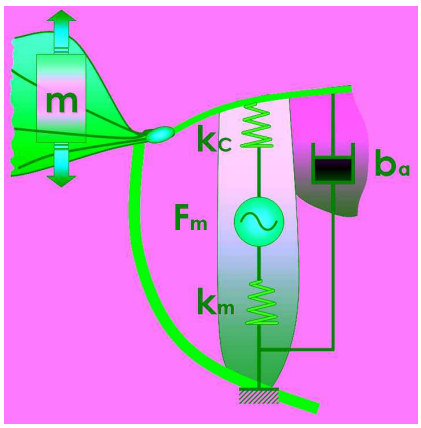

Figure 72: The *dv* muscle of *Manduca sexta* modeled as a mass-spring system where Fm denotes the force driving the system, k_m is the spring constant of muscle, k_c is the spring constant of the connective tissue and b_a is the damping caused by the antagonistic muscle group (*dl*).

5.1.2 Actuation of Antennal Lobe and Neck Muscles

After the flight muscles, antennal lobe and neck muscles of *Manduca sexta* were stimulated for locomotion control on both *land* and *air*. Physiological details can be found in Chapter 2 (Figure 30). In this study, the concept of lift-assistance was utilized, as explained in Chapter 4, to help the insect carry the payload.

5.1.2.1 Results of the Surgical Insertions

As in the previous experiments, the metamorphosis based surgical insertions of artificial structures in the insect were the key strategy here to enable a hybrid biological and technological pathway towards obtaining remote controlled insect biobots/cyborgs. Therefore, the wire electrodes described in Chapter 4 (Figure 33) were inserted in the insect following the EMIT procedure. These electrodes can possibly be replaces by their counterparts fabricated through the flex-PCB fabrication techniques (Figure 74). The adult insects emerged from pupae 5–7 days after the surgical insertions (Figure 8) with an average weight of 2.2g. The successful emergence rate was 84% (N=30) and 80% of these adults were able to inflate their wings successfully. The successful target localization obtained through Micro-CT

imaging (with a success rate of 100%) can be seen in Figure 73. The healing and tissue-growth around the inserted probe provided a secure payload attachment to the insect, as a result of the EMIT procedure that eliminated the need for synthetic adhesives (Figure 8). After emergence, the control electronics and power layers were connected to the probe body through the FFC connector in 5-10 seconds without requiring any anesthesia (Figure 73).

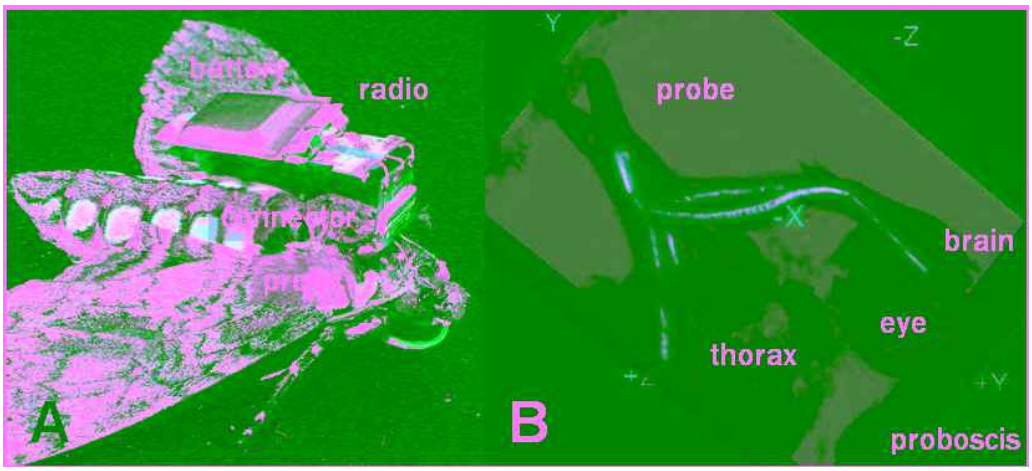

Figure 73: Reconstruction of the X-ray images (E) of the insect reveals the location of the metal-wires in the thorax and brain (metal wires lighter color). The radio-controlled stimulation system is assembled on the adult insect (D).

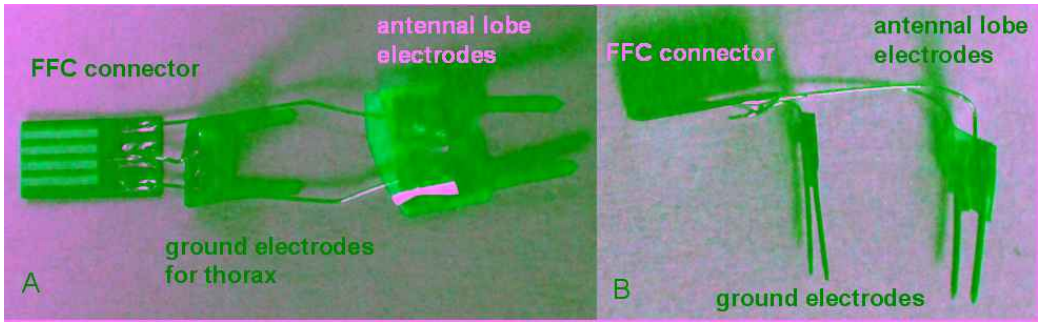

Figure 74: Flex-PCB based electrodes to replace the wire electrodes targeting antennal lobe described in Figure 33: (A) top view of electrodes before bending (B) side view of electrodes after bending.

5.1.2.2 Aerial Control of Lift Assisted Locomotion

The two major side-effects of the weight-loading on the insect were a delay in flight initiation through an extended shivering process and a diminished cruising height, as explained in Chapter 4. Under natural conditions, these insects warm up their thoracic muscles before flight through shivering by contracting their elevator and depressor muscles at the same time, as explained in Chapter 2. This process takes about 5 minutes and increases the lifting force of each wing-beat from 50 to 300 mg/cm^2 [Hei 74]. Therefore, an extension of this process is required to lift larger weights. Up to 8 minutes shivering time was observed on the loaded insects. Even with an extension of this period, moths were not able to lift themselves up more than 5–10cm over the ground with the addition of 750 mg weight. On the other hand, the shivering process does not always result in flight initiation under natural circumstances. The rate of shivering-without-flight for the insect increased from 30% to 85% with the added payload.

The helium balloon with around 3 liters of volume (diameter approximately 13 cm) was able to lift the insect with the added electronics. In addition to increasing the payload capacity, lift provided by the helium (1g/L) helped the insect to conserve the energy used for lifting its own body weight, thereby potentially increasing the duration of the mission. This approach also allows for adding other electronic components, such as extra power sources for extended mission duration, sensors for environmental sensing, cameras for surveillance or actuators for further detailed control of insect flight.

For aerial locomotion direction, two sets of experiments were performed on *Manduca sexta.* In the first set, insect locomotion was restrained for a close-up camera investigation by introducing a restricting annular ring around the stick-connector connecting the radio to the balloon in the aerial case (Figure 75). Behavioral changes

with the applied pulses were observed and video recorded during balloon assisted free-flight in order to digitize the data for further analysis in a computer environment. The actuation of the targeted regions with electrical pulses sent from the transmitter to the antennal lobe caused wing flapping on a resting moth, indicating successful electrical coupling. A typical DC resistance in the order of 3MΩ/cm was measured between the wire electrodes, as a quick inspection of the interface. In the restrained setup, natural flight was initiated with pulses sent to the antennal lobe (3.5Vpp–20Hz–50% duty cycle) (Figure 76). After flight was initiated, actuation of the neck muscles with similar pulses elicited controlled yawing of the insect (~60–80°/s) (Figure 76). Flight ceased immediately when the antennal lobe was stimulated with high frequency pulses (3.5Vpp–50Hz–50% duty cycle). Unrestrained free flight was successfully enabled by removing the annular ring in which a three-task mission of lifting-off, yawing and landing was demonstrated with freely flying insects. A typical trajectory of insect position obtained during this mission can be seen in Figure 77. To exhibit reproducibility, the same mission was repeated three consecutive times on three different trials. All of these results can be best seen in movie format (see appendix). By feedback controlled learning of yaw motion obtained in various insects, it is plausible to ascertain the best positions for probe placement and optimized pulse sequences.

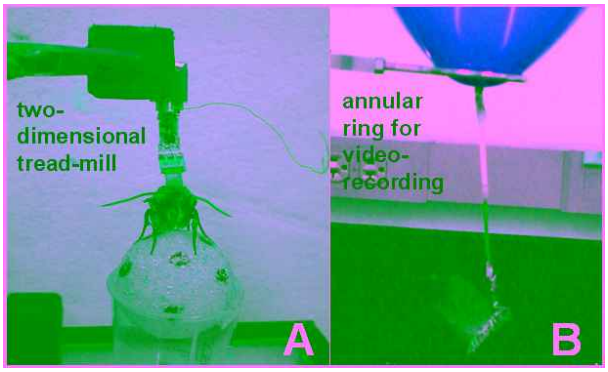

Figure 75: Description of balloon assisted flight and walk setup with retaining rings inserted for stable recording purposes

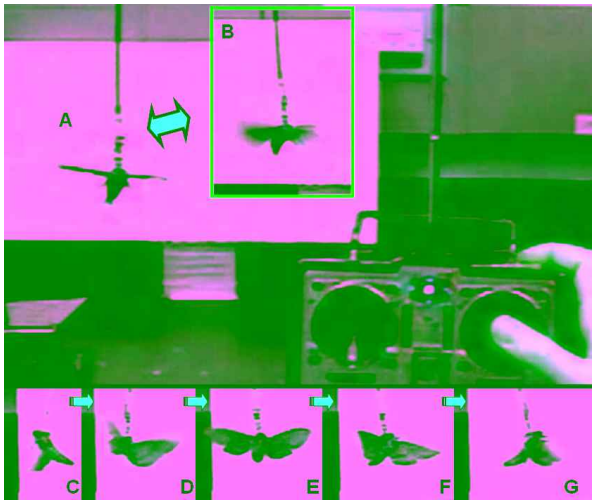

Figure 76: Snapshots of the video demonstrating the results of the RC actuation experiments. Pulsing of the brain initiates flight (B) on a resting moth and stops flight (A) when the moth flies. The screen captures the insect's yaw (C-G) obtained through joystick manipulation.

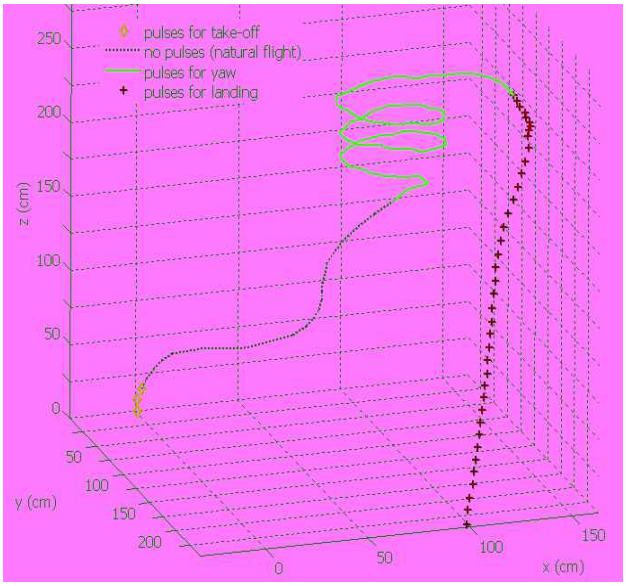

Figure 77: Digitized flight track of the moth as a result of applied stimulation pulses. Circular flight control is demonstrated by the red circular trajectories.

5.1.2.3 Terrestrial Control of Lift Assisted Locomotion.

For the terrestrial experiments, adult insects were anesthetized and the wings were removed using surgical scissors. No behavioral disturbance of the insect was

observed due to wing removal, as expected, since the wings are passive cuticular airfoils. Two sets of experiments were performed on these wing-removed *Manduca sexta* for terrestrial locomotion direction. In the first set, the insect was placed on a low friction foam ball, which acted like a two-dimensional treadmill to restrain the locomotion for a close-up camera investigation (Figure 75). Later, these restrainers were removed and behavioral changes from the applied pulses were observed and video recorded during the balloon assisted free-walk.

Similar pulses to the aerial control were applied to the wing-removed insect for terrestrial control. On the two-dimensional treadmill, actuation of each side caused rotation of the ball towards the opposite direction (~360°/s) simulating the turning of the insect towards the actuated side. When the insect was released for a free-walk, the continuous actuation of one side caused the insect to follow a circular path in that direction. A mission of following consecutive "8" shaped routes was demonstrated with these freely moving insects (typical trajectory in Figure 78) (see the appendix for the movie information).

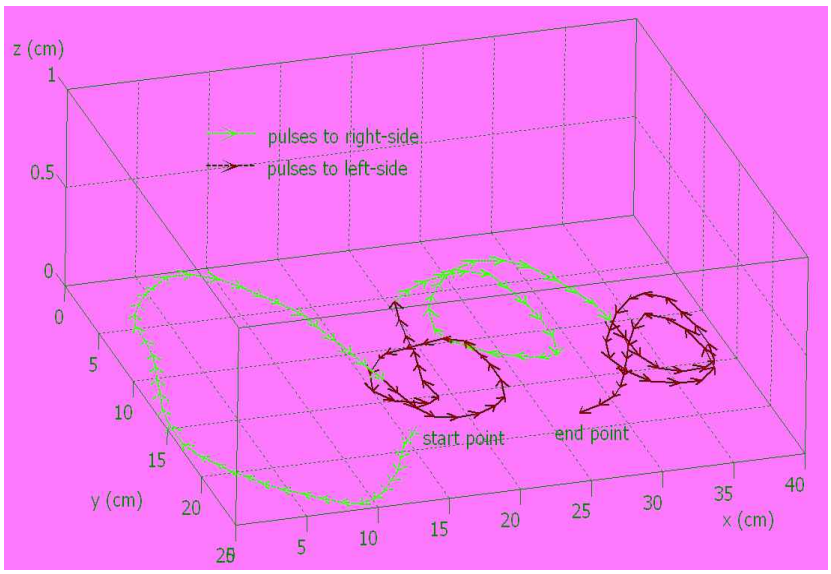

Figure 78: Digitized walking track of the moth as a result of applied stimulation pulses

5.2 Thermally Induced Flight Control

If one is to realize hybrid-insect flyer with tissue embedded electronics for flight control, the thermoregulation paradigm presented in Chapter 2 makes the take-off period of hybrid flyer a strong function of the environment. A slow take-off period would reduce the bandwidth with which flight operations could be controlled. Experimentally, a pre-take off warm-up duration of 5–10 minutes is required to deploy a hybrid insect system under room temperature conditions. To mitigate this potential show stopper for stable flight control, micro thermal-heaters are reported in this section to be inserted into the dorsal thorax of the tobacco-hawkmoth *Manduca sexta* in the pupal stage. When the adult emerges, artificial heating of the muscles can be used to enable faster flight initiation and flight control. In addition to flight control, these probes allow one to study thermodynamics of muscle actuation in insects, possibly translating to design principles of other biohybrid systems.

5.2.1 Results of the Surgical Insertions

The thermal-probes (Figure 52, 53) were inserted at the center of the thorax of male-pupae seven-days before eclosion using the EMIT surgical procedure (Figure 79). A successful emergence-rate of 75% was obtained with the implanted thermal probes where the remaining 25% of the insects did emerge but with deformed wings due to hitherto unknown reasons. Post-experimental dissections demonstrated successful localization in the center of the thorax (Figure 79). The probes were integrated in the tissue and no encapsulation around the probes was observed. The cuticle around the probe had healed and tightly sealed the probes to the body, which prevented any mechanical movement of the probe within the tissue.

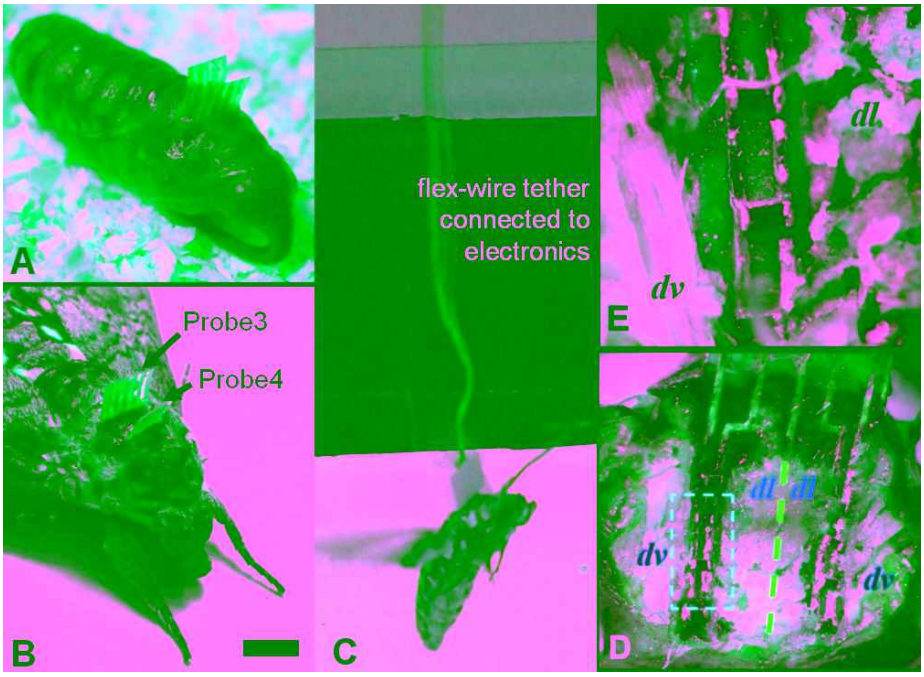

Figure 79: Double probes for heating (probe 1, 2 or 3 on Figure 53) and recording (probe 4) inserted to the center of pupal thorax (A) with a distance of 2mm and successful emergence (B). Double probes were deployed via the flex-wire tether (C) connected to the data acquisition system and power supply electronics. Post-experimental dissection (D) of thorax showing the location and biocompability of the thermal probe. The symmetrical probe targets both sides of the thoracic musculature (see the symmetry axis as the dotted red line). When the marked square on (D) is zoomed-in (E) dl and dv muscles can be distinguished easily (see Figure 18 for *dl*, *dv*). The scale-bar (B) represents 5mm.

5.2.2 Thermal Recording and Modeling

The implanted probes were connected to a semiconductor characterization system (Keithley™ 4200) after the emergence of adult insects in which the temperature was read by converting the voltage into temperature using a calibration table. First, natural temperature trends were recorded through the thermistors during preflight warm-up and flight activity of the moth. Then, heat was applied to the thermodes of quiescent insects at laboratory temperature (20ºC) while induced temperature on implanted thermistors was also recorded as a function of time and applied power in order to determine thermode values and the geometry required to obtain thoracic-temperatures similar to the natural trend. Finally, the preflight warm

up duration of the insect cyborg was measured while heat was applied to the thorax of the insects at the same time that the internal temperature was monitored through implanted thermistors.

The insect thorax can be simply modeled as a thermal capacitance, where stored heat can escape to the environment through thermal resistances (Figure 80). The net heat flow depends on heat sources and thermal resistances and can be expressed in terms of the system's state variables: the temperature of the thermal capacitances. The state variable model for this system is

$$\frac{\partial T}{\partial t} = \frac{1}{C}\left[Q_{in}(t) - Q_{out}(t)\right] \qquad (1)$$

$$\text{where} \quad Q_{out}(t) = \frac{A\kappa}{d}\left(T(t) - T_a\right)$$

The temperature response of the muscle to a unit step function in heat input is an exponentially increasing temperature that saturates to a steady state value.

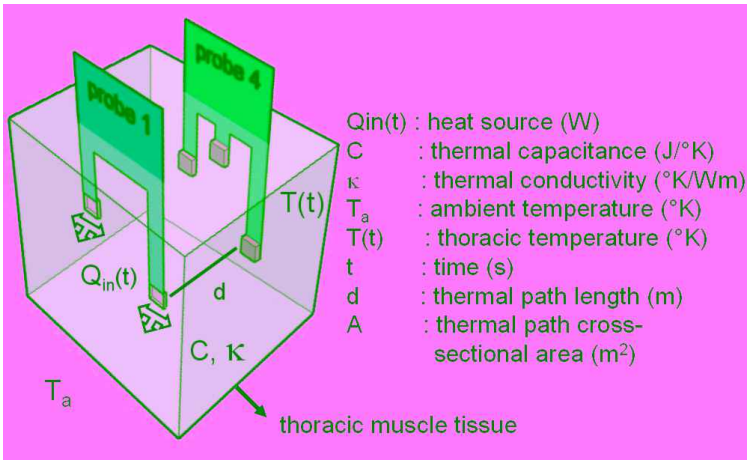

Figure 80: Thoracic cross-section modeled as a thermal system with the indicated thermal model parameters (heater and sensor elements are illustrated as probe 1 and probe 4 in Figure 53, respectively)

5.2.3 Endogenous Heating of the Thorax and Behavioral Results

The recorded natural temperature trend of an insect performing pre-flight warm up and flight behaviors can be seen in Figure 81. An average of 7 minutes was

required for *Manduca sexta* to reach 39ºC at room temperature (20ºC) before taking off. Next, 50mW of power were applied to each thermode in parallel on each probe and the average thoracic temperature was recorded using the thermistors (Figure 82). Larger numbers of heaters provided more uniform and faster heating as expected.

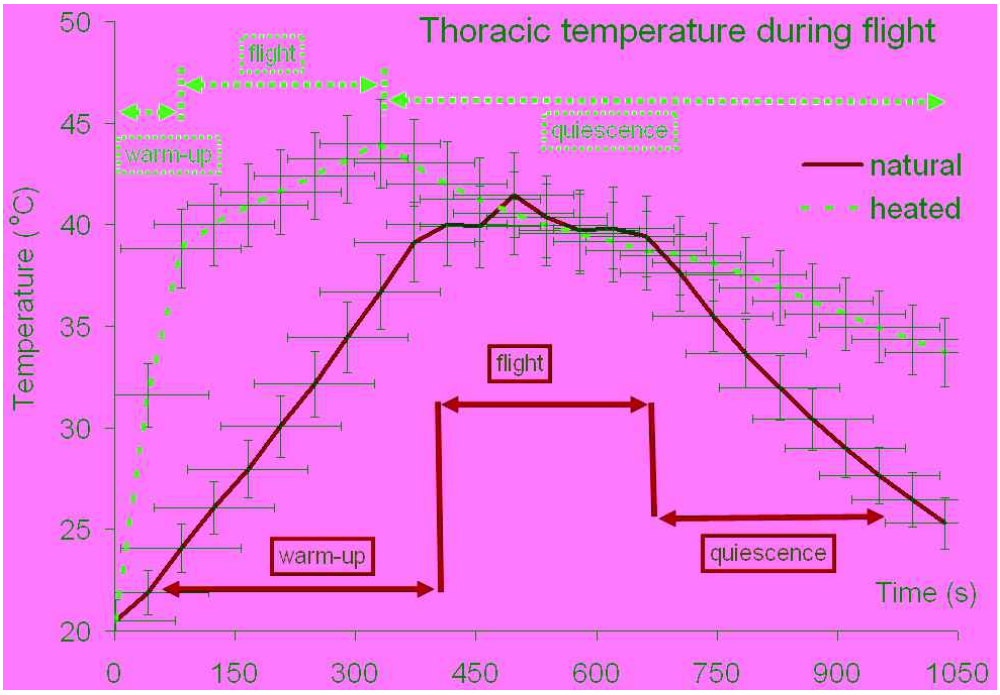

Figure 81: Temperature of the thorax measured during warm-up, flight and post-flight quiescence periods for natural and artificially heated conditions. The heat was kept on throughout the entire experiment. Data are given as mean +/- SEM of 3 moths.

The recorded values for each thermistor were fitted to equation (1) in order to calculate the heat capacity and thermal conductivity to match the values reported in the literature (Figure 82). The calculated values are in good agreement with the range reported for skeletal muscle in the literature (0.2–0.6 W/mºK for κ and 2–4 J/gºK for C) [Nga 98, Pon 91, Lan 95].

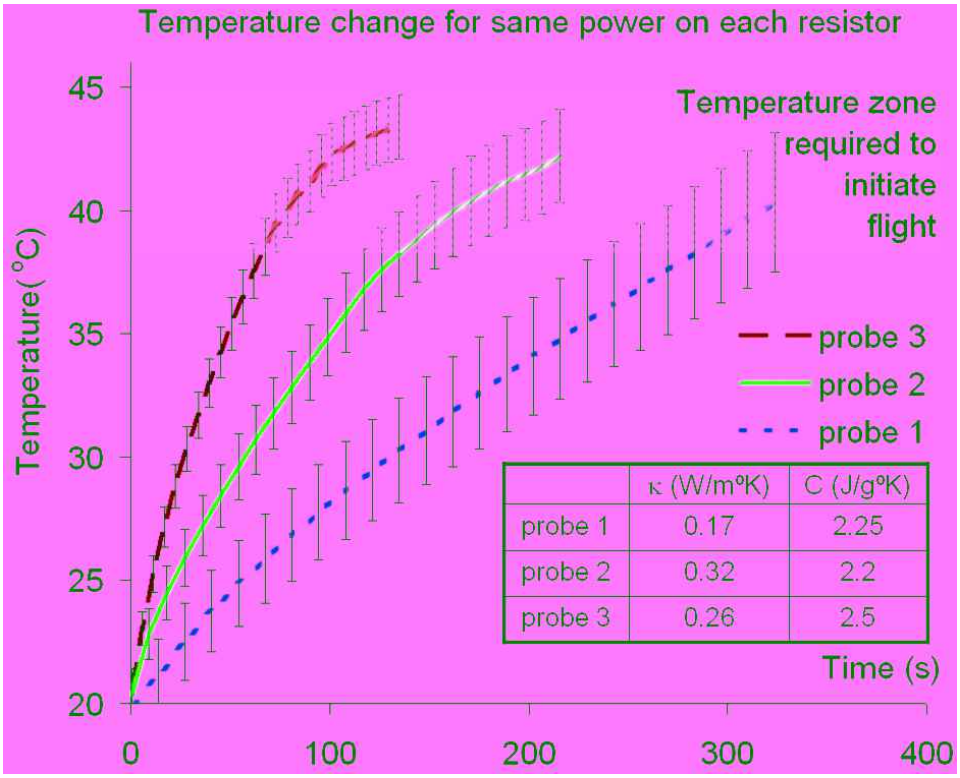

Figure 82: Change in the thoracic temperature of 3 tethered insects when 50mW was applied to each resistor on the probes in parallel (see Figure 53 for probe numbers). Table shows the specific heat capacity and thermal conductivity obtained from the curve-fit. Data are given as mean +/- SEM.

Subsequently, the time required to reach a thoracic temperature of 39ºC was measured for each probe for different powers (Figure 83). The time predicted by the model for each probe is also provided. Throughout these recordings, the insect was in a non-shivering quiescent state. After these measurements, 50mW of power were applied to Probe 3 in Figure 79 and the flight behaviors of the three insects were observed and videotaped. Preflight warm-up duration was decreased to 58 seconds, from the natural average of 7 minutes, in a room temperature environment on the tethered setup (Figure 81).

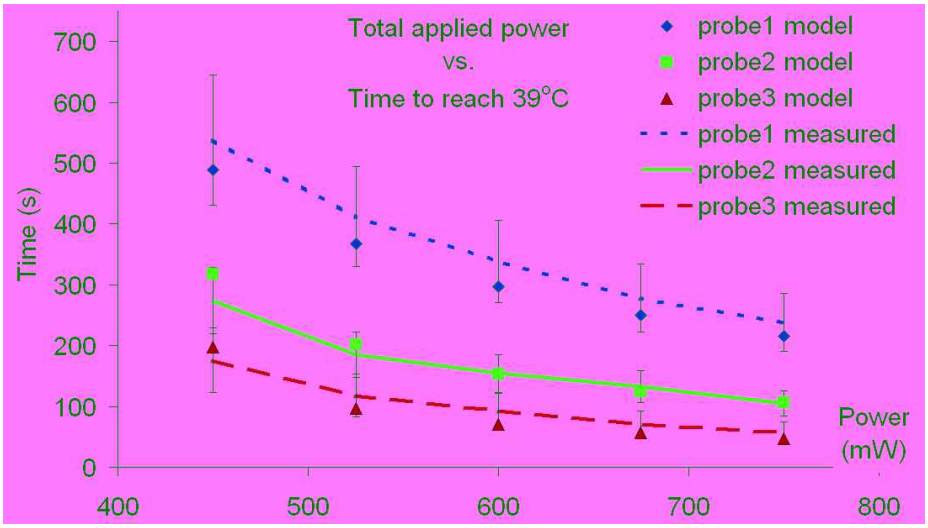

Figure 83: Time required for each probe to induce 40°C in the tissue as measured on probe 4 (probe numbers given in Figure 53) and provided by the model in Figure 80. Data are given as mean +/- SEM of 3 insects.

An average preflight warm-up duration of 62 seconds was obtained when the untethered battery powered printed circuit board was used (Figure 52). Standard 8 mAh capacity watch batteries can supply this power for 4800 s (75 times the required duration). A temperature drop was observed on the heated thorax during the post-flight quiescence period (although the heat was still on), due to circulatory cooling and the cessation of muscle actuation. Natural shivering behavior was also observed during the last 10 seconds of the artificially heated warm-up period.

5.3 Optomotor Flight Control

To observe the capability of locomotion control through exteroceptive input applied to the optical lobe, a visual simulator was built to identify the relevant parameters of the optic-flow motor-output coupling (Figure 84). Similar setups, first samples being patterned on rotating cylindrical drums on motors, have been used for a long time [Van 50]. The cylindrical LED-arena was programmed to create a virtual rotating environment around the vertical body axis of the moth. Green was used as the LED color because 75% of the visual receptors are green-sensitive [Cut 95]. The moth

is free to rotate around itself through the ball-bearing to which it is attached. The attachment is achieved through a wire loop and an "EZ-hook" (Figure 85). In this setup, the experienced optical flow depends on the moth's own actions similar to free-flight.

The *Manduca sexta* demonstrates object-fixation behavior which is gated in the visuomotor pathway (see appendix for the movie result). During flight in the optical simulator, the visual system of the moth experiences continuous retinal images changes. While turning to one side, the entire retinal image shifts in the opposite direction. This shifting is called the optical flow. The rotation related optical flow is independent of the distances of the objects in the visual surround. The *Manduca sexta* processes optical flow to create optomotor responses to stabilize the retinal images [Mil 87]. In the cylindrical LED arena, the fixation can only be achieved as an effect of turning flight. As a result, visually motivated right-left yaw was obtained and video-captured. This fixation based yawing action can be characterized for different locations, sizes, speeds and intensities of the light stripes in order to find the limits and delay of tracking.

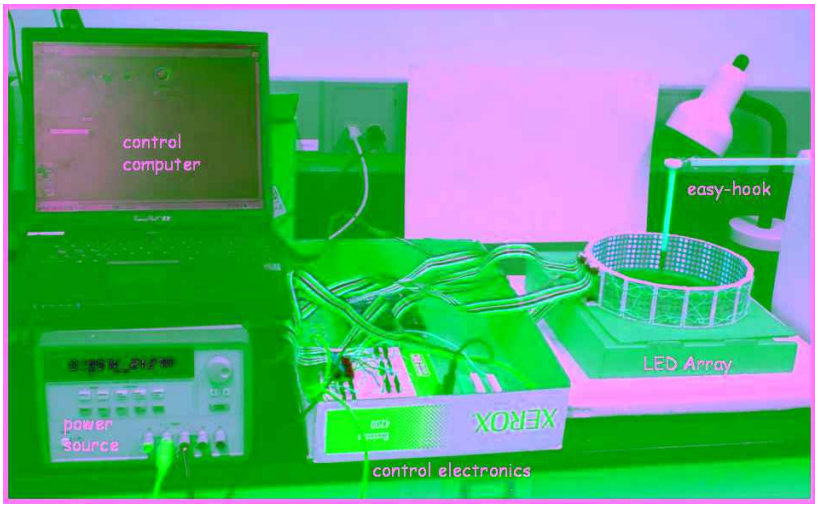

Figure 84: Computer controlled "LED Arena" for frame of reference perception induced motion illusion. Computer runs LabView™ code through the control electronics to turn on some of the 630 LEDs in the arena.

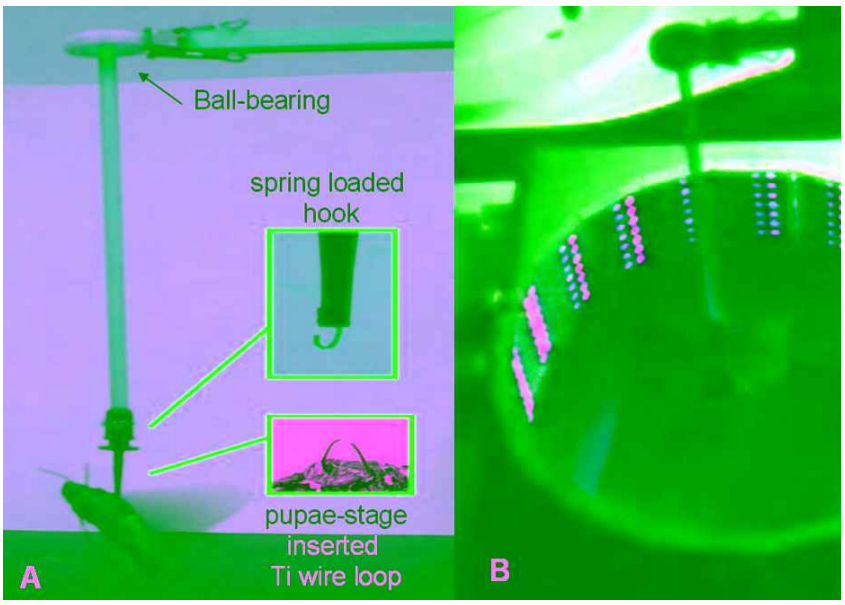

Figure 85: Ball bearing set-up with developed "easy-hook" method for limiting the degree of freedom to "yawing" only (A). The metal wire loops for attachment are inserted in the insect through the EMIT process. Insect is located in the middle of the LED arena with this tool to obtain right and left yaw (B).

The LED arena is controlled by a LabView™ (National Instruments, Inc.) code generating rotating bright stripes. The intensity, rotation speed and direction are all adjustable. This flexible virtual environment can be used as a "test-bed" to investigate the responses of indirect flight muscles and direct steering muscles to oscillatory left-right optical flow through the EMIT surgical procedure implanted microprobes. In this way, a minimal model of neuromuscular signals obtained from the probe related to visually guided rotation behavior can be identified. Similar electrophysiological signals obtained from the model can be reapplied to study the obtained motor response.

The same simulator can be rotated 90^{o} to create a rotational background around the horizontal body axis to induce pitch angle change. For this setup, the insect also needs to be tethered in the horizontal plane to a similar circular ball bearing. In this rotated simulator, if a linear ball bearing is used instead of a circular one, induced lift and thrust can also be achieved with proper LED light rotation [Fry 01]. All of the six

degrees of freedom can be studied by rotating the LED Arena to an appropriate angle and using linear or rotational ball bearings.

Figure 86: Implantable miniature LED arena (old version with 2 LEDs on the left and bigger version with 12 LEDs on the right) for optomotor steering of the insect.

Furthermore, the LED arena can be miniaturized in order to be implanted on the insect to study its free flight response to the rotating light. The visio-motor reflexes to rotating light have the potential to be used to steer the insect through a radio controlled miniature LED arena embedded on the insect in an untethered setup (Figure 86).

CHAPTER 6
CONCLUSION

Controlled by neurons, muscles are actuated to do mechanical work by converting chemical energy into mechanical power. Throughout history, humans have benefited from the muscle power of animals for farming, transportation and industry, the backbones of civilization. These achievements were possible through the domestication process, mainly selective breeding of different species that are trainable by humans. With recent developments in micro- and nanotechnology and neuroengineering, it may be possible to achieve this goal through direct "biobotic" control of the neuromuscular system. Insects are especially promising candidates in this regard because of the relative simplicity of their locomotion control system. This dissertation described methodologies involved with developing neuromuscular microsystems to control and domesticate insect locomotion.

Early Metamorphosis Insertion Technology (EMIT) is a novel neurotechnological pathway for integrating microelectronic sensing and actuation platforms on insects during metamorphosis to enable IMI (Insect Machine Interfaces). Inserting the probes at an early pupal stage ensures that the tissue grows around the probes for a highly natural implant. The muscle tissue develops around the inserted probes during pupal to adult metamorphosis, increasing the mechanical stability and integrity of the structure on the insect. The metamorphic development not only provides an elegant and effective method of mechanically affixing artificial systems in or on an insect, but also enables a reliable bioelectrical interface without any observable adverse effect on insect flight behavior. The experiments presented here show that a reliable bioelectronic interface has been realized for recording and controlling the motor function of insect muscles.

The EMIT procedure has opened a window for neuro-engineers to explore the details of insect flight neurodynamics and its control by allowing the implantation of various micro-devices through a simple surgery that results in little or no tissue damage. Following our initial demonstrations, other groups have also presented similar achievements by stimulating the abdomen of moths on tethered setups [Tsa 08] and the brain and the wing muscles of beetles [Sat 09].

Insects demonstrate genetically programmed stereotypical behaviors triggered by environmental stimuli. Therefore, as shown in this dissertation, direct control of insect locomotion behavior through electronics is more straightforward than for larger animals, e.g., rats and monkeys. Based on the initial results presented here, more advanced electrical neuromuscular control strategies can be developed to instruct insects to navigate and to learn particular tasks using routine-operant conditioning techniques. In the experiments done within the context of this dissertation, motor output was generated by applying proprioceptive inputs directly to the peripheral neuro-muscular systems. However, to stimulate behavioral responses, additional payloads can be implanted with the surgical procedure presented here to provide exteroceptive inputs to the insect's chemical, mechanical and visual receptors. These concepts have significant potential for training individual insects remotely to control their behavior.

As an application, the first results towards flight navigation in moths were established here. We were able to demonstrate on-demand wing actuation and flight direction control using microprobes inserted through the EMIT procedure, with the goal of insect navigation and domestication. Inserted probes were adopted by the developing muscle tissue as a result of metamorphic growth in which the surgical method was completed in less than a minute to embed the excitation electrodes directly into the indirect flight muscle groups. The muscle tissue developing around

the inserted probes increased the mechanical stability and integrity of the structure on the insect. Separate down- and up-stroke actuation of each wing was shown, through which the flight direction of *Manduca sexta* was affected. Using this procedure, we were able to alter and control the flight of tobacco hawkmoth *Manduca sexta* by actuating its flight muscles on tethered setups.

Successful locomotion control for both land and air was also demonstrated for the first time with remotely transmitted radio signals through electrodes inserted in the antennal lobe and neck muscles of the insect following an EMIT procedure. Initiation and cessation of flight and walk, as well as yaw actuation were obtained on freely flying and walking lift assisted moths through joystick manipulation on a conventional model airplane remote controller. Super-regenerative receiver based architecture was used to receive transmitted signals from a remote controller to stimulate the insect, where the overall circuitry weighed only 650 milligrams and consumed 750 microwatts. By feedback controlled learning of yaw and rotation motion obtained in various insects, it is plausible to ascertain the best positions for probe placement and optimized pulse sequences for improved precision.

The concept of lift assisted flight allows for transporting tens of grams while potentially increasing the flight duration of the insect biobots, enabling a vast number of engineering applications where such biobots can be deployed. Helium balloons were also used to assist the insect to lift the payloads. In our ongoing effort to control insect flight reliably with pupae-inserted electronics, the demonstration of using heat was realized to control insect flight initiation or take-off from a standing position. For this, a tissue embedded micro heater was used to decrease the preflight warm-up duration of hybrid electronic insect micro-air-vehicles. The EMIT procedure was followed for the surgical implantations. The biological takeoff-time at room temperature of 5–10 minutes was reduced to 58 seconds by thorax heating.

Minimizing takeoff-time will enable higher bandwidth and reliable control for repeated takeoff and landing applications. The thermal probes implanted in the pupal stage not only decrease the time required to deploy the insect-cyborgs, but they also have the potential to extend the insect cyborgs' mission time, for the biochemical energy expended for thoracic warming is conserved. Artificial heating used to overheat the thorax also may increase the payload capacity, since wing-stroke power dramatically depends on thoracic temperature. Thermal probe technology may also enable temperature control of individual muscle groups for flight control. All of this progress paves the way for future engineering approaches to understand insect flight in more detail and also to facilitate insect-based biobotic systems as centimeter scale micro-air-vehicles.

Hence, we can validate a prototypical technology using insect muscle for controlled insect locomotion, which could lead to domesticating insects to be modern "beasts of burden," to carry information processing electronics and sensors. Moreover, electronics can be used for biological and environmental sensing by tapping into the sensory systems of the insects and using their own natural receptors. Controlling motor function of invertebrates while simultaneously recording from its natural sensors enables a vast number of applications for various scientific and engineering studies. The simplicity of the optimized surgical procedure presented here allows for batch insertions to the insect for automatic and mass production of such hybrid insect-machine platforms. Therefore, this bio-electronic interface and hybrid insect-machine platform enables multi-disciplinary scientific and engineering studies not only to investigate the details of insect behavioral physiology but also to explore methodologies to control such physiology more precisely. When instrumented with equipment to gather information for environmental sensing, such insect based platforms can potentially assist humanity to monitor the ecosystems that we share with

them for a sustainable future, by creating low-cost and biodegradable sensing platforms.

APPENDIX A

MOVIE DESCRIPTIONS

Movie #1
Description: Wing actuation through electrical stimulation of flight muscles
File name: wingactuation.wmv
HTTP Location: http://www.alperbozkurt.info/thesismovies/wingactuation.wmv
Duration: 84 s
File size: 3.56 MB
Content: uni- an bilateral wing actuation, induced up- and downstroke, induced right and left yaw, induced wing flapping cessations
Movie caption: Figure 70

Movie #2
Description: Balloon assisted flight control through electrical stimulation
File name: balloonflight.wmv
HTTP Location: http://www.alperbozkurt.info/thesismovies/balloonflight.wmv
Duration: 163 s
Content: flight initiation and stopping on the bench-top setup , induced yaw at the bench-top setup, balloon assisted flight control: inititation of flight, yaw maneuver, landing
Movie caption: Figure 75

Movie #3
Description: Balloon assisted gait control through electrical stimulation
File name: balloongait.wmv
HTTP Location: http://www.alperbozkurt.info/thesismovies/balloongait.wmv
Duration: 323 sec
Content: right and lrft turn on the bench-top setup, following several 8 shaped routes on the ground
Movie caption: Figure 75

Movie #4
Description: visuomotor reflex induced yaw maneuvers
File name: LEDarena.wmv
HTTP Location: http://www.alperbozkurt.info/thesismovies/LEDarena.wmv
Duration: 29 s
Content: several yaw maneuvers to follow rotating light stripes
Movie caption: Figure 85

APPENDIX B

PUBLICATIONS

Publications produced from the content of this dissertation:

Journal Papers:

1. A. Bozkurt, R. Gilmour, A. Sinha, D. Stern D, A. Lal, "Insect Machine Interface Based Neuro Cybernetics," *IEEE Transactions on Biomedical Engineering*, 56:6, pp. 1727-33, 2009.
2. A. Bozkurt, R. Gilmour, A. Lal, "Balloon Assisted Flight of Radio Controlled Insect Biobots," *IEEE Transactions on Biomedical Engineering*, 56:9, pp. 2304-7, 2009.
3. A. Bozkurt, A. Lal, " In vivo Electrochemical Characterization of Tissue-Electrode Interface During Metamorphic Growth," in preparation to be submitted to Journal of Neural Engineering.
4. A. Bozkurt, R. Gilmour, A. Lal, "Low-Cost Flexible Printed Circuit Technology based Microelectrode Array for Extracellular Stimulation of Invertebrate Locomotory System," to be submitted to Sensors and Actuators A.

Conference Abstracts:

1. A. Bozkurt, A. Paul, S. Pulla, A. Ramkumar, B. Blossey, J. Ewer, R. Gilmour, A. Lal, "Microprobe Microsystem Platform Inserted During Early Metamorphosis to Actuate Insect Flight Muscle," *20th IEEE International Conference on Micro Electro Mechanical Systems (MEMS 2007),* Kobe, JAPAN, pp. 405-408, January 2007,.
2. A. Bozkurt, R. Gilmour, D. Stern, A. Lal, "MEMS based Bioelectronic Neuromuscular Interfaces for Insect Cyborg Flight Control,," *21st IEEE International Conference on Micro Electro Mechanical Systems (MEMS 2008),* Tucson, AZ, pp. 160-163, January 2008.
3. A. Bozkurt, A. Lal, R. Gilmour, "Electrical Endogenous Heating of Insect Muscles for Flight Control," *30th International Conference of the IEEE Engineering in Medicine and Biology Society (EMBC'08)*, Vancouver, Canada, 2008.
4. A. Bozkurt , A. Lal, R. Gilmour, "Radio Control of Insects for Biobotic Domestication," *4th International Conference of the IEEE Neural Engineering (NER'09)*, Antalya, Turkey, 2009.
5. A. Bozkurt, A. Lal , R. Gilmour, "Aerial And Terrestrial Locomotion Control of Lift Assisted Insect Biobots," *31th International Conference of the IEEE Engineering in Medicine and Biology Society (EMBC'09),* Minneapolis, MN, 2009.

APPENDIX C

MANDUCA SEXTA REARING PROTOCOL

(With the courtesy of Katherine Renwick, Marjolein Schat and Janice Beal of Boyce Thompson Institute in Ithaca, NY)

I. Eggs

1. Place a tobacco plant in the adult tent cage overnight.

2. Remove the plant from the cage the following morning. Cut off the leaves and gently roll the eggs into a small glass dish lined with a paper towel. Freeze the plant and any remaining eggs overnight before discarding.

3. Surface sterilize the eggs by placing them in a small strainer set in a dish of 5% bleach solution. Swirl the eggs for one minute, then rinse in deionized water. Spread on a paper towel under the laminar flow hood and allow to dry thoroughly.

4. Transfer the dry eggs to a clean glass dish lined with a paper towel, cover tightly, label with the date, and place in the 25°C incubator (16L:8D photoperiod, 60% relative humidity) for three days.

5. Transfer the eggs and the label to one or more hatching trays lined with paper towels. There should be no more than 150 eggs per tray. Add 6 thin slices of diet, cover, and return to the incubator. Placing a board over the cover helps reduce condensation inside the tray.

6. The eggs will begin to hatch the following day.

II. Larvae

1. One week after the eggs were collected, just after the larvae have molted to the 2nd instar, transfer them to glass tubes.

2. Prepare the glass tubes as follows:

a. Place a foam stopper in one end of each tube. Tubes are arranged vertically in racks.

b. Remove caps containing artificial diet from the refrigerator and allow to reach room temperature. Keep covered so the diet does not dry out.

c. Insert a plastic stick vertically into each cap of diet.

3. Using soft forceps, remove each larva from the hatching tray and place on a stick, near the diet. Insert the stick into the glass tube so the cap rests on top. Label the rack with the date the eggs were collected. Place in the 25°C incubator (16L:8D photoperiod, 60% relative humidity).

4. When the larvae have molted to the 5th instar and resumed feeding (approximately 10 days later), replace the caps with fresh diet. Begin emptying the frass from the tubes daily. Place boards over the tubes in the incubator to hold the caps in place so the larvae cannot escape.

III. Prepupae

1. Check the tubes daily and remove all larvae that have become prepupae. Place them in a plastic tray with paper towels so they can "wander" for a few minutes.

2. Transfer prepupae to wooden blocks. Attach a pre-made label and record today's date and the date the eggs were collected. Cover with a board kept in place with rubber bands. Place in the old incubator (no lights, 25°C, 60% RH).

IV. Pupae

1. Prepupae will molt to pupae in 5 days. They should remain in the blocks for an additional 2 days so the cuticle can become sufficiently hardened.

2. Remove each pupa from the block with a metal scoop and record its sex on the label (transfer it later to the Excel spreadsheet). Weigh the pupa using the balance with Winwedge software (so the weight is recorded directly onto the Excel spreadsheet). Replace the pupa in the block, and after all pupae are sexed and weighed, place the block back in the old incubator.

3. When all pupae from a cohort (reared from the same group of eggs) have been weighed, choose the largest 12 males and 12 females to set aside in a plastic tray for the colony. Return to the old incubator until they are ready to emerge. The remaining pupae can be distributed to researchers or used for experiments.

V. Adults

1. Several days before emergence (the developing wings begin to show dark pigmentation), place the pupae in an emergence tray in the large tent cage in room B19.

BIBLIOGRAPHY

[Akt 08] E. Aktakka, H. Kim, M. Atashbar, and K. Najafi, "Mechanical energy scavenging from a flying insect," in Proc. 13th Solid-State Sensor, Actuator, and Microsystems Workshop (Hilton Head '08), pp. 382-383, 2008.

[And 04] N. Ando, R. Kanzaki, "Changing motor patterns of the 3rd axillary muscle activities associated with longitudinal control in freely flying hawkmoths," *Zoological Science*, 21(2), pp.123-30, 2004.

[Bay 01] R.J. Bayline, C. Duch, R.B. Levine, "Nerve-muscle interactions regulate motor terminal growth and myoblast distribution during muscle development," *Dev Biol*, 231, 348-63, Mar 2001.

[Bec 99] H. Becker, A. Manz, *Microsystem Technology in Chemistry and Life Sciences*, Springer Publishing, pp 145, 1999.

[Bha 74] R.K. Bharadwaj, R.S. Chandran, L.E. Chadwick, "The cervical and thoracic musculature of Lepidoptera Part I. *Manduca sexta* (Johannson) and *Spodoptera eridania* (Cramer) (Lepidoptera: Sphingidae and Noctuidae)," *Journal of Natural History,* 8, pp. 291-300, 1974.

[Buc 97] I. Buchmann, *Batteries in a Portable World*, Ec & M Books, 1997.

[Bre 10] G.J. Brewer, "Copper toxicity in the general population," *Clin Neurophysiol.*, 121(4), pp.459-60, 2010.

[Bui 98] J.R. Buitenweg, W.L.C. Rutten, W.P.A. Willems and J.W. van Nieuwkasteele, "Measurement of sealing resistance of cell-electrode interfaces in neuronal cultures using impedance spectroscopy," *Med. Biol. Eng. Comput.,* 36, pp. 630–7, 1998.

[Bye 88] C.L. Byers, P. Zimmerman, P. Feinstein, M. Sutter, "Iridium treatment of neuro-stimulating electrodes," US Patent 4721551, 1988.

[Car 92] S.J. Carte, C.J. Linker, T. Turkle-Huslig, and L.L. Howard, "Comparison of impedance at the microelectrode–saline and microelectrode-culture medium interface," *IEEE Transactions on Biomedical Engineering*, vol 39:11, 1992.

[Cha 98] R.F. Chapman, *The Insects: Structure and Function,* Cambridge Univ. Press, pp 250, 1998.

[Cog 05] S.F. Cogan, P.R. Troyk, J. Ehrlich and T.D. Plante "In Vitro Comparison of the Charge-Injection Limits of Activated Iridium Oxide (AIROF) and Platinum-Iridium Electrodes," *IEEE Trans Biomed Eng,* 52(9), pp.1612-4, 2005.

[Cou 98] K. Coupland, "Laser cleaning of ablation debris from CO2-laser-etched vias in polyimide," *Applied Surface Sciences*, 127-129, pp.731-737, 1998.

[Cui 07] X.T. Cui, D.D. Zhou, "Poly (3,4-ethylenedioxythiophene) for Chronic Neural Stimulation," *IEEE Transactions on Neural Systems & Rehabilitation Engineering*, 15, pp.502-508, 2007.

[Cut 95] D.E. Cutler, R. R. Bennett, R. D. Stevenson, and R. H. White, "Feeding behavior in the nocturnal moth *Manduca sexta* is mediated by blue receptors but where are they in the retina?," *J. Exp. Biol.*, 198, pp.1909–1917, 1995.

[Dia 02] J. Diamond, "Evolution, consequences and future of plant and animal domestication," *Nature*, 418, 700–707, 2002.

[Duc 00] C. Duch, R. J. Bayline, R. B. Levine, "Postembryonic development of the dorsal longitudinal flight muscle and its innervation in *Manduca sexta*," *J. Comp. Neurol.,* 422 (1), pp. 1-17, 2000.

[Eat 71] J. L. Eaton, "Morphology of the head and thorax of the adult tobacco hornworm, *Manduca sexta* (Lepidoptera:Sphingidae). I. Skeleton and muscles," *Ann. ent. Soc. Am.*,vol 64, pp:437-445, 1971.

[Ell 99] C.P. Ellington, "The novel aerodynamics of insect flight: applications to micro-air vehicles," *The Journal of Experimental Biology*, 202, pp.3439-348, 1999.

[Fie 03] E.C. Field-Fote, B. Andersen, V.J. Robertson, N.I. Spielholz, "Monophasic and biphasic stimulation evoke different responses" *Muscle Nerve*, 28, pp.239-241, 2003.

[Fra 05] W. Franks, I. Schenker, P. Schmutz, A. Hierlemann, "Impedance characterization and modeling of electrodes for biomedical applications," *IEEE Trans Biomed Eng,* 52(7), pp.1295-302, 2005.

[Fry 01] M.A. Frye, "Encoding properties of the wing hinge stretch receptor in the hawkmoth *Manduca sexta,*" *Journal of Experimental Biology*, 204, 3693-3702, 2001.

[Gio 06] L. Giovangrandi, K.H. Gilchrist, R.H. Whittington, and G.T.A Kovacs, "Low-Cost Microelectrode Array with Integrated Heater for Extracellular Recording of Cardiomyocyte Cultures Using Commercial Flexible Printed Circuit Technology," *Sensors and Actuators B: Chemical*, 113, pp.545-554, 2006.

[Gri 94] W. M. Grill and J. T. Mortimer, "Electrical properties of implant encapsulation tissue," *Ann. of Biomed. Eng.* **22** 23–33, 1994.

[Gub 45] A.F. Gubin, "Bee training for pollination of cucumbers," *Bee World*, 26, pp. 34, 1945.

[Guy 96] A.C. Guyton, and J.E. Hall, *Textbook of Medical Physiology*, 9th Edition, W. B. Saunders Co., 1996.

[Hei 71] B. Heinrich, G.A. Bartholomew, "An analysis of pre-flight warm-up in the sphinx moth, *Manduca. sexta*," *J. Exp. Biol*. 55, pp. 223-239, 1971.

[Hei 74] B. Heinrich, "Thermoregulation in endothermic insects", *Science,* 185, pp. 747–756, 1974.

[Joh 04] M.D. Johnson, K.J. Otto, J.C. Williams and D.R. Kipke "Bias voltages at microelectrodes change neural interface properties in vivo," *Conf Proc IEEE Eng Med Biol Soc,* 6, pp. 4103-4106, 2004.

[Joh 05] M.D. Johnson, K.J. Otto, and D.R. Kipke, "Repeated rejuvenation improves unit recordings by consistently reducing high tissue impedances," *IEEE Transactions on Neural Systems and Rehabilitation Engineering*, 13(2), pp.160-165, 2005.

[Kam 71] A.E. Kammer, "The motor output during turning flight in a hawkmoth, *Manduca sexta*", *J. Insect Physiol.*, 17, 1073-1086, 1971.

[Kam 76] A.E. Kammer, M.B. Rheuben, "Adult motor patterns produced. by moth pupae during development," *J. Exp. Biol.,* 65, 84, 1976.

[Kam 77] A.E. Kammer, S.C. Kinnamon, "Patterned muscle activity during. eclosion in the hawkmoth,. *Manduca sexta*, "*J. comp. Physiol.*, 114, pp.313-326, 1977.

[Kam 79] A.E. Kammer, "Maturation of the Flight Motor Pattern without Movement in *Manduca sexta*," *Journal Of Comparative Physiology,* 130: 29, 1979.

[Kel 03] A. Kelber, A. Balkenius, and E.J. Warrant, "Colour vision in diurnal and nocturnal hawkmoths," *Integr. Comp. Biol.*, 43, 571-579, 2003.

[Klo 97] P. Kloppenburg, S.M. Camazine, X.J. Sun, P. Randolph, J.G. Hildebrand, "Organization of the antennal motor system in the sphinx moth *Manduca sexta*," *Cell Tissue Res*, 287, pp.425-33, 1997

[Klo 02] M.J. Klowden, *Physiological Systems in Insects*, San Diego,CA: Academic Press, 2002.

[Kon 02] P. Konig, P. F. M. J. Verschure, "Neurons in action," *Science*, 296, pp. 1817-8, 2002.

[Kor 88] G. Koren and J.J. Donelon, "CO2 laser cleaning of black deposits formed during the excimer laser etching of polyimide in air," *Appl. Phys.*, 45,1988.

[Lan 91] L. Landois, *Textbook of Human Physiology*, W. Stirling, London: Griffin, pp 371-6, 1891.

[Leb 06] M.A. Lebedev, M. A. L. Nicolelis "Brain machine interfaces: Past, present and future," *Trends Neurosci*, 29, pp. 536-546, 2006.

[Lev 95] R. B. Levine, D. B. Morton and L. L. Restifo, "Remodeling of the insect nervous system," *Curr Opin Neurobiol* 5. 28-35, 1995.

[Mar 98] S.A. Marzouk, S. Ufer, R.P. Buck, T.A. Johnson, L.A. Dunlap, W.E. Cascio, "Electrodeposited iridium oxide pH electrode for measurement of extracellular myocardial acidosis during acute ischemia," *Analytical Chemistry*; 70(23), pp. 5054-61, 1998.

[May 79] M.L. May, "Insect thermoregulation," *Annual Rev. Entomol.,* 24, 313-349, 1979.

[Mav 04] J. Mavoori, B. Millard, J. Longnion, T. Daniel, C. Diorio, "A Miniature Implantable Computer for Functional Electrical Stimulation and Recording of Neuromuscular Activity," *IEEE BioCAS 2004*, Singapore, October 2004.

[McA 95] E.T. McAdams, A. Lackermeier., J.A. McLaughlin, D. Macken, "The linear and non-linear electrical properties of the electrode-electrolyte interface", *Biosensor & Bioelectronics*, vol 10, pp 67-74, 1995.

[Men 07] R. Menzel, B. Brembs, M. Giurfa, "Cognition in Invertebrates," in *Evolution of Nervous Systems,* Vol. II: Evolution of Nervous Systems in Invertebrates, J. H. Kaas, Eds. Oxford, England: Academic Press, Chapter No. 1.26, pp. 403-422, 2007.

[Mey 01] R.D. Meyer, S.F. Cogan, T.H. Nguyen and R.D. Rauh, "Electrodeposited Iridium Oxide for Neural Stimulation and Recording Electrodes," *IEEE Trans. Neur. Systems Rehab. Eng.*, 9, pp.2-11, 2001.

[Mil 87] F.A. Miles, "Visual Stabilization of the Eyes," *Trends in Neurosciences*, 10,153,1987.

[Mil 92] J.Milde, W.Gronenberg, N.Strausfeld, "The Head-Neck System of the Blowfly Calliphora: Functional Organization and Comparisons with the Sphinx Moth *Manduca sexta*," in *The Head-Neck Sensory-Motor System*, A Berthoz, W. Graf, and PP Vidal, Eds., Oxford University Press, pp.64-70, 1992.

[Moh 01] P. Mohseni, K. Nagarajan, B. Ziaie, K. Najafi, and S. B.Crary, "An ultralight biotelemetry backpack for recording EMG signals in moths," *IEEE Trans. Biomed. Eng.,* vol. 48, no. 6, pp. 734-737, June 2001.

[Mor 94] S.L. Morton, M.L. Daroux, J.T. Mortimer, "The role of oxygen reduction in electrical stimulation of neural tissue," *J.Electrochem.Soc.*, 141, 122-130, 1994.

[Mor 06] D.F. Morey, "Burying key evidence: the social bond between dogs and people," *Journal of Archaeological Science*, 33(2), pp.158-175, 2006.

[Naj 97] K. Najafi, "Micromachined Systems for Neurophysiological Applications" in *Handbook of Microlithography, Micromachining, and Microfabrication*, Vol. 2., P. Rai-Choudhury, Ed. SPIE Press/IEE, Chapter 9, pp. 517-569, 1997.

[Nga 98] M.O. Ngadi, J.N. Ikediala, "Heat transfer properties of chicken drum muscle," *Journal of the Science of Food and Agriculture*, 78(1), pp.12–18, 1998.

[Nor 02] P. Norlin, M. Kindlundh, A. Mouroux, K. Yoshida and U.G. Hofmann, "A 32-site Neural Recording Probe Fabrication by DRIE of SOI Substrates," *Journal of Micromechanics and Microengineering*, 12, pp.414-419, 2002.

[Ott 06] K.J. Otto, M.D. Johnson, and D.R. Kipke, "Bias Voltages Change Neural Interface Properties and Improve Unit Recordings with Chronically Implanted Microelectrodes," *IEEE Transactions on Biomedical Engineering,* 53(2), pp.333-40. 2006.

[Pec 05] P. H. Peckham and J. S. Knutson, "Functional Electrical Stimulation for Neuromuscular Applications," *Annual Review of Biomedical Engineering,* 7**,** 327-360. 2005.

[Pet 98] M. Petit, V. Plichon, "Anodic electrodeposition of iridium oxide films," *J. Electroanal. Chem.,* 444, pp. 247–252, 1998.

[Pon 62] E. Ponder E, "The coefficient of thermal conductivity of blood and. various tissues," *Gen Physiol,* 45, pp. 545-551, 1962.

[Pou 66] M. Pourbaix, *Atlas of Electrochemical Equilibria*, Oxford: England, Pergamon Press, pp 399-405, 1966.

[Rei 08] T. Reissman, E. Garcia, "Surgically Implanted Energy Harvesting Devices for Renewable Power Sources in Insect Cyborgs," *ASME International Mechanical Engineering Congress and Exposition*, ASME IMECE2008-68136, 2008.

[Rhe 87] M.B. Rheuben, A.E. Kammer, "Structure and innervation. of the third axillary muscle of Manduca relative to its role in turning flight," *J. exp. Biol.*, 131, 373-402, 1987.

[Ric 93] R.R. Richardson, J.A. Miller, W.M. Reichert, "Polyimides as biomaterials—preliminary biocompatibility testing," *Biomaterials*, 14, 8, pp. 627–635, 1993.

[Ril 05] J.R. Riley, "The flight paths of honeybees recruited by the waggle dance," *Nature*, 435, pp. 205-207, 12 May 2005.

[Rou 01] P.J. Rousche, D. Pellinen, D. Pivin, J.C. Williams, R. Vetter, and D. R. Kipke, "Flexible Polyimide-based intracortical electrode arrays with bioactive capability," *IEEE Trans. on Biomedical Engineering*, vol.48(3), pp.361-371, 2001.

[Sat 09] H. Sato, C.W. Berry, Y. Peeri, E. Baghoomian, B.E. Casey, G. Lavella, J.M. VandenBrooks, J.F. Harrison and M.M. Maharbiz, "Remote radio control of insect flight," *Front. Integr. Neurosci*., 3-24, 2009.

[Sch 88] E.M. Schmidt, J.S. McIntosh, M.J. Bak, "Long-Term Implants of Parylene-C Coated Microelectrodes," *Med Biol Eng Comput*, 26, 96-101 (1988).

[Sco 06] S.H. Scott, "Converting thoughts into action," *Nature,* 442, pp.141-142, 2006.

[Sie 00] I.M. Siegel, *All about Muscle*, Demos Medical Publishing, pp 42, 2000.

[Sha 99] D. K. Shaeffer, T. Lee, *The design and implementation of low-power CMOS radio receivers*, Springer, 1999.

[Smi 84] D.S. Smith, "The structure of insect muscles," in *Insect Ultrastructure*, R.C. King and H. Akai, Eds. Plenum Press, pp 123, 1984.

[Spe 61] N. Sperelakis, T. Hoshiko, "Electrical Impedance of Cardiac Muscle," *Circ. Res.*, 9, pp.1280-1283, 1961.

[Spe 91] N. Sperelakis, C. Sfyris, "Impedance analysis applicable to cardiac muscle and smooth muscle bundles," *IEEE Trans. Biomed. Eng.*, vol. 38, pp.1010-1022, 1991.

[Sza 03] D.H. Szarowski, M.D. Andersen, S. Retterer, S.J. Spencer, M Isaacson, H.G.Craighead, J.N. Turner and W. Shain, "Brain responses to micro-machined silicon devices," *Brain Res.*, 983, 23–35, 2003.

[Tak 04] S. Takeuchi, I. Shimoyama, "A Radio-Telemetry System with a Shape Memory Alloy Microelectrode for Neural Recording of Freely Moving Insects," *IEEE Transaction on Biomedical Engineering*, vol. 51, no. 1, pp. 133-137, 2004.

[Tau 00] G. Taubes, "Biologists and Engineers Create a New Generation of Robots That Imitate Life," *Science*, pp. 80-83, April 7 2000.

[Tsa 08] W. Tsang, et.al, "Insect flight control by neural stimulation of pupae-implanted flexible multisite electrodes," *Micro Total Analysis Systems*, pp.1922-24, 2008.

[Tu 04] M.S. Tu, and T.L. Daniel, "Cardiac like behavior of an insect flight muscle," *J. Experimental Biology*, vol. 207, 2455-2464, 2004.

[Van 50] E. Van Holst, H. Milttelstaedt, "Das Reafferenzprinzip", *Naturwissenschaften*, 37, 464–476, 1950.

[Vog 01] S. Vogel, *Prime mover. A natural history of muscle,* New York, NY: W.W. Norton, 2001.

[War 01] E. Warburg, "Uber Die Polarizations capacitatdes platins," *Ann. Phys.*, vol 6, pp 125-135, 1901.

[Wei 00] J. D. Weiland and D. J. "Anderson Chronic Neural Stimulation with Thin-Film," Iridium Oxide Electrodes," *IEEE Trans, Biomed. Eng.,* 47:7, 911-918, 2000.

[Wei 02] J.D. Weiland, D.J. Anderson, M.S. Humayun, "In vitro electrical properties for iridium oxide versus titanium nitride stimulating electrodes," *IEEE Trans Biomed Eng*, 49, pp.1574-1579, 2002.

[Wen 93] G. Wendler, M. Muller, and U. Dombrowski, "The activity of pleurodorsal muscles during flight and at rest in the moth *Manduca sexta* (L.)," *J. Comp. Physiol. A*, 173, 65-75, 1993.

[Wen 02] G. Wendler, "The Organization of Insect Locomotion Systems and Computer-Based Flight Control in the Tobacco Hawkmoth *Manduca sexta*," in *Neurotechnology for Biomimetic Robots*, J. Ayers, J.L. Davis, A. Rudolph Cambridge, MA: The MIT Press, pp. 451-468, 2002.

[Wha 06] J.J. Whalen, J.D. Weiland, and P.C. Searson, "Electrochemical characterization of charge injection at electrodeposited platinum electrodes in phosphate buffered saline," *J. Electrochem. Soc.*, 153, C834-C839, 2006.

[Wil 46] C Williams, "Physiology of insect diapause: the role of the brain in the production and termination of pupal dormancy in the giant silkworm Platysamia cecropia," *Biol. Bull.*, 90, 234-43, 1946.

[Wil 61] C. Williams, "The juvenile hormone. II. Its role in the endocrine control of molting, pupation, and adult development in the Cecropia silkworm," *Biol. Bull.*, 121:572-85, 1961.

[Wil 91] M.A. Willis, E.A. Arbas, "Odor-modulated upwind flight of the sphinx moth, *Manduca sexta L.*," *J Comp Physiol A*, 169, pp.427-440, 1991.

[Wis 05] K. D. Wise, "Silicon Microsystems for use in Neuroscience and Neural Prostheses: Interfacing with the Central Nervous System at the Cellular Level," *IEEE Eng. in Medicine and Biology Magazine*, 24, pp. 22-29, September/October 2005.

[Woo 00] R. Wootton, "From insects to microvehicles," *Nature*, 403, pp.144-145, 2000.

[Xu 06] T. Xu, R.J. Farris, "Stresses associated with diffusion in Kapton and Polyacrylics films," *Journal of Applied Polymer Science*, 99-5, pp. 2661–2670, 2006.

[Yam 89] K. Yamanaka, "Anodically electrodeposited iridium oxide films (AEIROF) from alkaline solutions for electrochromic display devices," *Japanese Journal of Applied Physics Part 1*, vol. 28, no. 4, pp. 632-637, 1989.

[Zhe 84] E. Zheng, S. Shao, J.G.Webster, "Impedance of skeletal muscle 1 Hz to 1 MHz," *IEEE Trans. Bio. Eng.*, vol. 31, pp.477-481, 1984.